TECHNISCHE UNIVERSITÄT DARMSTADT

FUNKTIONALE MATERIALIEN

Unconventional Alloy Design of (Nd, Pr)-Fe-B Based Alloys for the Production of Permanent Magnets by Additive Manufacturing

Department of Materials and Earth Science

Technical University Darmstadt

Dissertation approved in fulfilment of the requirements for the degree of Doctor of Engineering

Dissertation genehmigt zur Erlangung des akademischen Grades Doktoringenieur (Dr. Ing.)

M. Sc. Lukas Schäfer

1st Referee:	Prof. Oliver Gutfleisch
2nd Referee:	Prof. Karsten Durst

Darmstadt 2023

Unconventional Alloy Design of (Nd, Pr)-Fe-B Based Alloys for the Production of Permanent Magnets by Additive Manufacturing

Genehmigte Dissertation im Fachbereich Material- und Geowissenschaften von Lukas Schäfer

1. Gutachten: Prof. Dr. Oliver Gutfleisch (Technische Universität Darmstadt)
2. Gutachten: Prof. Dr. Karsten Durst (Technische Universität Darmstadt)

Tag der Einreichung: 28.02.2023

Tag der Prüfung: 07.06.2023

Darmstadt

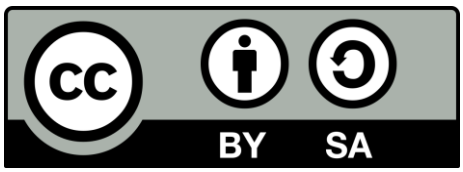

Erklärung zur Dissertation anhand der Promotionsordnung des Fachbereiches

§8 Abs. 1c

Ich versichere hiermit, dass die elektronische Version meiner Dissertation mit der schriftlichen Version übereinstimmt.

§8 Abs. 1d

Ich versichere hiermit, dass zu einem vorherigen Zeitpunkt noch keine Promotion versucht wurde.

§9 Abs. 1

Ich versichere hiermit, dass ich die vorliegende Dissertation selbstständig verfasst habe. Alle wörtlich und inhaltlich übernommenen Stellen und sind als solche gekennzeichnet.

§9 Abs. 2

Die Arbeit hat bisher noch nicht zu Prüfungszwecken gedient.

Darmstadt den 06.07.2023 Lukas Schäfer

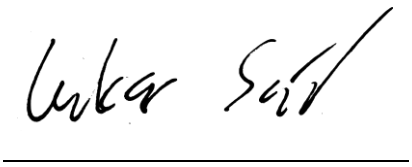

Abstract

The scientific goal of this work is to investigate hard magnetic alloys based on Nd-Fe-B for the production of permanent magnets by additive manufacturing. The experimental work covers the material chain from the element to the (printed) component, including the synthesis of the alloys from elements, the thermal treatments necessary to improve microstructure and magnetic properties and finally the powder production and laser fusion to obtain bulk samples. By this, an interdisciplinary approach with modern characterization techniques of materials science and novel manufacturing techniques is chosen, focusing on the qualification of hard magnetic rare earth alloys for the production of permanent magnets by laser powder bed fusion (PBF-LB).

The chosen compounds are related to the commercial high-performance Nd-Fe-B magnets. However, due to the very local and complex melting and solidification processes during PBF-LB, the materials need to be adapted. In this context, two approaches were investigated which have in common the formation of unusual phases and microstructures in the Nd-Fe-B system. First, the influence on phase formation and magnetic properties of element dopants such as cobalt, copper and transition metals (titanium, vanadium, zirconium, molybdenum, niobium, tungsten, tantalum) were investigated by the synthesis of alloys with systematic addition of the dopants. The solidification behavior was investigated by rapid solidification experiments which provides metastable phases/ microstructure and is starting point for the magnetic hardening by thermal treatments. A coercivity of almost $\mu_0 H_C = 1$ T could be achieved in $Nd_{16}Fe_{53}Co_{20}Cu_2Mo_2B_7$ samples. A second approach was based on high copper addition in (Pr,Nd)-Fe-Cu-B compounds which is the basis for high coercivity. Uncommon intermetallic phases are forming whose influence on coercivity was investigated. For this purpose, the phase stability and magnetic properties were explored within a quasi-ternary phase diagram. With suitable alloy adjustment and heat treatment, coercivities above $\mu_0 H_C = 2$ T could be achieved in Pr-Fe-Cu-B alloys.

Based on these lab-scale experiments, alloy compositions with promising magnetic properties were selected and powder for the additive manufacturing tests was produced. In this context, a systematic approach and parameter study of the PBF-LB experiments was established in cooperation with the Institute for Production Management, Technology and Machine Tools (PTW), adapted to small material quantities and the properties of the materials used here, which differ significantly from structural materials. In addition to the adaptations of the materials and alloy modifications, recurring errors and problems during additive manufacturing process could be identified.

In addition to the exceptional microstructures and magnetic properties in the modified rare earth-based alloys, the findings from the PBF-LB experiments serve as a starting point for future investigations with advanced process monitoring methods.

Kurzfassung

Das wissenschaftliche Ziel dieser Arbeit ist die Untersuchung von hartmagnetischen Legierungen auf der Basis von Nd-Fe-B für die Herstellung von Permanentmagneten durch additive Fertigung. Die experimentelle Arbeit deckt die Materialkette vom Element bis zum (gedruckten) Bauteil ab, einschließlich der Synthese der Legierungen aus Elementen, der erforderlichen thermischen Behandlungen zur Verbesserung der Mikrostruktur und der magnetischen Eigenschaften und schließlich der Pulverherstellung und des Laserschmelzens. Dabei wird ein interdisziplinärer Ansatz mit modernen Charakterisierungstechniken der Materialwissenschaft und neuartigen Fertigungstechniken gewählt, der sich auf die Qualifizierung von hartmagnetischen Seltenerdlegierungen für die Herstellung von Dauermagneten durch Pulverbettbasiertem Laserstrahlschmelzen (PBF-LB) konzentriert.

Die ausgewählten Verbindungen sind mit den kommerziellen Hochleistungsmagneten aus Nd-Fe-B verwandt. Aufgrund der sehr lokalen und komplexen Schmelz- und Erstarrungsprozesse beim PBF-LB müssen die Werkstoffe jedoch angepasst werden. Es wurden zwei Ansätze untersucht, denen die Bildung ungewöhnlicher Phasen und Gefüge im Nd-Fe-B-System gemein ist. Zunächst wurde der Einfluss von Elementdotierstoffen wie Kobalt, Kupfer und Übergangsmetallen (Titan, Vanadium, Zirkonium, Molybdän, Niob, Wolfram, Tantal) auf die Phasenbildung und die magnetischen Eigenschaften durch die Synthese von Legierungen mit systematischer Zugabe der Zusatzelemente untersucht. Das Erstarrungsverhalten wurde mit Hilfe von Rascherstarrungsexperimenten untersucht, die metastabile Phasen bzw. ein metastabiles Gefüge liefern und Ausgangspunkt für die magnetische Härtung durch thermische Behandlungen sind. In $Nd_{16}Fe_{53}Co_{20}Cu_2Mo_2B_7$ Proben konnte eine Koerzitivfeldstärke von fast $\mu_0 H_C = 1$ T erreicht werden. Ein zweiter Ansatz basiert auf einem hohen Kupferzusatz in (Pr,Nd)-Fe-Cu-B Verbindungen, der die Grundlage für eine hohe Koerzitivfeldstärke bildet. Es bilden sich ungewöhnliche intermetallische Phasen, deren Einfluss auf die Koerzitivfeldstärke untersucht wurde. Zu diesem Zweck wurden die Phasenstabilität und die magnetischen Eigenschaften in einem quasi-ternären Phasendiagramm erforscht. Bei geeigneter Legierungseinstellung und Wärmebehandlung konnten in Pr-Fe-Cu-B Legierungen Koerzitivfeldstärken über $\mu_0 H_C = 2$ T erreicht werden.

Auf der Grundlage dieser Experimente im Labormaßstab wurden Legierungszusammensetzungen mit vielversprechenden magnetischen Eigenschaften ausgewählt und Pulver für die additiven Fertigungstests hergestellt. In diesem Zusammenhang wurde in Zusammenarbeit mit dem Institut für Produktionsmanagement, Technologie und Werkzeugmaschinen (PTW) eine systematische Vorgehensweise und Parameterstudie der PBF-LB Experimente etabliert, angepasst an die kleinen Materialmengen und die Eigenschaften der hier verwendeten Werkstoffe, die sich deutlich von Strukturwerkstoffen unterscheiden. Neben den Anpassungen der Werkstoffe und Legierungsmodifikationen konnten wiederkehrende Fehler und Probleme im additiven Fertigungsprozess identifiziert werden.

Neben den außergewöhnlichen Mikrostrukturen und magnetischen Eigenschaften in den modifizierten Legierungen auf Seltene-Erden-Basis dienen die Erkenntnisse aus den PBF-LB Experimenten als Ausgangspunkt für zukünftige Untersuchungen mit Prozessüberwachungsmethoden.

List of Content

1. Motivation

The increasing demand and awareness for functional magnetic materials combined with the social and political desire for renewable energy, e-mobility and resource efficiency is more relevant than ever, demanding and promoting research and innovation in this field. Functional magnetic materials, especially hard and soft magnets, are everywhere in today´s life and key components in many high-tech technologies. Highest magnetic performance of permanent magnets is found in Rare-Earth-based alloys, specifically in Nd-Fe-B. Magnets from this material show extraordinary magnetic properties which are the reason for their industrial importance.

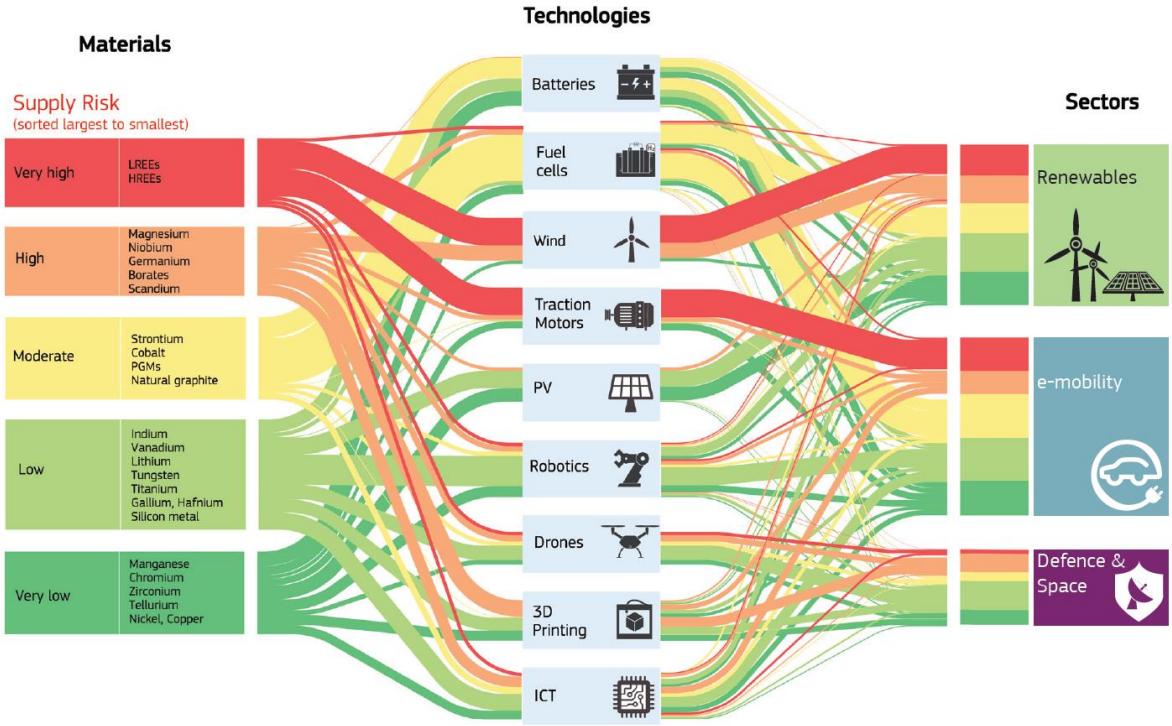

Figure 1: The supply risk of Heavy and Light Rare Earth Elements (HREE and LREE) is a well-known problem and displayed in the flow chart by the EU commission [1]. Such elements are the fundament for key technologies in the sectors of renewable energy and e-mobility. The political efforts to counteract climate change also mean optimizing the circular economy and the resource-efficient use of such materials. In the words of Prof. Oliver Gutfleisch: "The energy transition requires a material transition!"

At the same time, the criticality of Rare Earth elements is an undeniable problem, which is not based on the "rarity" of the elements as implied by the name. The supply risk of such elements is high (Figure 1) and based on the local abundance in China which makes it the worldwide monopoly for Rare Earth production as shown in Figure 2. This situation became prominent in 2011 as the “Rare Earth Crisis”, when the value for Rare Earths multiplied within months due to the price dictation of China. After this incident at the latest, the European Union was well aware of its full import dependence for Rare Earths and took acts to ensure the economic stability [2]. The “European Green Deal” led to funding frameworks such as Horizon Europe and the foundation of the European Raw Materials Alliance (ERMA) [3] which is led by the European Institute of Innovation and Technology – Raw Materials (EIT RawMaterials) [4]. However, not only Europe is aware of this geo-political dilemma. The USA committed to reduce 52 % reduction of its greenhouse gas pollution from 2005 until the year 2050. This includes the usage of renewable energies and alternative energy generation, which implies the increasing demand for Nd-Fe-B magnets. Similar to the EU efforts, in February 2021, the “Executive Order on America´s Supply Chains” was declared as the base for building a more secure and diverse

U.S. supply chain [5]. In this context, the worldwide research on permanent magnets has ensured its importance and became even more prominent by the increase in e-mobility and renewable energies [6]. Especially the resource efficient use and production of critical materials is necessary and the fundament for a successful energy transition. This aspiration translates into several approaches on the research of permanent magnets [7]–[9].

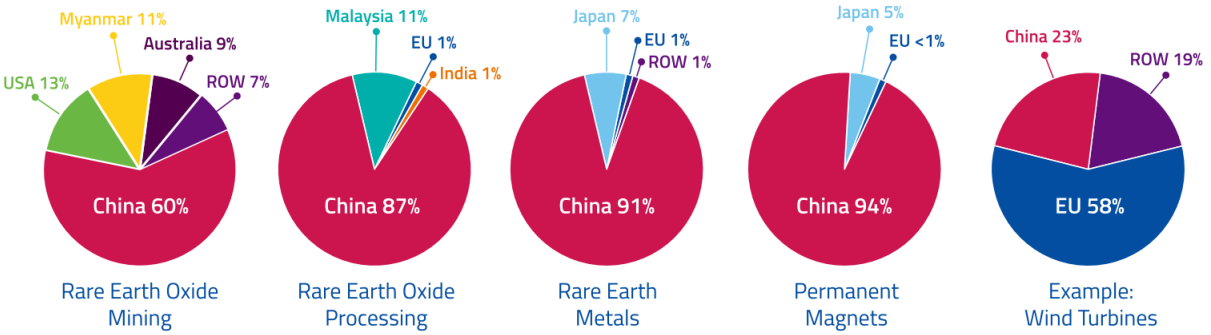

Figure 2: Estimated market shares in 2019 from Rare Earth oxide mining until the use in wind turbines as permanent magnets. The reason for Chinas dominance until application is not only based on the abundance but on the cost. Western magnet companies can hardly compete with the price of magnets from China. [6]

The first obvious goal is to completely avoid the use of critical Rare Earth elements. Although there are approaches for Rare Earth free permanent magnets such as ferrites [10], AlNiCo [11] and improvements in Mn-based materials [12], the high magnetic performance relies on the unique intrinsic properties of Rare Earth intermetallics which appear to be irreplaceable. Consequently, much effort has been made to reduce the Rare Earth content in magnets. The substitution by less critical rare earth elements such as Lanthanum and Cerium was successfully implemented in sintered [13] and hot-deformed [14] (Nd, La, Ce)-Fe-B magnets. Furthermore, other Rare Earth-lean compounds are under intense investigation due to their promising intrinsic magnetic properties. Another approach, which is the basis for this thesis, arises from the novel development of a fast-evolving production technique, Additive Manufacturing. Conventional permanent magnets have simple geometries which is based on the limitations during production. Common production routes, such as sintering or hot deformation, do not easily allow for complex shapes. Due to these restrictions, the design of components and the application of magnets does strongly depend on the production. The premise of additive manufacturing of functional, especially magnetic, materials involves the free design of novel components and geometries while at the same time using the materials in a way that conserves resources. The advantages of high geometrical freedom, local variation of the production parameters and chemical gradients by the layer-by-layer building principle are tempting improvements. Complex designs together with effective and localized functionalities can be realized which goes beyond conventional magnetic components. In this light, the promise of the Additive Manufacturing process applied to magnetic functional materials becomes increasingly attractive and could open many new application aspects [15], arising from the possibility to create complex components with tailored magnetic flux density distribution, that have been impossible to build previously [16]–[18]. The big problem which arises is the uncontrolled and local melting and solidification, which contrasts with the temperature- and time -controlled processing during commercial sintering or hot compaction. The alloy design for conventional Nd-Fe-B magnets cannot be easily translated to the Additive Manufacturing process and needs careful alloy design and microstructural engineering.

Scientific Approach and Goal of this work

The successful Additive Manufacturing of permanent magnets is not a trivial task. The conventional Nd-Fe-B alloys are optimized for their specific production route and rely on controlled processing parameters which cannot be secured during the laser fusion. The goal of this work is to modify Nd-Fe-B based alloys specifically for the use in Laser Powder Bed Fusion (PBF-LB). By making use of secondary phases in the Nd-Fe-B system, unconventional and novel magnetic hardening processes are explored.

An interesting alloy system is the quaternary (Nd,Pr)-Fe-Cu-B. It is known that high coercivity can be achieved in bulk state by specific annealing treatments in [19]–[27]. The addition of Cu to the ternary system strongly improves the hard magnetic properties (coercivity) due to formation of additional grain boundary phases (e.g. RE-Cu low melting eutectics [28] or $(Nd,Pr)_6Fe(Cu, Al, Ga)_{14}$ in commercial magnets [29]), which separate the hard magnetic grains. Thus, on a variety of compositions, the Pr-Fe-Cu-B material system features large coercivity in bulk state independent of the consolidation technique, which makes it a potential material system to produce permanent magnets by PBF-LB.

Furthermore, a novel route for magnetic hardening of Nd-Fe-B based alloys is shown in this work. The principle is based on the formation of a metastable $Nd_2Fe_{17}B_x$ phase during rapid solidification processes [30]–[47], which can be further transformed to the hard magnetic $Nd_2Fe_{14}B$ phase along with nanometer sized precipitates by a temperature induced solid state reaction. By combining specific modification of the alloy with elements such as Cobalt, Molybdenum and Copper, the formation of the metastable phase and the temperature profile to promote the microstructural transformation are explored. Finally, the magnetic hardening of bulk pieces is realized and translated to the Additive Manufacturing of the developed alloy.

The scientific approach towards additive manufactured permanent magnets includes the alloy development of Nd-Fe-B related alloys. Based on systematic studies of compositional modifications and the impact on the magnetic properties on lab-scale, the alloys are upscaled and prepared for the Laser Powder Bed Fusion technique. Accompanied by material science characterization methods such as microscopy, X-ray diffraction and magnetic measurements, this work aims for the qualification of Nd-Fe-B and its technical realization as additive manufactured permanent magnets.

2. Fundamentals

2.1. Magnetism and Magnetic Materials

The research on functional magnetic materials unites atomistic, quantum mechanical effects and technical advancements of production. For a detailed insight into the origin of magnetism and the quantum mechanical basis, it is referred to the book of Miyazaki [48]. Different magnetic models and approaches of theoretical description of magnetic behaviour in materials is given by the book of Skomski [49]. For a basis and broad overview on magnetism towards application it is referred to the books of Coey [50], [51] and Cullity [52]. Magnetic domain imaging techniques and fundamental physics behind are explained in the book of Schäfer and Hubert [53]. The interesting chemistry and magnetic properties of Rare Earth intermetallics has a long history and contains much experimental and theoretical work. A great summary and explanation is given by the the *Handbook on the Physics and Chemistry of Rare Earths*, edited by Geschneidner, Bünzli and Pecharsky. Especially the volumes 1 [54], 2 [55] and 11 [56] introduce the chemistry of Rare Earths and interesting physical properties. The magnetism of Rare Earths towards application is part of the comprehensive *Handbook of Magnetism and Magnetic Materials*, edited by Wolfarth and Buschow. Besides the magnetic properties of many compounds, especially volumes 1 [57], 3 [58], 4 [59] and 6 [60] contain important knowledge about Rare Earth intermetallics and development towards magnets.

The Origin of the Magnetic Moment and Magnetic Ordering

In the history of humanity, magnetism was and still is a haunting and mesmerizing physical effect which is difficult to explain. It is impossible to experience and distinguish the magnetic properties of materials with our human senses. No wonder, since the reason and origin is coming from the world of Quantum Mechanics in which “vividness” can be called a foreign word.

The very source of the macroscopic magnetism in solids is the angular momentum of elementary particles. The nucleus consisting of protons and neutrons has only a small contribution to the magnetic moment of an atom. On the other hand, the electrons contribute with their orbital motion and with their spin. Due to the quantized nature of the resulting angular moment, the smallest increments of magnetic moment can be given in units of the Bohr magneton magnetons μ_B:

$$\mu_B = \frac{e\hbar}{2m_e}$$

Equation 1: Bohr Magneton

with m_e as the electron mass, e the electrons charge and $\hbar$ the Planck constant.

Although the origin of a magnetic moment seems clear, only the interaction between atoms via their electrons can explain why there is a macroscopic magnetic ordering and a distinction between soft and hard magnetic materials. The Coulomb repulsion of charged electrons and the Pauli exclusion of identical fermions leads to an exchange energy E_{ex} for each bonding/ parallel

and antibonding state of electrons. This energy includes the spin momenta $\overrightarrow{S_i}$ and $\overrightarrow{S_j}$ of the electrons via the exchange integral J_{ex}:

$$E_{ex} = -J_{ex}\overrightarrow{S_i}\overrightarrow{S_j}$$

Equation 2: Exchange Energy

The sign of J_{ex} – meaning a positive or negative exchange interaction- decides if the magnetic moments are aligned parallel or antiparallel – ferromagnetic or antiferromagnetic ordering. It is very important to emphasize, that the exchange and ordering of magnetic moments does not originate from magnetic interaction but from the fermionic and electric nature of the electrons which carry the magnetic moment.

In solids, the sign and strength of simplified exchange does depend on the interatomic distance between the atoms. This is depicted in the phenomenological Bethe-Slater-Neél curve. It is able to explain why only iron, cobalt and nickel are ferromagnetic whereas manganese shows an antiferromagnetic behavior.

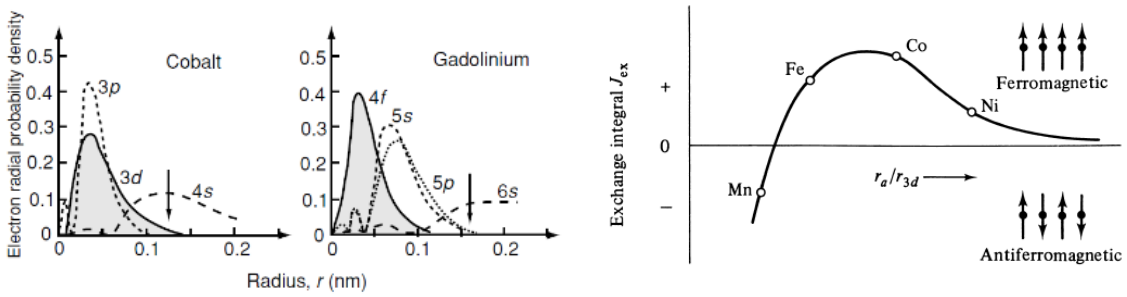

Figure 3: The left figure shows the radial electron probability of a Cobalt and Gadolinium atom. The small arrow indicates the interatomic distance. Whereas the 3d electron of the Cobalt atom are interacting, the 4f electrons of the Gadolinium atom are closer to the atom center [50]. On the right side the Bethe-Slater curve which simplifies the exchange energy/ integral depending on the interatomic distance. The positive exchange for Fe, Co and Ni leads to ferromagnetic order [52].

Furthermore, the exchange interaction, more specifically its strength, correlates with the temperature stability of the magnetic order. This means that a high exchange energy in a Fe-Co alloy translates directly in a high critical temperature above which the ferromagnetic ordering becomes unstable and disappears, the Curie Temperature T_C. Of course, this phenomenological view is not enough to explain the magnetic behavior of materials entirely which becomes apparent when comparing atomic and electronic structure of the 3d Transition Metal (TM) elements with the 4f Rare Earth (RE) series.

The nature of materials is based on the assembly of multiple atoms to form a solid. The interaction of valence electrons leads to a splitting of energy levels which can be describe as a continuous energy distribution of electron states. The metallic character and conductivity is based on the unfilled valence band. For the 3d TM metals, the very same valence electrons which are responsible for conductivity do also possess the magnetic moment of the atom which is the reason for the fractional number of Bohr Magnetons per atom. The magnetic moment in Fe, Co and Ni is based on a band splitting and the interaction of the conductive electrons

forming magnetic moment and order. From these considerations, research is able to correlate the measured magnetic moment of 3d TM alloys with the theory.

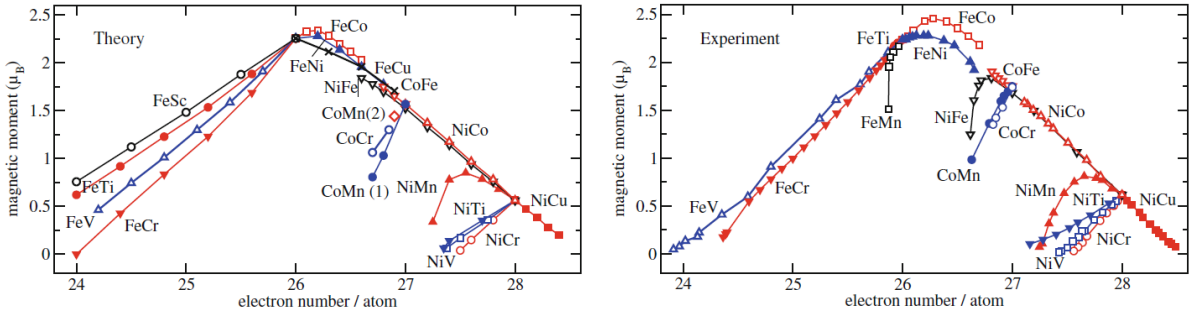

Figure 4:Theoretical (left) and experimental (right) Slater-Pauling curve of different 3d transition metal alloys. The curves show the average magnetic moment over the electron number per atom. [51]

This behavior is called band- or itinerant magnetism which was first described by the Stoner Model. The fundamental idea is that the exchange interaction between the valence electrons leads to a "rigid band shift" between the spin-up and spin-down part of the Density of States (DOS), on the cost of kinetic energy. This shift gives rise to a discrepancy between both spin sorts and a resulting net magnetic moment per atom. Stoner formulated a criterion which needs to be fulfilled in order to stabilize a spontaneous ferromagnetic ordering based on the energy balance between the gain in magnetic energy coming from the exchange energy and the cost of kinetic energy which is summarized in the Stoner exchange integral I.

$$I * n_{E_F} \geq 1$$

Equation 3: Stoner Criterion

Based on this description, the importance of the density of states at the Fermi level n_{E_F} becomes apparent. Whereas the Stoner exchange integral varies smoothly with the transition metal row, the density of states shows drastic changes and is high for Fe, Co and Ni leading to their elemental ferromagnetic behavior.

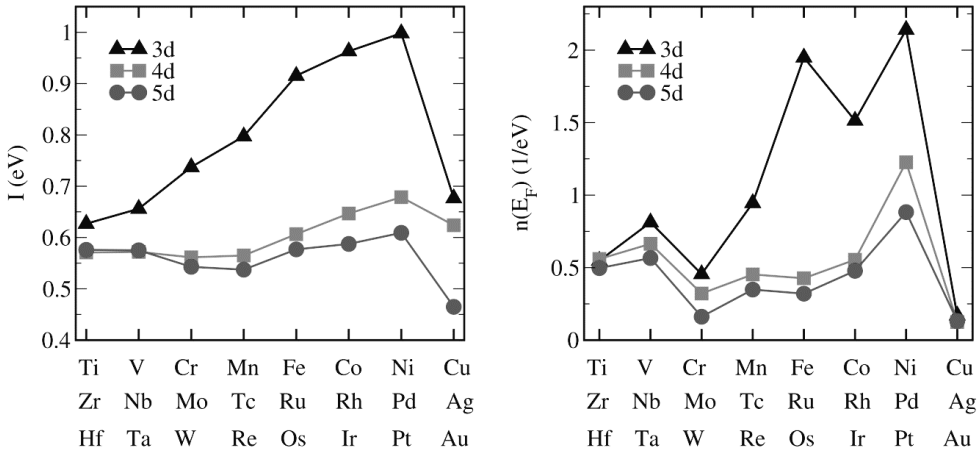

Figure 5: The Stoner exchange integral I (left) and the density of states at the Fermi level (right) for different transition metals. The graphs show that not only the exchange integral but the large difference in the density of states determines the ferromagnetic behavior. [51]

Contrary to the transition metal series, the chemistry of the 4f RE series is much different. The unfilled 4f orbitals are buried deep in the atom center, which explains the very similar chemical properties of the elements in this series. Although these metals do show conductivity and metallic character, their valance electrons are not the ones which carry the magnetic moment. Rather the electrons in the unfilled 4f orbitals give rise to integer number of Bohr Magneton per Atom. The occupancy of these 4f energy states follows the Hund Rules, meaning the minimization of the ground state by considering the Pauli exclusion for fermions, electric repulsion and spin-orbit energy levels. The calculated magnetic moments for the ground state ions do agree with the experimental results. Furthermore, the strong spin-orbit coupling of the 4f electrons leads to very interesting and important effect for permanent magnets, the magnetocrystalline anisotropy [61]. The origin for this is the occupancy of the 4f orbital following Hund´s Rules which does affect the shape of the ions. The magnetic moment depends on the orbital motion of the electrons and therefore the shape of the orbital. This is represented by the RE element specific Stevens Coefficients α_j which are based on the quantum mechanical treatment of the 4f ions and orbitals. The shape of the orbital interacts with its charged environment, the crystal field given by the neighboring atoms, in order to minimize the electrostatic energy. This effect leads to an orientation dependent alignment of the magnetic moment in a crystal.

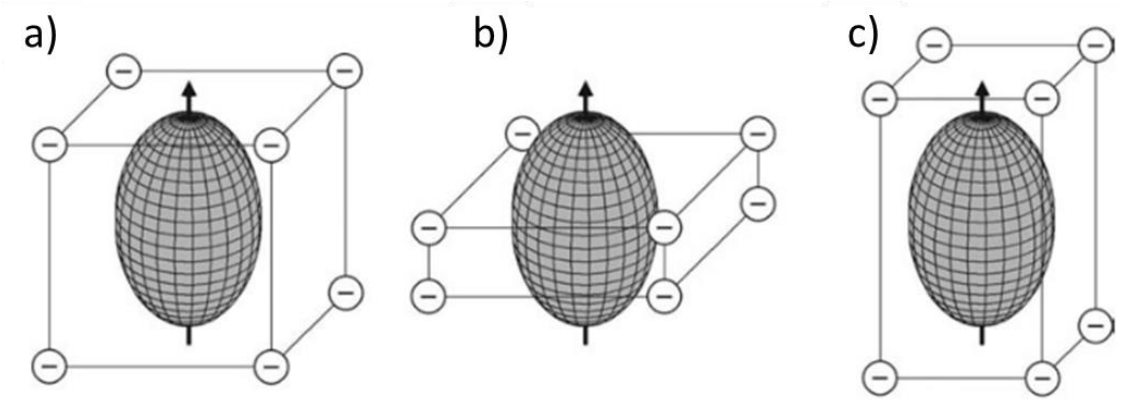

Figure 6: Crystal field interaction between a 4f electron distribution (prolate ion) and a) cubic and b-c) tetragonal environments. The difference between b) and c) are opposing crystal field parameters which lead to c) an easy axis alignment of the magnetization whereas the vector in c) lies in the a-b plane of the tetragonal environment. Adapted from [49].

The minimum and maximum energy lead to an orientation of the magnetization along specific crystallographic directions, which can be measured experimentally. Considering the simplest case of a magnetic volume V with uniaxial magnetocrystalline anisotropy, the energy E_A can be formulated as:

$$E_A = V(K_1 \sin^2\theta + K_2 \sin^4\theta + K_3 \sin^6\theta)$$

Equation 4: Anisotropy Energy

The K_i are anisotropy constants, whereby the leading factor is K_1 and the others can be often neglected. In the simplified case, the polar angle θ is referring to the c-axis. Considering a positive sign of K_1 it becomes apparent, that the energy minimum with $\theta = 0° \; and \; \theta = 180°$

lies along the c-axis called “easy axis”. On the other hand, a negative K_1 leads to a “easy plane” magnetocrystalline anisotropy. The role of the 4f ion anisotropy and crystal field surrounding on the magnetocrystalline anisotropy becomes apparent when looking at the definition of the anisotropy constant K_1. It couples the shape of the ion given by the Stevens Coefficient α_j with the magnetic moment J and the crystal-field parameter A_2^0:

$$K_1 = -\frac{3}{2}\alpha_j * r_{4f}^2 * A_2^0 * (2J^2 - J)$$

Equation 5: Anisotropy Constant

The term magnetocrystalline anisotropy means that the energy of a magnetic body depends on the correlation between the crystallographic direction and the external applied field. The strong influence of the 4f RE magnetism, the anisotropy of ions and the resulting magnetocrystalline anisotropy is the fundament for permanent magnets. These intrinsic properties are the prerequisite for magnetic hardness and high coercivity. However, only the union of 3d TM metals and 4f RE elements leads to special and important magnetic properties and finally to great importance in technical applications. [61][62]

Table 1: First and second anisotropy constants at room temperature for selected materials. The strong uniaxial magnetocrystalline anisotropy apparent by a high, positive K_1 of $Nd_2Fe_{14}B$ is the intrinsic fundament for the use as a permanent magnet. [51]

	K_1 (MJ/m^3)	**K_2 (MJ/m^3)**	**Structure**
Fe	0.048	0.015	Cubic
Ni	-0.005	0.005	Cubic
Co	0.53	0	Hexagonal
Fe_3O_4	-0.011	0.028	Cubic
$Nd_2Fe_{14}B$	4.9	0.65	Tetragonal

2.2. Magnetism of Lanthanide-Transition Metal Intermetallics

Rare Earth (RE) -Transition Metal (TM) intermetallics show interesting magnetic properties and combine the properties of both element classes. The Lanthanides are divided into Light-REs starting from the element with number Z=57 Lanthanum to Z=63 Europium and Heavy-REs from Z=64 Gadolinium to Z=71 Lutetium. The fourth period TM elements have delocalized 3d electrons, which are sometimes described by a free-electron gas. There are several intermetallic compounds between RE an TM and several show unique magnetic properties while combining the high magnetic anisotropy of REs with high Curie temperature of the ferromagnetic TMs. The 4f electrons are well localized and possess large spin-orbit coupling, which brings large magnetocrystalline anisotropy, but at the same time the Curie temperature is low, since the interaction between the RE atoms is indirect and weak. The strong TM-TM interaction gives rise to the relatively high Curie temperature and brings high magnetic moment. [62]

The intrinsic magnetic properties are based on exchange interaction and magnetocrystalline anisotropy. Dividing the compounds into sublattices of TM and RE atoms makes it easier to describe the underlying effects. The magnetic interactions can be divided into to three categories. RE-RE interaction is the weakest of them, since the 4f electrons are localized. TM-TM interactions of the TM sublattice lead to strong exchange coupling between the TM atoms mediated by the 3d electrons and are the main contribution to the high Curie temperature. The RE-TM interactions are small but couple the mutual orientation of the RE and TM sublattices. In general, the magnetocrystalline anisotropy of RE is high at low temperatures. The contribution of TM anisotropy is important at elevated temperature. Therefore, a strong magnetocrystalline anisotropy of the intermetallics is based on strong RE-TM interaction. However, the coupling between the RE and TM lattice is not straight forward. It is indirect between the intra-atomic exchange of 4f-5d electrons in the RE atom and interatomic exchange of the 5d-RE and 3d-TM electrons. Generally, it is found that 4f-RE and 3d-TM moments are coupled antiferromagnetically. The differences of heavy and light RE spin orbit coupling of 4f electrons explains why there can be parallel or antiparallel alignment between the RE and TM sublattice. This effect has technical relevance in Nd-Fe-B based magnets. Whereas the Nd and Fe atoms show parallel coupling, heavy RE like Dy or Tb are coupled antiparallel to the Fe moments. As a result, the total magnetization of the magnet is lower by the substitution of Nd by heavy RE elements in magnets. The fact that Dy or Tb are still used is due to the high magnetocrystalline anisotropy of the respective $(Dy,Tb)_2Fe_{14}B$ phase and the resulting increase in the coercivity and temperature stability of the magnets. This technical application is a great example of the controlled intrinsic modification of magnetic properties which translate into the measurable extrinsic properties of the magnet. [62], [63]

The most important intermetallics for permanent magnets are formed by light RE and Fe or Co. Most of the RE_xTM_y (TM=Fe, Co, Ni) compounds are isostructural and only the magnetic ordering is changing. Important phases are based on the $CaCu_5$ structure. In the 1960s, research on permanent magnets focused on compounds like YCo_5 which showed high coercivity due to magnetocrystalline anisotropy. Replacing Y by Sm improved the magnetic properties due to the contribution of Sm to the anisotropy. The disadvantage of low magnetization was tried to overcome by using Sm_2Co_{17} which resulted in the development of todays high temperature Sm-Co based magnets which unite both high anisotropy of $SmCo_5$ and high magnetization of Sm_2Co_{17} by a controlled precipitation hardening mechanism [64]–[66]. Soon, the desire to use materials based on Fe instead of Co led to the development of Nd-Fe-B magnets which started by the discovery of the ternary intermetallic $Nd_2Fe_{14}B$ phase [67]–[71]. The advantage was the

use of Fe instead of Co and using the ferromagnetic coupling between the Nd (or Pr) and Fe sublattice. The intrinsic magnetic properties were soon translated to high performance permanent magnets by controlled production techniques. [72]

Table 2: Collection of some important Rare Earth intermetallics. In general, the intrinsic magnetic properties are based on the interaction between Rare Earth and Transition Metal in the crystal. Although the chemical composition and crystal structure are the same, the interplay between 4f electronic structure and crystal field are the reason for very different properties. Data taken from [50], [51].

	K_1 (MJ/m^3)	$\mu_0 M_S$ (T)	T_C (K)	Structure
$NdCo_5$	0.7	1.23	910	Hexagonal
$SmCo_5$	17.2	1.07	1003	Hexagonal
Nd_2Co_{17}	-1.1	1.39	1150	Rhombohedral
Sm_2Co_{17}	3.3	1.2	1190	Rhombohedral
$Nd_2Fe_{14}B$	4.9	1.6	585	Tetragonal
$Sm_2Fe_{14}B$	-12	1.49	618	Tetragonal

2.3. Intrinsic and Extrinsic Magnetic Properties

Discussing the reason for magnetism, order and interaction of atoms in a crystal field leading to magnetocrystalline anisotropy is still not enough to explain the behaviour of a ferromagnetic sample in an external magnetic field. The reason for this is the neglection of the magnetostatic energy. If we consider our sample to be ferromagnetic, the result would be a parallel alignment of all magnetic moments along its easy axis. This would lead to a large magnetic stray field around the sample volume which possess an important energy contribution E_d. In order to minimize its total energy E_{tot}, the sample is forming magnetic domains which guide the magnetic field lines through the sample volume. The energy contributions can be formulated as:

$$E_{tot} = E_{ex} + E_d + E_A + E_{stress} + E_{ms} + E_{ext}$$

Equation 6: Energy Balance Regarding Magnetic Domain Formation

This complex energy balance is important to understand formation and structure of magnetic domains. Besides the stray field, it depends on the magneto-elastic energy E_{stress} which can occur by internal stresses, the magnetostrictive energy E_{ms} due to spontaneous deformation along the magnetization direction and on the energy related to external applied field E_{ext}.

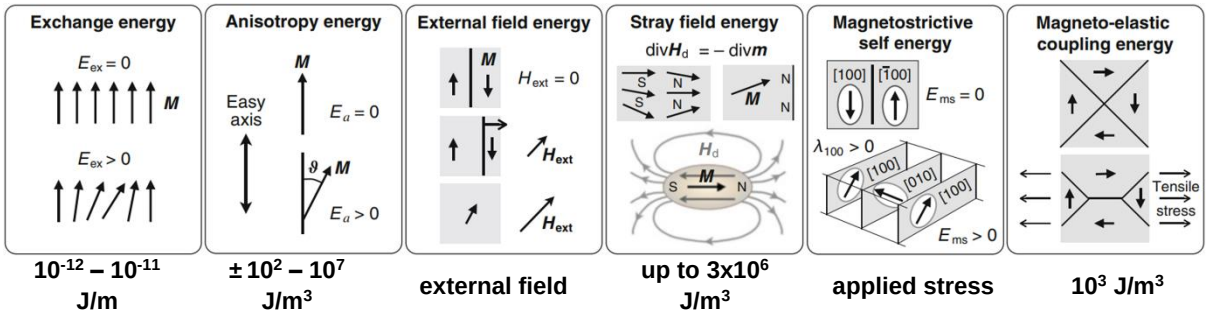

Figure 7: The energy minimization is the reason for magnetic domains. The different energy contributions are listed together with the energy ranges. [51]

As already described, the exchange interaction favours the parallel alignment of magnetic moments in order to minimize the energy E_{ex}. In between domains, it favours only small misalignment of the magnetic moment, which is the reason for a gradual transition between the magnetization direction by forming domain walls. In general, two types of domain walls can be distinguished, the Neél and Bloch domain wall. For thin films, Néel walls can be observed which are characterized by rotation of the magnetic vector perpendicular to the wall plane. However, bulk samples show Bloch walls where the magnetization rotates parallel to the wall plane in order to minimize the stray field.

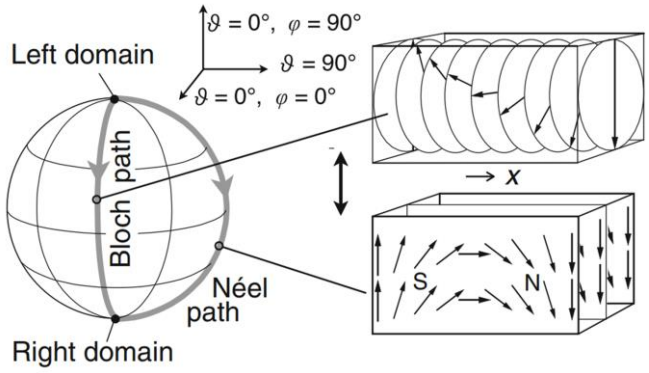

Figure 8: Schematic drawing of Block and Néel magnetic domain walls. The magnetization vector rotates perpendicular for Néel walls which are found in thin film samples, whereas the Bloch walls show the parallel rotation to the wall plane in order to minimize the stray field.[51]

Regarding exchange alone, the rotation would happen only in small increments and the domain wall would be huge. The anisotropy energy is acting opposingly by forcing the magnetic moment along the crystal's easy axis. This interplay of the energy terms is represented in the domain wall thickness δ_W, with A as the exchange stiffness and K_1 the already mentioned leading anisotropy constant:

$$\delta_W = \pi \sqrt{\frac{A}{K_1}}$$

Equation 7: Domain Wall Width

The first observation is, that uniform magnetization breaks up into domains due to the high stray field energy E_d. The domain structure depends strongly on the material's intrinsic magnetic properties. Especially the stray field is directly linked to the saturation magnetization of the samples M_s and can be formulated as:

$$E_d = \frac{1}{2}\mu_0 M_s^2 = K_d$$

Equation 8: Stray Field Energy

It is important to realize, that the driving force for domain formation is based on its own magnetization which is represented by the effective stray field coefficient K_d. The domain pattern depends strongly on the interplay between stray field and anisotropy which can be represented in the form of a Quality Factor Q, where K_{eff} represents the leading anisotropy constant:

$$Q = \frac{K_{eff}}{K_d}$$

Equation 9: Quality Factor

If $Q > 1$, the anisotropy dominates over the stray field energy and large domains with magnetization along the easy axis are formed. If the ratio between anisotropy and stray field approaches $Q \cong 1$ or even $Q \ll 1$, complex closure domains are formed with magnetization vectors non-parallel to the easy axis in order to guide the magnetic field lines within the material and minimize the stray field.

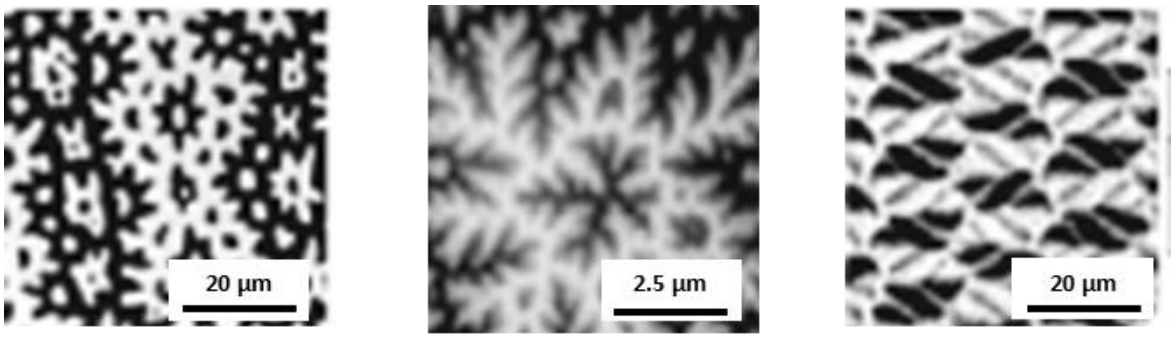

Nd-Fe-B **Cobalt** **Fe-B-Si**

$\boldsymbol{Q > 1}$ $\boldsymbol{Q \approx 1}$ $\boldsymbol{Q << 1}$

Figure 9: Classification of magnetic domain structures based on the quality factor Q. Different domain patterns are observed by Kerr microscopy on the top surface. The images show a Nd-Fe-B single crystal on the left, a Cobalt single crystal in the middle and soft magnetic, amorphous Fe-B-Si on the right. The interplay between stray field and magnetic anisotropy can lead to complex domain patterns, especially on the surface of the sample. The figure has been adapted from [51].

The difference in domain structure can be visualized and measured with the magneto-optical Kerr effect. Comparison of the domain patterns by viewing in the materials c-axis shows a strong difference in shape and size of domains. This does not only visualize the severe difference of the intrinsic magnetic properties for different materials but is also a representation for the magnetic hysteresis which, in essence, is the samples answer to excitation by an external magnetic field.

2.4. Magnetic Hysteresis

The magnetic hysteresis loop delivers several important parameters to classify and qualify materials for their technical applicability. Considering our ferromagnetic sample, it could be expected that the magnetic moments rotate proportional to the magnetocrystalline energy and energy in a magnetic field until they are parallel to the external field. A theoretical approach is given by the Stoner-Wolfarth model. It considers spherical, single-domain particles with uniaxial magnetocrystalline anisotropy. The demagnetization happens by irreversible rotation of magnetization and the shape of the hysteresis does only depend on the angle between easy axis of the particle and external field direction. In the simplest case, the field is applied along the easy axis which leads to a perfectly square shaped hysteresis where the coercivity equals the nucleation field.

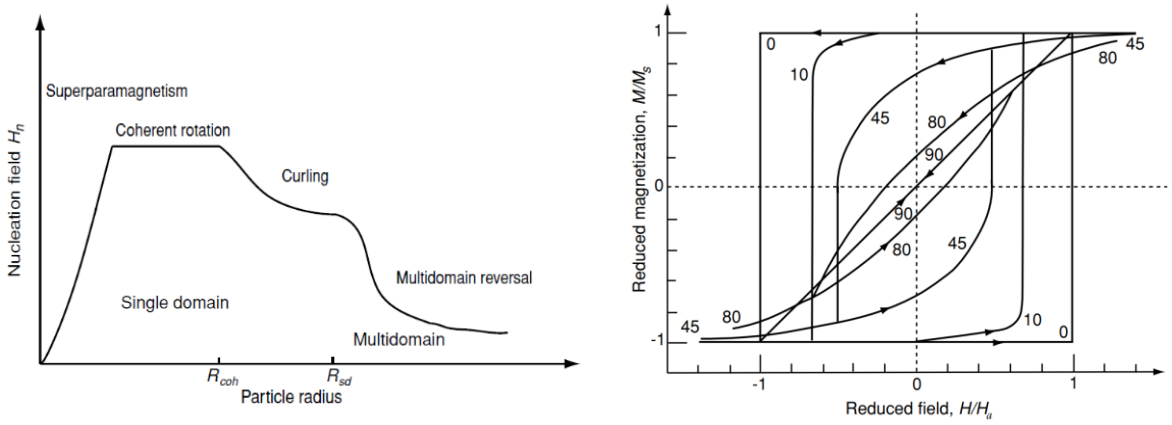

Figure 10: The nucleation field is an upper limit for the coercivity of particles and depends on their size is schematically shown on the left. The magnetization curves of an idealistic Stoner-Wolfarth particle for different angles between easy axis and external field direction is shown on the right. It shows the perfect square shaped hysteresis along easy and no hysteresis along hard axis of the particle. [50]

Due to the contribution of different microstructural features such as, grain size, texture, multiple phases and defects, the application of an external field leads to a much more complex magnetization behaviour. The domains opposite direction to the external field direction start to grow and at a certain field the sample is fully magnetized reaching the saturation magnetization M_{sat} of the material. However, the sample does not fall into its initial state after removing the external field. It possesses a remanent magnetization M_R which is an extrinsic parameter depending on the intrinsic spontaneous magnetization of the magnetic phase M_S and the microstructural features of the sample, specifically the texture. The domain structure represents a metastable magnetic state which is of great importance for the performance of permanent magnets. The stabilization of the remanent field and domain structure is the essence of

permanent magnet production. The resistance of this metastable magnetic state against external fields is represented by the coercivity H_C which is the field strength necessary to demagnetize the magnet from the remanent state. The theoretical limit of this value was derived by W.F. Brown [73] and considers only the intrinsic properties in form of the anisotropy constant K_1 and spontaneous magnetization M_S:

$$H_C \leq 2\frac{K_1}{\mu_0 M_S} - NM_S$$

Equation 10: Theoretical Limit of Coercivity

The later term NM_S represents the stray field of the sample when fully magnetized. It acts as a demagnetizing external field and depends on the sample geometry given by the factor N.

Simply put, the optimization of permanent magnets relies on the maximization of the magnetic hysteresis, namely remanence and coercivity. Whereas technical realization of a high degree of texture leads to almost ideal remanence given by the upper limit of the material's spontaneous magnetization M_S, reaching high coercivity takes much effort. This discrepancy between theory and measurement is referred to as the "Brown Paradox". All imperfections of the microstructure can be formulated in form of a temperature dependent empirical factor α which leads to the Kronmüller equation for coercivity [74]–[76]:

$$H_C = \alpha H_a - NM_s$$

Equation 11: Kronmüller Formulation of Coercivity

In this equation the interplay of anisotropy and magnetization is summarized in the anisotropy field H_a which can be practically measured and quantifies the field strength necessary to rotate the magnetization into the hard axis. The fundamental flaw of neglecting multiphase microstructures is tried to overcome since the coercivity mechanism is not only based on one magnetic phase but the interaction between several magnetic and non-magnetic phases and defects.

The magnetic hysteresis of a material contains several important information but needs always to be interpreted as a superposition of all microstructural features such as multiple phases, variation in grain size and texture. The response to the applied field H_{ext} can be displayed as the intrinsic magnetization M, the polarization $J = \mu_0 M$ or the technical relevant magnetic induction B:

$$B = J + \mu_0 H_{ext} = \mu_0 (M + H_{ext})$$

Equation 12: Relation between Magnetic Induction B, Polarization J, intrinsic Magnetization M and external magnetic field.

From this representation it is possible to formulate a figure of merit for permanent magnets, the maximum energy density $(BH)_{max}$. It is colloquially described as the stored energy in a magnet and is directly influenced by the coercivity, remanence and squareness of the hysteresis. It is based on the degree of texture (DOT) which can be easily determined by comparing the remanence along the easy and hard axis of the sample. However, the reason for the equally important coercivity is difficult to explain and is based on the several microstructural features.

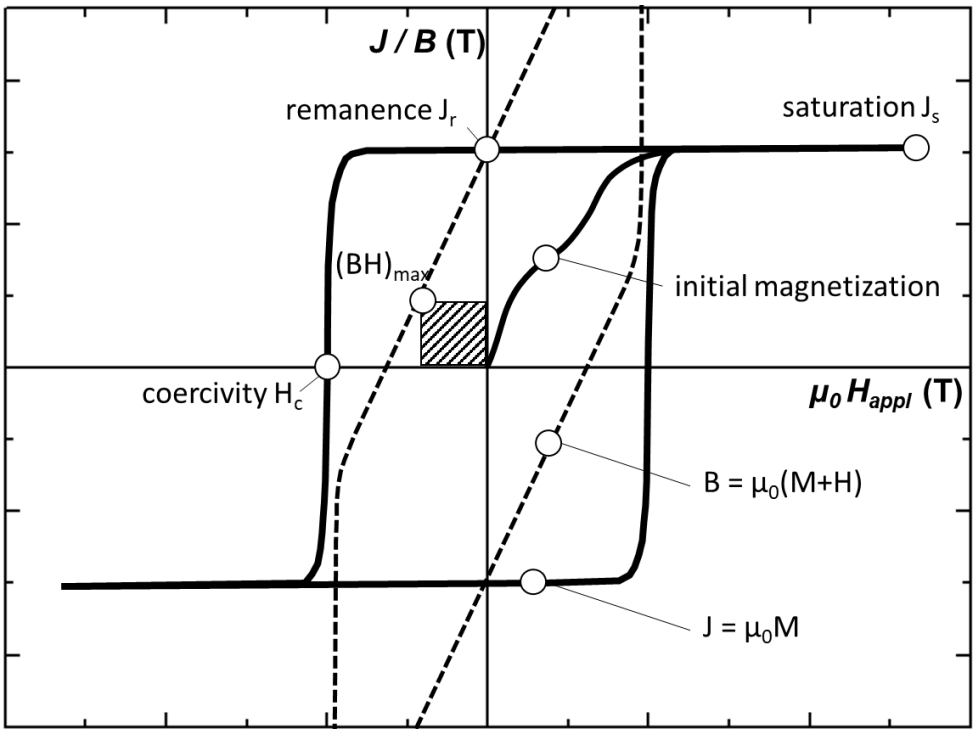

Figure 11: Magnetic Hysteresis in form of Polarization (J) or Magnetic Flux (B) over the applied field in $\mu_0 H$ for a textured, hard magnetic sample. The characteristic values coercivity H_c, remanence J_r and saturation polarization J_s are indicated. The representation of the magnetic flux $B = \mu_0(M+H)$ is shown I dashed line. In addition, the maximum energy density $(BH)_{max}$ is marked which represents the figure of merit for permanent magnets.

2.5. Coercivity Mechanism

In a real material, there are always defects which affect the physical properties. This is the reason why the coercivity will never exceed the anisotropy field H_A. Especially grain boundaries and inter- or intragranular secondary phases have a severe impact [77], [78]. In a magnet, these defects can lead to hindrance of domain wall motion or the nucleation of critical reverse magnetic domains meaning both the enhancement and/or degradation of coercivity. The theoretical description of the domain wall energy γ_W shows that deviances in exchange constant A and anisotropy constant K_1 by introducing secondary magnetic phase can have a strong attractive or repulsive effect on the domains and their movement, which is used in Sm-Zr-Co-Fe-Cu precipitation hardened magnets.

$$\gamma_w = 4\sqrt{AK_1}$$

Equation 13: Domain Wall Energy.

Especially planar and nanoscale inhomogeneities whose size is in the range of the domain wall width δ_w show strong pinning effects and increase in coercivity. The field needed to overcome or release the domains from their pinned state is the pinning field H_P. For example, the initial magnetization curve of Sm-Zr-Co-Fe-Cu magnets starts less steep if the pinning mechanism is high, as depicted in Figure 12. The domains are pinned until H_P is reached, above which the domains can move in the material and the magnetization increases. The coercivity of pinning-type magnets shows a weak dependency on the maximum applied field because the pinning field will always be the same.

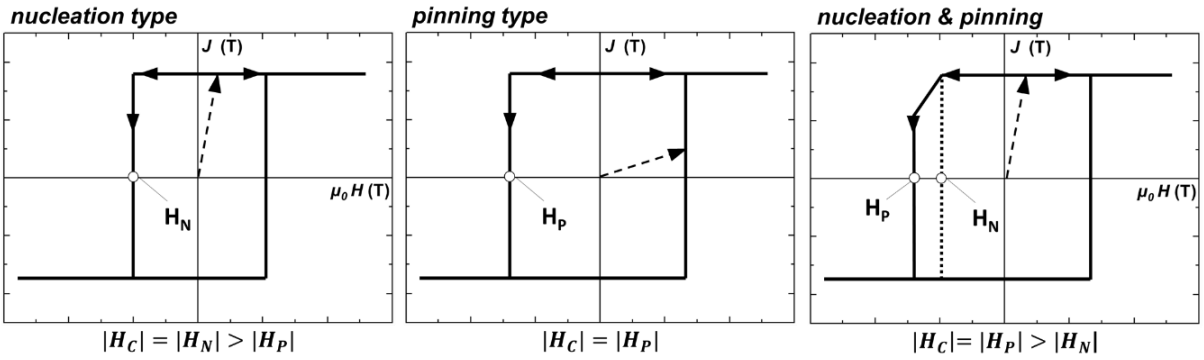

Figure 12: Schematic magnetic hysteresis of a nucleation type magnet (left) and a pinning-controlled magnet (middle). The nucleation-type magnet is characterized by a high low-field susceptibility due to reversible domain wall motion, whereas pinning sites inhibit the free motion of the domain walls and lead to a lower magnetization in pinning-type magnets. The coercivity is determined by the nucleation- or pinning field respectively. The hysteresis on the right shows a mixture of both mechanisms. Within the sample, demagnetization nuclei form at the nucleation field, but they are still pinned by defects. A shoulder in the demagnetization curve is visible and the coercivity is determined by the pinning field. The sketches have been adapted from Buschow [72].

However, the mechanism of coercivity is not only determined by pinning mechanism. Another coercivity mechanism is based on nucleation of reverse magnetic domains. In sintered Nd-Fe-B magnets, the approach in production is to obtain a microstructure based on defect free grains which are separated by a (usually RE-rich) grain-boundary layer. From the thermally demagnetized state, the magnetic structure of the grains is divided into magnetic domains, which leads to a zero net-magnetization. Applying a field leads to a sharp increase in the magnetization, because there are no pinning centers within the grains, meaning that H_P is very low. To demagnetize a single grain after reaching full saturation, a critical field H_N is required, which is able to induce a reverse magnetic domain. Nucleation-type magnets show lower coercivities when they are not saturated, because the number of reverse-magnetic domains is higher and more grains are demagnetized easily [48], [79]. In reality though (even after full magnetization), there will always be grains with reverse-magnetic domains and defects which lower the effective H_N and therefore the H_C of the macroscopic magnet. To understand the unique magnetic performance, the coercivity mechanism and the elaborate production techniques of Nd-Fe-B magnets, it is necessary to start from the phase diagram and intrinsic properties of the material system [7].

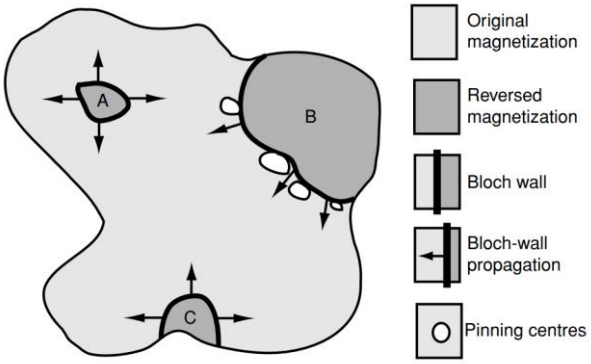

Figure 13: Schematic of demagnetization and domain movement processes involved in the coercivity mechanism. The nucleation of reverse magnetic domains can happen at defects within the grain (A) or at the grain surface (C). Pinning centers are hindrances to domain wall motion (B). [50]

2.6. The RE-Fe-B System

The hard magnetic properties of Nd-Fe-B based magnets is based on the intrinsic magnetic properties of the $Nd_2Fe_{14}B$ phase. It possesses a strong uniaxial magnetocrystalline anisotropy along its c-axis of the tetragonal unit cell with space group $P4_2/mnm$. It is important to mention that crystal structure is specific and not related to any know binary Nd-Fe phase. The boron atoms are the reason for the formation of this phase and take specific sites in the crystal structure. Regarding the magnetic properties, the Nd atoms are the reason for the high anisotropy. On the other hand, high saturation magnetization is based on the parallel coupling between Nd atoms and the large magnetic moments of Fe atoms which translates into the high remanence of such magnets. The Curie Temperature of 312 °C is relatively low, which is the reason for the limited temperature stability of such magnets. Since RE atoms take dedicated sites in the unit cell, the coupling between RE and Fe is the reason for the strong variety of the intrinsic magnetic properties in the $RE_2Fe_{14}B$ series. As already mentioned, heavy RE like Dy or Tb are used to increase coercivity and temperature stability due to their higher anisotropy field and Curie temperature.

Table 3: Intrinsic properties of $RE_2Fe_{14}B$ compounds at room temperature. [80]

$RE_2Fe_{14}B$	T_C (K)	$\mu_0 H_a$ (T)	K_1 (MJ/m^3)	J_s (T)
Y	571	2	1.1	1.41
La	530	2	-	1.27
Ce	422	3	1.44	1.17
Pr	569	8.7	5.5	1.56
Nd	586	6.7 [81] 7.3 [82] 8 [9]	4.5	1.6
Gd	659	2.5	0.9	0.89
Tb	620	22	5.9	0.66
Dy	598	15	4	0.71

The speciality of the $Nd_2Fe_{14}B$ (ϕ phase) is its distinct formula unit. It is a line compound, meaning that it shows a narrow homogeneity region. The modification of this phase and influence of elemental additions is based on the substitution of RE or TM cites in the unit cell. Especially the use of RE mixtures is of technical interest. So called Mischmetal-Fe-B magnets can contain several unseparated RE elements such as La, Ce, Nd, Pr and heavy RE. The aim is to develop low-cost magnets and to find beneficial combination of RE regarding the magnetic properties [83]–[88]. Although this is ongoing research, state-of-the-art Nd-Fe-B based magnets usually contain Pr. In fact, the Nd- and Pr-Fe-B phase diagrams look very much alike which is based on the chemical similarity of the RE elements in general and Nd & Pr in particular.

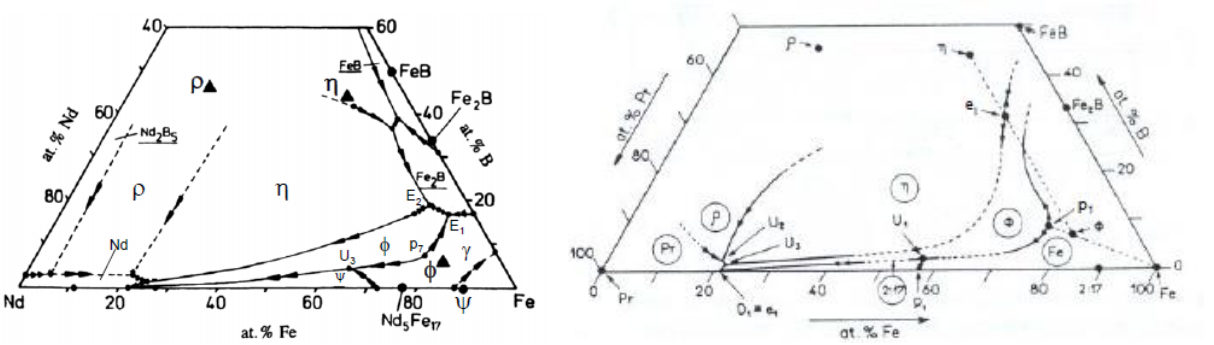

Figure 14: Ternary phase diagram as liquidus projections in the Nd-Fe-B (left) [89] and Pr-Fe-B (right) [90] systems. Both compounds show similar temperature profiles and same occuring phases. Most importantly, the peritectic reactions from $L + \gamma - Fe \rightarrow \phi$ occur at 1180 °C for the Nd- and at 1125 °C for the Pr-based system.

The intrinsic magnetic properties of the $Pr_2Fe_{14}B$ phase shows slightly lower Curie Temperature and saturation magnetization, however, much higher anisotropy field which can increase the coercivity of the magnet. An important advantage arises at low temperature. Whereas the $Nd_2Fe_{14}B$ phase shows a spin reorientation transition at 135 K which leads to a drastic decrease in magnetic hardness, the $Pr_2Fe_{14}B$ phase does not show a spin reorientation and is therefore interesting for the use at low temperatures.

2.6.1. Elemental Modifications

Although the intrinsic magnetic properties of the ϕ-phase are the essence for Nd-Fe-B based permanent magnets, the goal is a specific microstructure which provides high magnetic performance. In order to improve and optimize the magnets, several elemental modifications have been explored and found to have beneficial influence on remanence, coercivity but also properties such as corrosion resistance. Besides elemental substitutions which replace the RE, TM or B site in the unit cell, other elements show only a low solubility, therefore known to form intergranular phases. Following the nomenclature by Fidler & Schrefl [91] the elements can be distinguished into “Type 1 dopants (T1)” which form RE-TM-T1 phases and “Type 2 dopants (T2)” which form boride phases. The latter group contains elements such as Mo, W, Ta, Zr, V, Ti and Nb. In permanent magnets, these elements are used to decrease grain size and improve corrosion resistance. All of these elements form intergranular T2-Fe-B phases and do not solve in the ϕ-phase. The Type 1 group of elements is known to affect the decoupling of the ϕ-grains by forming low melting eutectic. Associated elements such as Al, Ga and Cu improve the wetting behaviour and enhance the coercivity of the magnets. Practically, the addition of such elements does directly affect the annealing treatment of magnets due to the low melting point of the grain boundary phase. This influence is of special interest in this work since the **Pr-Fe-B** system is known for its high coercivity in as-cast, bulk material by **high Cu addition** to the ternary system.

2.6.2. The Pr-Fe-Cu-B System

Research has shown that it is possible to form secondary $Pr_6Fe_{13}Cu$ and Pr_2Fe_{17} phases in certain regions of the Pr-Fe-Cu-B phase diagram [21]. The characteristic of this complex microstructure is the well separated $Pr_2Fe_{14}B$ grains embedded in a thick matrix of Pr-Cu rich eutectic phase

and $Pr_6Fe_{13}Cu$. The interesting finding is that high coercivity cannot only be reached by hot deformation but by careful annealing at high temperature (1000 °C) followed by low temperature annealing (500 °C) [19]–[27], [92]. Although this compound is a special example due to its high Pr and Cu content, recent studies on commercial magnets with addition of Cu, Al and Ga explain the high coercivity by formation of $(Nd,Pr)_6Fe(Cu, Al, Ga)_{14}$ and low melting eutectics [28], [29], [93], [94] and agree with the important role of "Type 1 dopants" on the magnetic properties of the magnet. It has to mentioned that the magnetic properties of the secondary $RE_6Fe_{13}(Cu, Ga, Al)$ phase is not clear and is believed to be either para- or antiferromagnetic.

2.6.3. The Effect of Cobalt in (Nd,Pr)-Fe-B

For the production of Nd-Fe-B based magnets, Cobalt is a relevant substitution for Iron due to its beneficial properties on the magnetic properties and corrosion resistance [91][95]. The $Nd_2(Fe_{1-x}Co_x)_{14}B$ compounds are stable over the whole substitutional range in the tetragonal structure where the lattice parameters decrease with increasing Co content. The most important effect is the increase in Curie temperature due to the stronger Co-Co exchange coupling compared to Fe-Fe. Furthermore, the spontaneous magnetization M_s has a maximum around 20 at% Co substitution, however, the anisotropy field H_a is decreasing throughout the whole substitutional range. Therefore, the coercivity is decreasing drastically and only small substitution by Co is beneficial and applicable for magnet production [96]. Contrary to the increase in T_C, the spin reorientation temperature shifts to lower temperatures (37 K) where the uniaxial anisotropy transitions into a canted order.

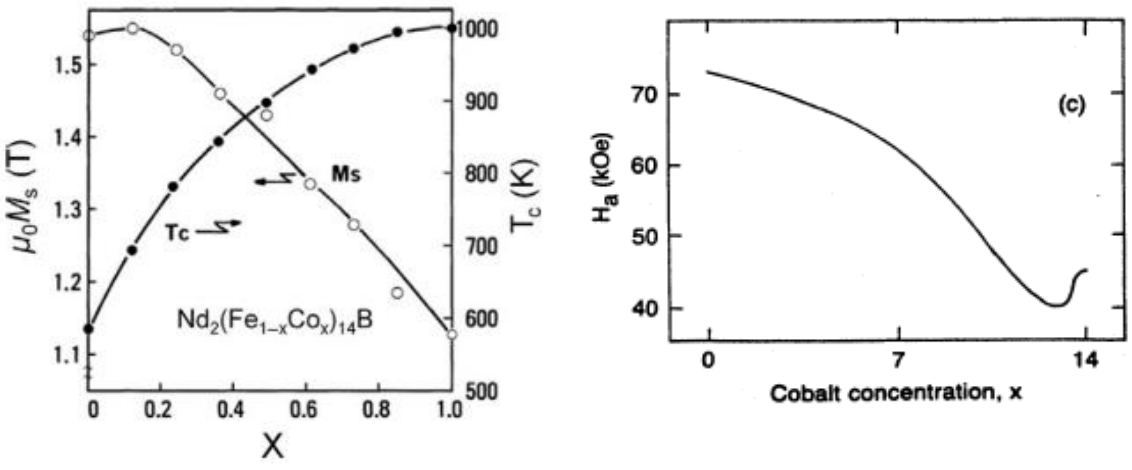

Figure 15: Magnetic properties of $Nd_2(Fe_{1-x}Co_x)_{14}B$ depending on the Cobalt content. The left graph shows the spontaneous magnetization and Curie Temperature [80] , the right graph the decreasing anisotropy field [97].

Like in $Nd_2(Fe_{1-x}Co_x)_{14}B$ compounds, the Pr-based counterparts show full substitution of Fe by Co and the increase in Curie temperature is similar. However, the anisotropy field is much higher for $Pr_2Co_{14}B$. Together with the high Curie temperature, Pr-Co-B based compounds are interesting candidates to produce high temperature magnets and could close the gap between Nd-Fe-B and high temperature Sm-Co magnets.

Besides the effect on the magnetic properties, Co is known to stabilize secondary phases in the Nd-Fe-B [98] and Pr-Fe-B system [99]. Melt spinning experiments have shown, that the Laves

$Nd(Fe,Co)_2$ phase, $Nd(Co,Fe)_4B$ and a $Nd_2(Fe,Co)_{17}$ are formed at high Co substitution above 20 at%. Although a beneficial effect by increasing remanence up to 30 % and increasing Curie temperature has been found, the coercivity decreased drastically, which was assigned to the formation of (soft magnetic) secondary phases. However, the metastable $Nd_2(Fe,Co)_{17}B_X$ phas is of special interest in this work. Due to the absence of a intermetallic phase with high melting point in the Nd-Fe-B system, the possibility of a phase decomposition and precipitation hardening effect are not obvious and at hand, therefore nano-scale microstructural features and pinning effects like in Sm_2Co_{17} based magnets are not realized. The formation of a metastable phase by alloy modification and controlled solidification processes would allow to achieve unexplored microstructures and magnetic properties in Nd-Fe-B based material.

2.6.4. Metastable $Nd_2Fe_{17}B_x$ Phase in Nd-Fe-B Alloys

The relevant phase region for Nd-Fe-B magnets is located close to the $Nd_2Fe_{14}B$ phase in order to utilize the hard magnetic intrinsic properties and maximize the magnetic performance. In equilibrium, the primary solidification of γ-Fe is tried to avoid by high cooling rates and followed by the peritectic $Nd_2Fe_{14}B$ reaction. However, several authors [30]–[36], [38]–[47] have shown the formation of a metastable $Nd_2Fe_{17}B_x$ phase which forms by high undercooling of the melt. This metastable is related to the binary Nd_2Fe_{17} compound which crystallizes in the Th_2Zn_{17} structure. The solution of Boron in this phase is believed to change the crystal structure to the hexagonal $TbCu_7$ and increase the Curie temperature compared to the binary phase. However, the Boron content is yet unclear which is the reason for the unknown parameter x in $Nd_2Fe_{17}B_x$.

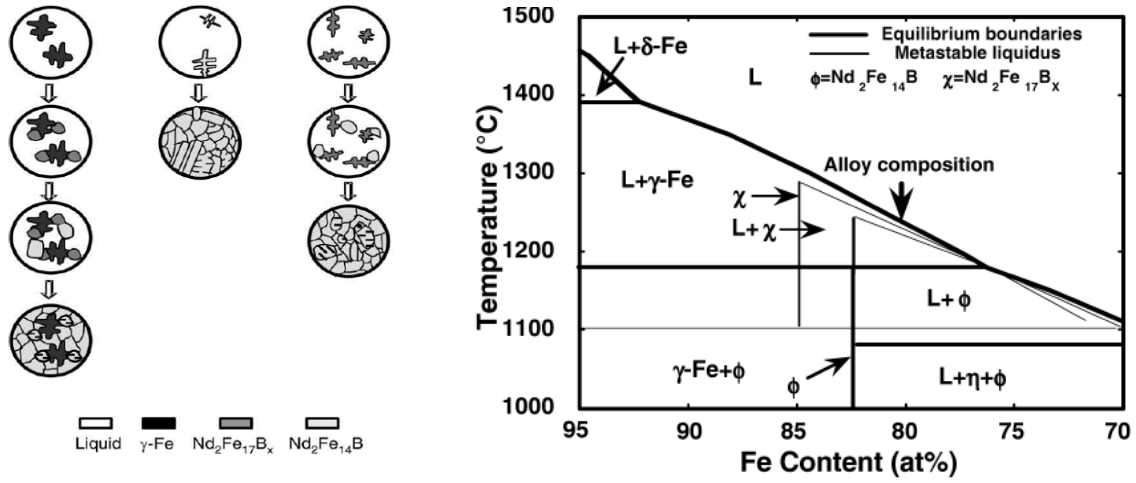

Figure 16: The sketch on the left shows the primary formation of Iron and subsequent peritectic formation of 2:17:x phase followed by its decomposition to Iron and 2:14:1 on the left as stated in [42]. The primary formation of 2:14:1 is shown in the middle and the primary formation of metastable 2:17:x followed by its decomposition on the right. The phase diagram shows the metastable phase region in the quasi-binary Nd-Fe-B system by undercooling of the melt [33].

The previous experimental work is based on containerless solidification methods such as drop-tube technique or electromagnetic levitation. These techniques aim for a homogeneous nucleation of crystals in the melt and reach higher undercooling compared to conventional

solidification by casting, where heterogeneous nucleation dominates the solidification process. Based on the microstructure and the dendritic formation of the metastable phase, the competing growth of γ-Fe, $Nd_2Fe_{14}B$ and the metastable $Nd_2Fe_{17}B_x$ phase could be shown as depicted in Figure 17. Often, the reported microstructure consisted of all 3 phases and the stabilization of the metastable phase could be shown by high substitution of Fe with Co. Most importantly, the transformation of the metastable phase was observed, leading to the formation of $Nd_2Fe_{14}B$ and fine dispersed α-Fe phase. This reaction happened indirectly by recalescence during solidification. The underlying mechanism of stabilizing a high temperature phase which is able to be transformed by heat treatment is fundamentally new in the Nd-Fe-B system. It could enable the realization of nano-scale microstructure and precipitation which can participate in the coercivity mechanism. The effect on the magnetic properties and utilization towards Additive Manufacturing is explored in this work.

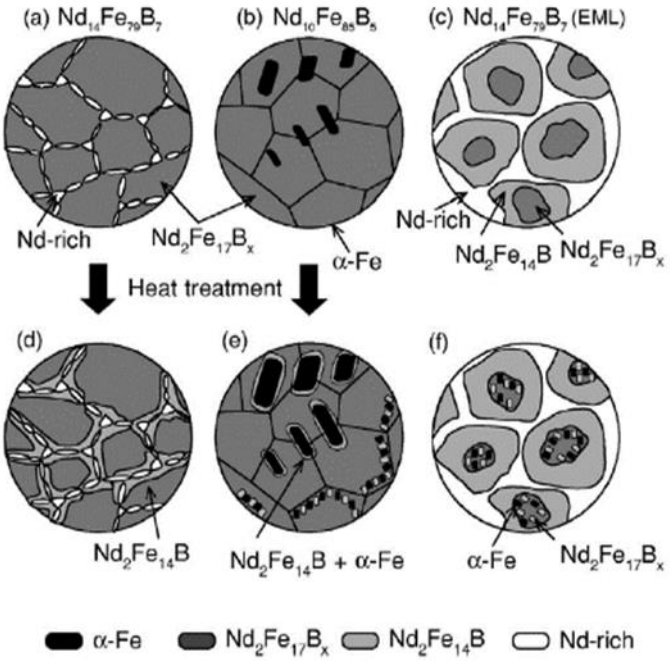

Figure 17: Transformation mechanism of metastable χ -phase proposed by Ozawa et al. [44]. The compositions on the left (a) and (b) were investigated after drop-tube experiments. Composition (a) shows $Nd_2Fe_{17}B_x$ grains with Nd-rich phase at the grain boundaries. The heat treatment leads to the formation of $Nd_2Fe_{17}B_x$ phase at the interface between $Nd_2Fe_{14}B$ and Nd-rich phase. Composition (b) with the $Nd_2Fe_{17}B$ stoichiometry shows α-Fe. The heat treatment leads to $Nd_2Fe_{14}B$ phase surrounding the α-Fe phase or fine dispersed α-Fe and $Nd_2Fe_{14}B$ precipitations. Composition (c) is a based on electromagnetic levitation (EML) experiments. The amount of $Nd_2Fe_{17}B_x$ is lower and core-shell structure with $Nd_2Fe_{14}B$ and Nd-rich phase is observed.

2.7. Commercial Production of Nd-Fe-B Permanent Magnets

The unique phase diagram of the Nd-Fe-B system is the reason for its nucleation based coercivity mechanism and the powder metallurgical production. In thermodynamical equilibrium, the $Nd_2Fe_{14}B$ forms at a peritectic point at 1180 °C from the primary solidification product γ-Fe and liquid. The soft magnetic Fe phase has a severe impact on the magnetic performance due to a drastic decrease in coercivity. Therefore, the magnet production starts usually with rapid solidification techniques such as strip casting, book mould casting or melt spinning in order to suppress the formation of Fe phase. Moreover, the alloy compositions of commercial magnets

are close to the $Nd_2Fe_{14}B$ phase, with a slight surplus in RE content. It is known that the coercivity increases with increasing RE content which is explained by the decoupling of $Nd_2Fe_{14}B$ grains and the reduction of defects on the grain surface. However, the produced precursor material can be very different in its microstructure and magnetic properties and needs to be adjusted for the subsequent consolidation method. Generally, the Nd-Fe-B magnet production can be divided in the nano-crystalline approach based on hot deformation and the macro-crystalline route which means the powder metallurgical sinter-process of fine-grained powders [7], [80], [100], [101].

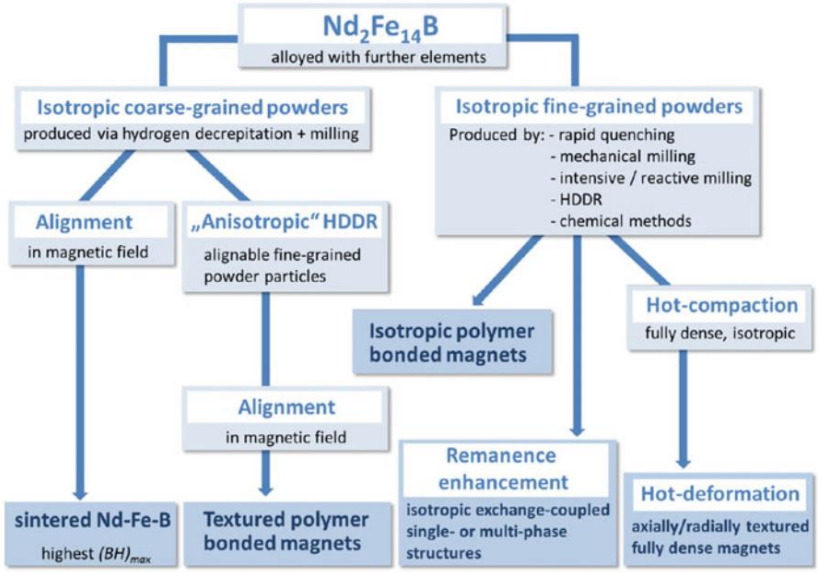

Figure 18: Different approaches for the production of Nd-Fe-B permanent magnets in form of a flow chart. The coarse-grained powders result in textured sintered magnets with highest $(BH)_{max}$. On the other side, nano-grained powders, commercially prepared by rapid solidification, are used for hot deformed magnets. The chart was taken from [51] and is adapted from [7].

2.7.1. Nano-Crystalline Approach

Although nano-crystalline Nd-Fe-B based material can be produced by several techniques, especially mechanical alloying [102] or Hydrogenation-Disproportionation-Desorption-Recombination (HDDR) process [103], the commercial usage relies on rapid solidification techniques and subsequent hot compaction. The resulting magnets are produced by hot compaction and deformation of nano-crystalline, partially amorphous powders which are commercially obtained by high cooling rates during melt spinning [104]. The material is solidified from the fully melted state on a rotating Cu-wheel (which can be coated with refractory metals) with cooling rates in the range of 10^5-10^6 K/s [105], [106]. The resulting microstructure depends strongly on the parameters during the process such as wheel speed, nozzle geometry and output pressure. For the hot deformation route, a partially amorphous and nano-crystalline microstructure is wanted although it should be noted that the amorphous content is decreasing in newer batches of the commercial powders, possibly driven by the cost saving in shortening the process time during hot pressing. The subsequent hot compaction is needed to consolidate the material to a fully dense, isotropic magnet. Therefore, the compaction temperature is usually just above the melting temperature of the Nd-rich grain boundary phase. A subsequent uniaxial deformation step is necessary to achieve a texture and therefore high remanence of the magnet. The reason is based on the anisotropic elastic constants of the

$Nd_2Fe_{14}B$ phase which enable the preferred grain growth along the a-b plane of the tetragonal unit cell induced by uniaxial pressure. This effect is described by the "Solution-Precipitation-Creep-Model" [107] and results in platelet shaped $Nd_2Fe_{14}B$ grains in the range of several hundred nanometer. The magnetization process is very different from sintered magnets and is based on the formation of interaction domains. The maze like structure consists of domains of hundreds of microns in size, much larger than the actual grain size of $Nd_2Fe_{14}B$ phase in the hot deformed samples [108], [109]. These characteristics indicate, that the coercivity mechanism is not only nucleation-based and different from the governing mechanisms in sintered magnets [7]. Theoretical works describe the pinning effect of planar defects, such as grain boundaries [110], but a straightforward explanation for the coercivity mechanism of nanocrystalline magnets is complicated and has to be separated from the classical nucleation and pinning based description [111]. However, the directly measurable advantage of hot deformed magnets is found in their high temperature stability in remanence and coercivity [112]–[115] compared to sintered magnets.

2.7.2. Micro-Crystalline Approach

Whereas magnets based on the nano-crystalline approach take only a small share of the commercial Nd-Fe-B market, the most relevant technique is based on sintering fine powders which leads to highest magnetic performance [116]. This approach aims directly for an optimal microstructure of well separated and decoupled grains [117] resulting in a nucleation controlled coercivity mechanism. The starting composition already accounts for the formation of a grain boundary phase and RE containing secondary phases and impurities by considering slightly higher RE content compared to the stoichiometric $RE_2Fe_{14}B$ composition. The production usually starts with strip casting of a pre-alloy. Thereby, the formation of soft magnetic Fe phase is suppressed by high cooling rates. The strip cast flakes are several hundred μm in thickness and contain dendritic grains of the $RE_2Fe_{14}B$ phase. Before the mechanical milling, the flakes are subjected to the Hydrogenation Decrepitation (HD) process. The strong reaction with hydrogen and volume expansion leads to the decrepitation of the flakes. After a heat treatment, the hydrogen is desorbed again and the resulting powder is very brittle and has a sufficient size for the jet milling process [103]. Most frequently, the powder is milled by interparticle collisions of opposing gas streams (jet milling). The particle sizes for sintered magnets are usually in the range of 5 μm although newer approaches aim towards ultra-fine-grained magnets with 1 μm grain size. After preparation of suitable powder, green bodies for sintering are pressed. The practical realization can vary depending on the geometry of the magnet but always incorporate the alignment of the particles in a magnetic field. During this step, the texture is induced and remanence of the magnet is achieved. Conventional pressing of green bodies is done in dies or rubber forms [118] with ideally isostatic pressure. However, recent developments are based on ultra-fine-grained powders which enable a pressless consolidation due to high sintering activity of the fine particles [119]–[121]. In general, the sinter process is based on liquid phase sintering mediated through the RE surplus. The sintering temperature is optimized for each composition but always happens in the $\phi + L$ phase region. It has to be high enough for full densification but as low as possible to prevent (abnormal) grain growth. In order to develop full coercivity, post-sinter annealing (PSA) treatments at lower temperatures are performed. Although the reason for the necessity of such heat treatments is still under discussion, recent studies have proven the fully reversible effect on the magnetic

properties during short-term heat treatments which exclude long-range diffusion processes. The work suggests, that the low temperature annealing leads to a full wetting of the grains and the healing of defects on the grain surface [122].

In general, the commercial production of Nd-Fe-B magnets is based on careful production steps especially the processing of precursor material for either nano- or macro-crystalline approaches. The initial composition depends on the required magnetic performance but also on the production technique itself. Besides controlled modification of the intrinsic magnetic properties by elemental substitutions, an important aspect to increase the coercivity is the reduction in grain size [80]. In this regard, it is necessary to introduce the critical grain size for single domain particles.

$$D_C = 72\frac{\sqrt{AK_1}}{\mu_0 M_s^2}$$

Equation 14: Critical Grain Size for Single Domain Particles.

Regarding the theoretical view based on the Stoner-Wolfarth model, highest coercivity is expected for single domain particles. However, experimental and theoretical work shows that coercivity follows a $1/lnD^n$ proportionality [123], [124] for Nd-Fe-B magnets. Besides artificial thin films, the data shows a strong discrepancy between theory and measured coercivity. For $Nd_2Fe_{14}B$, the critical domain size is ~300 nm which is in the region of melt spun ribbons or hot deformed magnets. However, the coercivity is comparable to sintered magnets with grain size of several μm, indicating that there is still room for improvement. The unobvious reason seems to be based on the defect density in the microstructure [102]. Especially the high reactivity of the RE leads to oxidation and pick-up of C and N which has a severe deteriorating effect on the coercivity. The necessity of a clean environment and protective atmosphere during production is an important factor for the conventional production techniques and even more for novel techniques such as Additive Manufacturing.

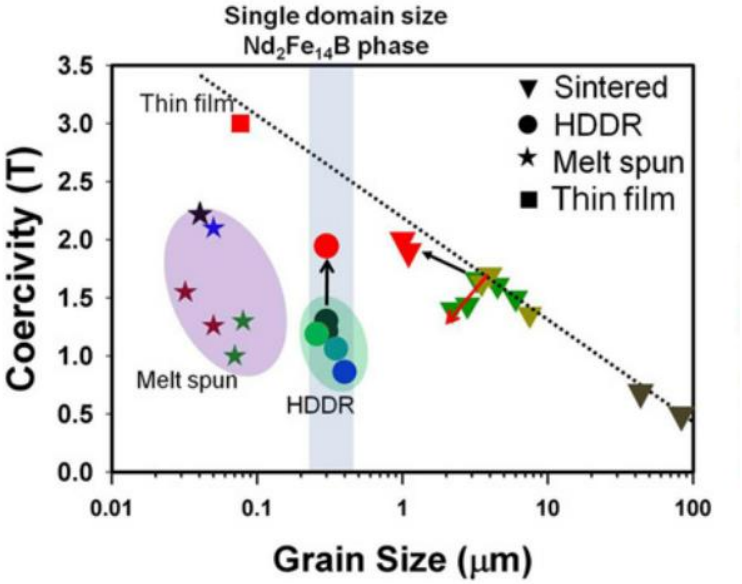

Figure 19: Coercivity in dependence on the grain size in Nd-Fe-B magnets. Below grain sizes of 1 µm for ultra-fine grained sintered magnets, the coercivity does not follow the predictions. Even more, the nano-crystalline hot deformed magnets reach only coercivities similar to sintered magnets. [101]

2.7.3. Towards Additive Manufacturing of Nd-Fe-B Magnets

Before diving into additive manufacturing of permanent magnets, it is necessary to introduce the relatively young field of AM. Initially, 3D printing served as “Rapid/ Fast Prototyping” technique but increasing number of technological variations and quality of the components led to the general term “Additive Manufacturing”. The rapid development and commercialisation of AM is leading to increasingly complex demands. Especially the processing of functional materials, which is also referred to as 4D printing, poses a great challenge. Apart from the production of complex 3D geometries, the components should interact with their environment, which is represented as the fourth dimension. The most significant and meaningful opportunity of this technique is the realization of complex geometries, print-in designs, locally tailored physical (magnetic) properties and components with response to external triggers while retaining a resource efficient use and fabrication. The reason for this relies solely on the manufacturing process itself. The 3D printing refers to the layer-by-layer building of a component. Since each layer has a certain thickness, a body is produced that corresponds to an approximation of the ideal Computer-Aided Design (CAD) model. In order to realize a component coming from the CAD model, the process chain includes a digital translation into Standard Triangulation/ Tesselation Language (STL) which is then transferred to a sliced, layered version of the CAD model.

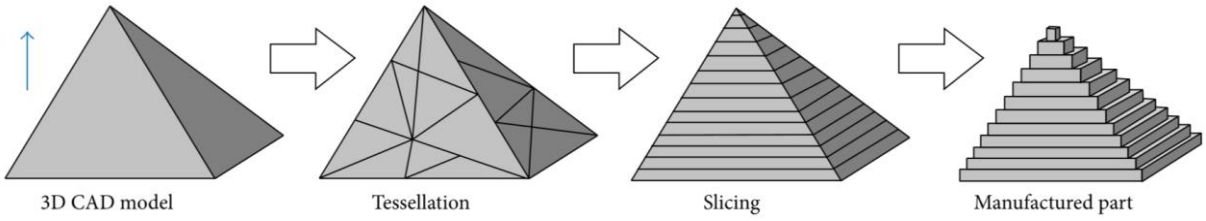

Figure 20: Practical realization of a printed component based on the computer added design, digital translation, slicing and final manufacturing. The blue arrow indicates the build direction. [125]

Additive Manufacturing is an umbrella term which contains various technologies. The most interesting technique for structural (and functional) metals is Laser-Powder-Bed-Fusion (PBF-LB), which allows to produce fully dense metallic components without the use of a binder material.

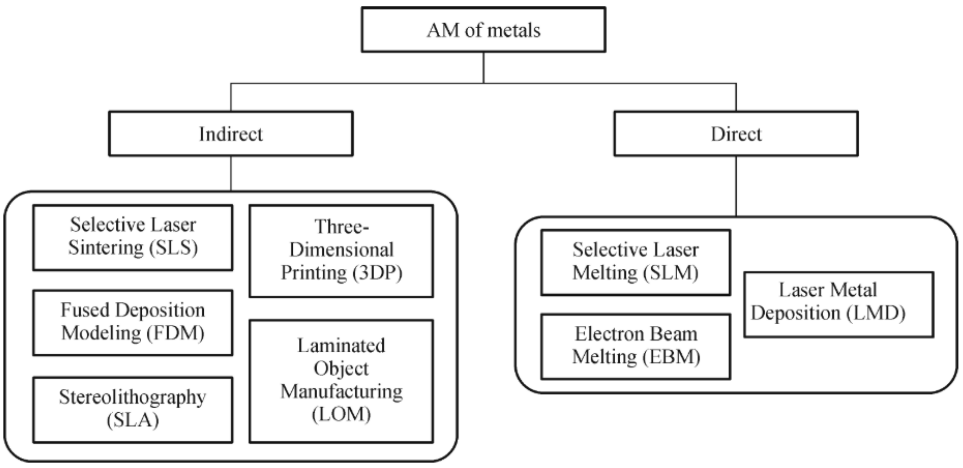

Figure 21: Classification of Additive Manufacturing of metals based on the use of binders (indirect) or full melting of the metal. The indicated “Selective Laser Melting (SLM)” equals Powder-Bed-Fusion by Laser Beam (PBF-LB) process. [126]

The process is based on repeated single-layer laser exposure and consolidation of metal powder. The powder bed is created by a coater which is then locally melted by means of a laser and scanner unit. When the melt solidifies, a firmly fused layer is formed. This is repeated until the component is built to its final shape. Due to the local melting process by the laser and repeated heat inputs, complex and difficult to predict processes and microstructures occur during solidification as indicated in Figure 22.

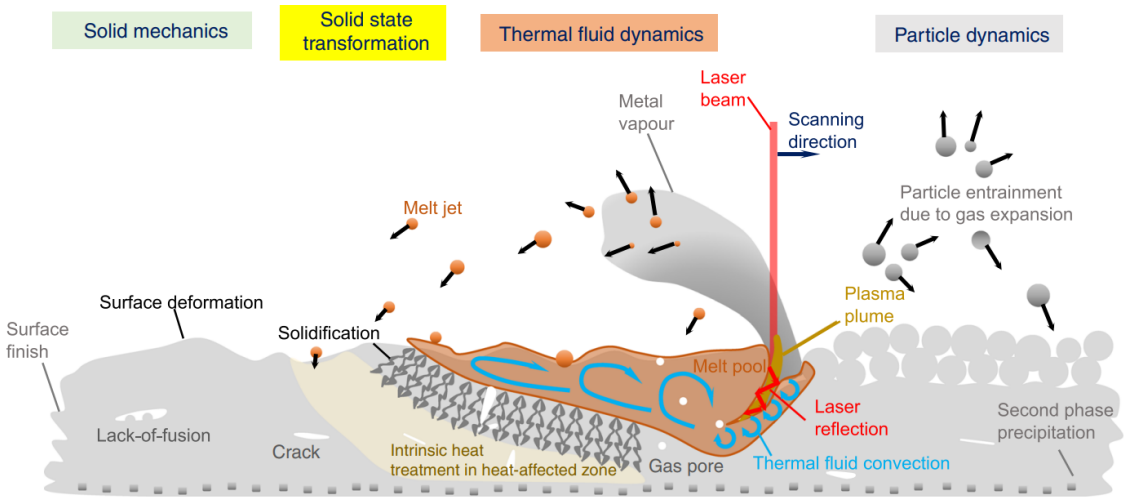

Figure 22: Schematic visualization of phenomena during PBF-LB. The complex process of liquification by a laser and rapid solidification depends on solid mechanics, solid state transformation, thermal fluid dynamics and particle dynamics. It is difficult to predict the material behavior beforehand, making the optimization process of the processing parameters unavoidable. [127]

The successful printing process depends on several tuneable parameters. The first important consideration is based on the powder size distribution resulting in the layer thickness D_S during printing. Typically, the powder particle size ranges between 20 – 80 μm which translates to a D_S usually below 100 μm. The powder is applied using a roll, brush, blade or manually where the latter option is especially reasonable for small amounts of non-spherical powders. The laser is guided by dedicated scanning optics and follows defined paths which are designed depending on the geometry. Furthermore, the hatch distance h_s displays the distance between the laser paths. Together with the variable laser power P_L and the scan velocity v_s it is possible the calculate a comparable equivalent between all parameters, the volume energy E_V:

$$E_V = \frac{P_L}{v_s * h_s * D_S}$$

Equation 15: Formulation of the Volume Energy for Laser Powder Bed Fusion.

The optimal processing window is narrow and several effects such as specific evaporation of elements, crack formation due to residual stresses and inhomogeneity within the microstructure must be overcome. In this context it becomes apparent, that the AM of permanent magnets is not a trivial task and includes several obstacles in the processing chain.

The main challenge which arises when PBF-LB is used to build Nd-Fe-B magnets consists of an unsuitable microstructure that appears after the re-melting and fast solidification processes resulting in low coercivity values. In comparison, commercial Nd-Fe-B sintered magnets are based on advanced and optimized microstructures achieved by controlled powder metallurgical processes [7]. The alloy design and powder production are optimized for this process and cannot easily be transferred to AM. The hard magnetic properties of the magnets are based on

a specifically adjusted microstructure, which can only be realized through the complex and well controlled processing steps, especially heat treatments, during the sintering process or hot deformation. For this reason, the production of PM using direct additive manufacturing methods (such as PBF-LB) without binder material has not been commercialized so far.

Most research in this field is based on the processing of a commercial magnetic powders optimized for the production of polymer-bonded or sintered magnets, MQP-S [16], [128]. The reason is, that MQP-S is the only commercially available spherical magnetic powder. However, the alloy composition is optimized for the manufacturing process (atomization) and shows maximum coercivity and remanence right after the solidification. Subsequent melting of the material during PBF-LB destroys the microstructure and the hard magnetic properties are lost [129]. Although the consolidation of dense samples is possible, these do not show any relevant hard magnetic properties. Subsequent heat treatments do not show to improve the magnetic properties. The only possibility to maintain the hard magnetic properties is the subsequent diffusion of RE [130]. However, this is not possible for all geometries and limits the possibility of "print-in" designs and complex component layouts, as homogeneous diffusion cannot be guaranteed.

Other research on conventional Nd-Fe-B compositions processed by PBF-LB agrees, that the parameter space for printing is narrow and non-spherical powders are difficult to process. Although the coercivity can reach reasonable values, all samples are isotropic and have low $(BH)_{max}$. Still, AM is currently an emerging research field that can revolutionize the production and use of permanent magnets. [16], [128], [130]–[142].

3. Sample Preparation and Experimental Methods

The experimental approach in this work consists of a specific alloy design and elemental modification of (Nd, Pr)-Fe-B alloys towards Additive Manufacturing. Therefore, the practical approach and characterization on lab-scale includes alloying, annealing treatments and magnetic and microstructural characterization. After deciding for suitable compositions, the upscaling of sample batches was realized. The following chapter gives an overview on the used techniques and motivates the use of certain equipment and experiments.

3.1. Alloy Preparation and Heat Treatments

All experiments in this work are based on lab-scale optimization processes. The first step, coming from pure elements, is the alloying. This was done by melting high purity elements in an induction melter (Reitel) under protective Argon atmosphere. On lab-scale, batches of ~25 g are prepared in Al- or Zr-oxide crucibles.

For homogeneous distribution of high melting elements or modifications of already alloyed precursor material (e.g. strip cast flakes), arc melting was performed using a Buehler MAM-1 Arc Melter. The samples were melted by high currents between a tungsten cathode and the sample, which is grounded on a water-cooled Cu-plate. Besides higher compositional homogeneity, the advantage is the possibility of using suction casting method. Therefore, a Cu mold with a cavity of 4 x 0.5 mm in size was inserted in the Cu water-cooled base plate. Attached to the Cu mold is a secondary vacuum chamber which provides the under pressure to suck the liquid metal into the Cu mold. The cooling rates are estimated to reach orders of 10^3 K/s based on previous works [143]–[145] due to the (in comparison) small cavity and large cooling surface of the Cu mold used in this work. This technique was especially used to test the influence of high cooling rates, similar to the Laser Powder Bed Fusion, on the magnetic properties of the sample material. As-cast samples were used to optimize the composition and annealing treatments for additive manufactured samples.

Due to high reactivity of RE elements, all subsequent annealing treatments were performed under protective atmosphere. The samples were sealed in high purity quartz crucibles under Argon atmosphere. The heat treatments were performed in Carbolite tube furnaces which provide temperature stability and homogeneity within the heating chamber.

3.2. Powder Preparation

As the term Laser-Powder-Bed-Fusion already implies is the additive manufacturing based on powder consolidation. For commercial purposes, the powders are produced by atomization techniques. However, such elaborate techniques require large and advanced equipment and result in minimum batch sizes of several kg. The alloy development and optimization process are therefore cost and time consuming. In this work, the alloys under investigation were mechanically milled, resulting in non-spherical powder. A Hosokawa Alpine Picoline® inside a glove box in protective argon atmosphere was used to prepare the powder. The particle size distribution was limited to the range of 20 to 80 μm by sieving, which is the represents the relevant region for Laser Powder Bed Fusion.

3.3. Additive Manufacturing and Qualification Process

The powders for the material under investigation are consolidated by Laser Powder Bed Fusion. A commercially available PBF-LB system EOSINT M270xt from EOS GmbH was used to conduct the experiments. This system uses a 200-W single-mode fibre laser with a wavelength of 1064 nm focused to a spot size of 83 μm. The building volume has a size of 250 mm x 25 mm x 215 mm. The process from powder to a printed volume contained three steps. At first, 1D melt tracks on a bulk piece of the material and 2D layer tests are performed to obtain qualitative information about the melting behaviour of the material. For the 2D tests, the powder was applied by hand in order to reduce the necessary powder volume. The systematic variation of the processing parameters was qualified by light microscopy. Consistent melt tracks and complete layers were positive indicators. For the subsequent 3D volume tests, the layer thickness had to be adapted to the powder flowability and size. Due to irregular shaped particles the layer thickness was changed for each experiment respectively. The powder was applied by an automated blade and the distribution of the powder was visually inspected. Starting from thin layers, the thickness was increased until a homogeneous distribution was achieved. Finally, multiple layers were built on a Nd-Fe-B based substrate fixed on a steel building platform. The size and geometry of the samples can differ, but a systematic variation of the volume energy was tested for all samples. The subsequent characterization included light and electron microscopy and the measurement of magnetic properties.

3.4. Characterization Methods

3.4.1. Scanning Electron Microscopy

The characterization of the microstructure contains morphology of grains, compositional gradients and identification of phases and phase fractions which is all united in Scanning Electron Microscopy (SEM). A *VEGA3* microscope from *TESCAN* equipped with a tungsten cathode (0.2 to 30 kV) electron source was used for first investigations.

For the Nd-Fe-B system, the morphology of the grain structure and characterization of phases can be best imaged by Backscattered Electrons (BSE). The incident electrons are reflected depending on the Z-number (electron number) of the atoms. This allows to distinguish different phases based on a pronounced grey-scale contrast in the micrograph. Further elemental quantification was done by using Energy Dispersive X-ray Spectroscopy (EDS or EDX). The element specific characteristic x-rays are excited by the incident electron beam and allow for an element specific quantification. Electrons from lower atomic energies are expelled and replaced by electrons from higher energy states. This element specific energy difference is emitted as an x-ray photon and can be used to quantify the element concentration. The emitted photons create electron-hole pairs in a semiconductor detector which give rise to a current proportional to the photon energy. The signal is amplified and processed which leads to the EDX spectrum in form as the intensity (summation of photons) over the corresponding energy. The interaction of electrons with matter does not easily allow to quantify the element concentration as described above. The absorption of elements needs to be corrected which depends on the chemical composition of the sample. However, the absorption coefficients can be determined by measurement and/or calculation. In addition, the fluorescence of photons with lower energy are considered as well. Based on referencing database resulting in a ZAF

correction. The TEAM™ EDS Analysis System for SEM by EDAX Corporation consisting of the TEAM™ EDS software and the Octane Silicon Drift Detector was used for this purpose.

3.4.2. Transmission Electron Microscopy

The magnification limit of light and scanning electron microscopes is not sufficient to resolve microstructural features on nanometer scale. Therefore, high resolution Transmission Electron Microscopy (TEM) is used. The wavelength of an electron following the de Broglie description can reach resolution in atomic scale. However, high acceleration voltages up to several hundred kV are used to penetrate the sample much deeper. Thin samples of several hundred nanometers are exposed to a high voltage electron beam. Like in SEM, it is possible to image the microstructure and measure the composition and obtain information on the crystal structure based on electron diffraction reaching magnifications of a few nanometers.

In this work, TEM microscopy was performed on an aberration corrected Titan 80−300 microscope (FEI Company) at the Karlsruhe Nano Micro Facility (KNMFi) performed by Dr. Andrey Mazilkin, who also prepared the data and was involved in the discussion and evaluation of the results. The specimens for this TEM study were prepared by ion milling on an FEI Strata 400S dual beam facility. The experiments were necessary to prove the occurrence of nano-scale precipitates and determine their crystal structure and composition.

Additional nanoscale characterizations of the metastable phase were done using a 200 kV JEOL JEM 2100-F Transmission Electron Microscope (TEM) at the Advanced Electron Microscopy Division of the Materials Science department at TU Darmstadt. The TEM lamella was prepared by cutting a slice of approximately 10 mm thickness of a bulk sample. The slice was then polished down to 50 μm thickness. Subsequent thinning down to an electron transparent lamella was achieved by ion milling two-step process using a Gatan 691 Precision Ion Polishing System (PIPS). First the angles and ion beam energy were set to 8 and 5.5 eV, respectively, and milling was done until a small hole was observed in the sample center. Then, the second step of milling with angles of 2 ° and ion beam energy of 2 eV was done to remove the damages from the previous step of milling. The structural features were investigated using bright-field and high-resolution TEM imaging, and diffraction patterns. The sample preparation, investigation and data treatment were done by Dr. Esmaeil Adabifiroozjaei, who was also involved in the discussion and evaluation of the results.

3.4.3. Phase Identification via Powder X-Ray Diffraction

Due to compositional and structural similarities of RE-based intermetallic phases and compounds and small feature in the microstructure, SEM-EDX characterization is often not sufficient and powder x-ray diffraction is used to distinguish phases based on their crystal structure. In general, diffraction does occur when electromagnetic radiation is interacting with periodic structures on same wavelength scales. For the structural characterization of materials, the elastic scattering of x-ray photons (Thomson Scattering) on the electrons of the crystal are used. The electrons act like a Hertz dipole and lead to interference. The detected intensities in form of a diffraction pattern can be translated to the crystal structure of the phases in the microstructure. Constructive interference occurs if the Bragg condition is fulfilled, with n being the order of diffraction, λ the wavelength of the x-ray radiation, d the lattice constant and θ the glancing angle:

$$n\lambda = 2dsin\theta$$

Equation 16: Bragg Condition

The characterization was performed on powder samples using a Stoe Stadi P diffractometer with $Mo\,K_{\alpha 1}$ radiation in transmission mode. The qualitative and quantitative phase characterization was done by using FullProf/WinPLOTR suite software.

3.4.4. Magnetic Characterization

Vibrating Sample Magnetometer

The measurement of the magnetic hysteresis is based on Faradays law of induction.

$$U_{ind} = -\frac{d\phi}{dt}$$

Equation 17: Faradays Law of Induction.

The principle relies on the change in magnetic flux over time. The Vibrating Sample Magnetometer (VSM) is based on the movement of the sample with certain frequency. Therefore, it is commonly mounted on a stick and driven by an electric motor, positioned in a calibrated set-up regarding the applied field and pick-up coils. The induced voltage is proportional to the magnetic moment of the sample. The static magnetic field is either applied by an electromagnet or by a superconducting magnet where the latter reaches fields up to 14 T. In this work, the hysteresis of the samples was measured inside a Quantum Design Physical Properties Measurement System PPMS-14 with VSM option at room temperature in a maximum field of 3 T. The temperature dependence of the magnetic moment was characterized by thermomagnetic measurements which were carried out using a LakeShore 7410 VSM equipped with an oven option. The magnetization was measured during heating and cooling between 350 K to 1200 K with a heating rate of 5 K/min and a constant applied field of 0.05 T. Before and after the thermomagnetic measurement, a magnetic hysteresis was recorded in a field of 2 T at room temperature to check the quality of the sample before and after thermomagnetic measurements. Degradation of the sample was inhibited by covering the sample with a ceramic layer and a constant stream of Argon gas.

3.4.5. Kerr Microscopy

The magneto-optic Kerr effect (MOKE) is used to visualize magnetic domains. It relies on the rotation of light polarization by interaction with the magnetic moments of the sample. In case of materials with magnetic ordering, the incident linear polarized light causes oscillations of the electrons which lead to a Lorentz force and a rotation of the polarization depending on the magnetization vector. Kerr microscopes are equipped with a tuneable polarizer and analyzer which enable the contrast between the incident light beam and the polarization of the reflected light. The strongest influence has the out of plane component of the magnetization on the surface, which leads to the polar Kerr effect.

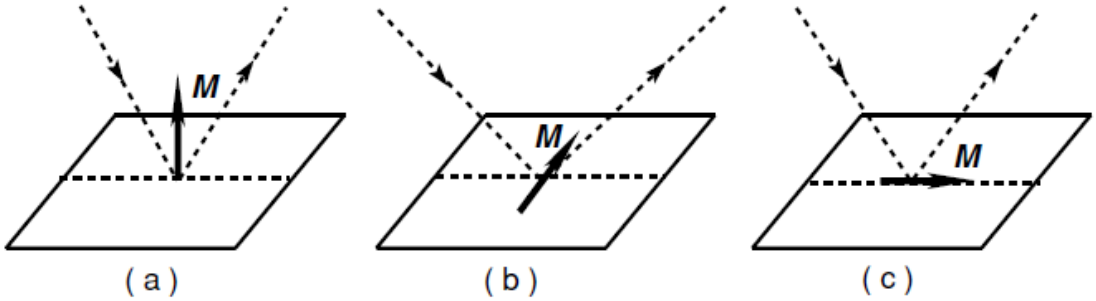

Figure 23: Configuration of Kerr effects. Polar (a), transverse (b), longitudinal (c). [79]

The magnetic domain contrast was observed by utilizing the magneto-optical Kerr effect (MOKE) in a light microscope (Zeiss Axio Imager.D2m evico magnetics GmbH). The image contrast was enhanced digitally by subtracting the non-magnetic background image from the collected average image using the KerrLab software.

4. Nano-Composite Nd-Fe-B based Magnets by Phase Decomposition

Parts of the results shown in this chapter 4 have already been reviewed and published. [146]

4.1. Rapid Solidification of Nd-Fe-B based Alloys and the Effect of Elemental Modification

The production of Nd-Fe-B magnets is based on controlled production and annealing treatments with optimized composition for the respective route. The resulting microstructures are based on the hard magnetic $Nd_2Fe_{14}B$ phase. In both, sintered and hot-deformed Nd-Fe-B-based magnets, the $Nd_2Fe_{14}B$ grains are separated by a several nanometers thick Nd-rich grain boundary layer, which reduces surface defects of the grains, prevents the nucleation of reverse magnetic domains and finally leads to high coercivity. However, this desired microstructure is not easily realized in the bulk as-cast state or novel production techniques such as Laser Powder Bed Fusion (PBF-LB). Local melting and complex solidification of the Nd-Fe-B-based powder precursor is a substantial problem that is being tried to be solved. A possible way to overcome this problem is the formation of a metastable phase which can be transformed by subsequent annealing treatment and passes through a phase decomposition reaction. In this way, the microstructure can be refined, and even the formation of nano-composite structures are possible. The resulting magnetic properties can be fundamentally different from the nucleation type coercivity mechanism in sintered Nd-Fe-B. More specifically, the nano-phase decomposition could lead to pinning and even lead to a remanence enhancing effect depending on the magnetic properties of the occurring phases. However, commercial Nd-Fe-B magnets and microstructures after intermediate production steps do not show the formation and occurrence of a suitable phase. It is necessary to investigate alloy compositions with specific element substitution.

Previous literature has shown that it possible to form a metastable $Nd_2Fe_{17}B_x$ phase (referred to as χ-phase) by solidification experiments using electromagnetic levitation or drop tube technique. The important factor seems to be the large undercooling by homogeneous nucleation of crystallites from the melt. The closest practical realization is quenching small samples (<5 g) in water. Other techniques with high cooling rates, such as suction casting or melt spinning, are based on fast thermal transport through the die (usually water cooled Cu) and by forming a large sample surface. Such techniques are used for the production of ribbons for hot compacted and deformed magnets. However, high cooling rates result in amorphous microstructures and not to the formation of the χ-phase. Regarding the chemical composition it is known that Cobalt stabilizes the χ-phase. Preliminary results in the group of Functional Materials on the solidification behaviour of Nd-Fe-Co-B samples have shown, that Fe substitution by at least 20 % of Co does result in a large fraction of the $Nd_2(Fe,Co)_{17}B_x$ phase. Subsequent annealing treatments could transform the microstructure and form the hard magnetic $Nd_2(Fe,Co)_{14}B$ phase, but the coercivity could not be increased. Therefore, the addition of Cu to the system seems to be necessary. This element is known to improve the wettability and separation of the hard magnetic grains, therefore increases coercivity. Furthermore, some transition metals are known to form precipitates in Nd-Fe-B magnets. These are referred to as “type-II” elements [91] and show low solubility in the hard magnetic $Nd_2Fe_{14}B$.

Based on this conclusion and preliminary results, the alloy composition for the following experiment was set to be $Nd_{16}Fe_{53}Co_{20}Cu_2TM_2B_7$. TM refers to different transition metals whose influence on the solidification behavior is investigated, namely Mo, Nb, Ti, V, Zr, W and Ta. The

samples have been prepared by induction melting and small pieces have been sealed in quartz under protective Argon atmosphere. They were annealed at 1300 °C for 10 minutes and subsequently quenched in water. The following SEM-BSE images show the microstructure of the quenched samples on the left and the corresponding annealed state at higher magnification.

The SEM-BSE images in Figure 24, Figure 25 and Figure 26 reveal that in the quenched state of the $Nd_{16}Fe_{53}Co_{20}Cu_2TM_2B_7$ samples, only the samples with TM = Mo, Nb show the formation of a metastable phase which is observed as dendritic, dark grains. At this stage, EDX reveals a slightly lower RE content compared to a $Nd_2Fe_{14}B$ stoichiometry. Furthermore, traces of Mo and Nb respectively are found within these dendrites, which indicates that it is not the $Nd_2Fe_{14}B$ phase since the solubility for these elements is very low and not detectable by EDX. An obvious difference between the samples is the smaller grain size of the Mo containing sample. Furthermore, no precipitates in the quenched state are found. Systematic investigation of the $Nd_{16}Fe_{53}Co_{20}Cu_2Mo_2B_7$ and XRD reveals that besides the metastable $Nd_2(Fe,Co)_{17}B_x$ formation, $Nd(Fe,Co)_4B$ phase is occurring after quenching which is forming a thick matrix and is observed as in brighter SEM-BSE contrast. The annealing treatment shows the formation of $Nd_2Fe_{14}B$ and spherical precipitates down to sizes in nanometer region. By TEM, the precipitates could be determined as $FeMo_2B_2$ phase. The Nb addition leads to precipitates in similar shape, size and stoichiometry based on the SEM-BSE contrast.

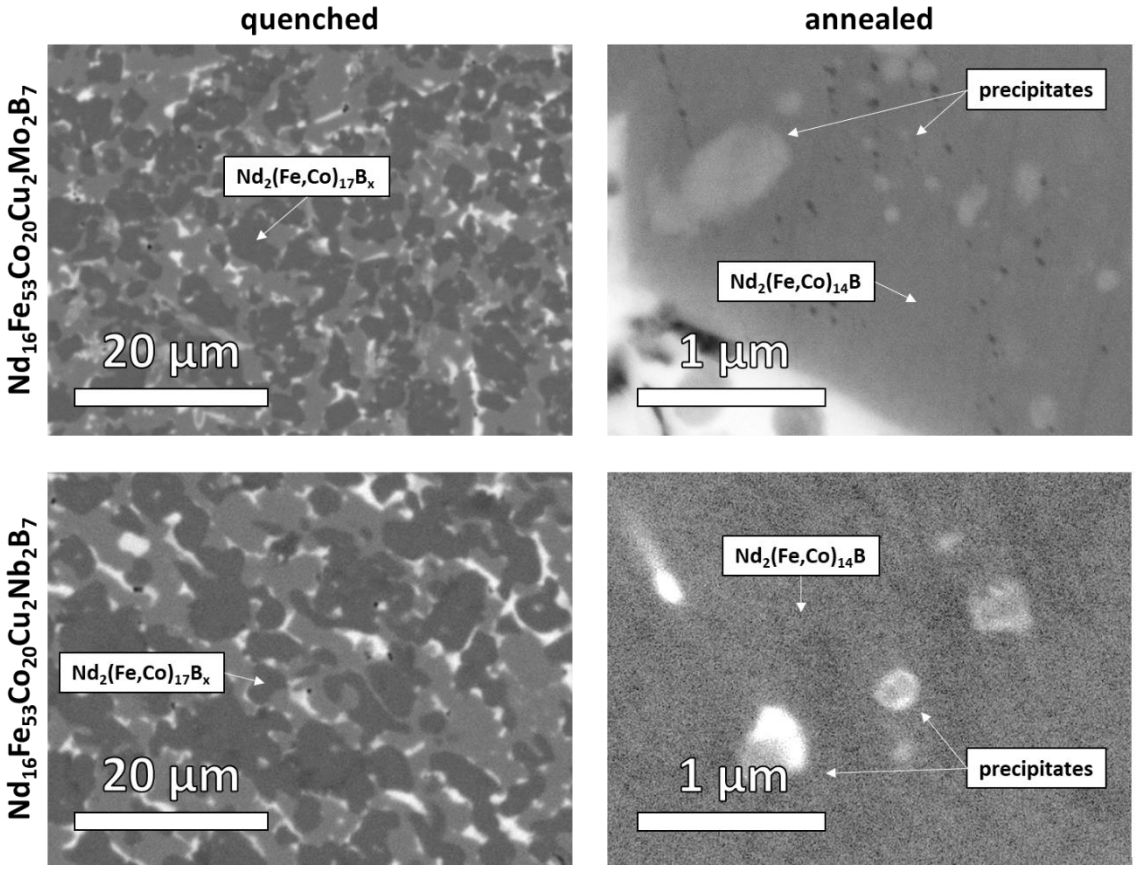

Figure 24: SEM-BSE images of the quenched (left) and annealed (right) microstructure for the $Nd_{16}Fe_{53}Co_{20}Cu_2\mathbf{TM}_2B_7$ composition with **Mo** and **Nb**. For both samples, main solidification product of the metastable phase are found. After annealing, both samples show nano-sized Mo, Nb rich precipitates.

Nanometer sized dark spots are visible in BSE contrast in the Mo containing sample (Figure 24b). However, there is no indication for the formation of α-Fe phase and there is no visible

difference in size. This indicates that it has to be an artifact from the sample preparation, most likely a corrosion effect during polishing. Further substitution by the elements Ti, V and Zr (Figure 25) reveal the formation of precipitates already in quenched state, which differs from the Mo and Nb containing samples. At the same time, there is no indication for the occurrence of metastable phase besides some small fractions in the Zr containing sample. In all samples, macroscopic precipitates seem to accumulate in the grain boundary which leads to rather fine microstructures below 20 μm. However, after the annealing treatment, smaller precipitates down to several hundred nanometers can be observed. The shape of such precipitates differs for the respective elements.

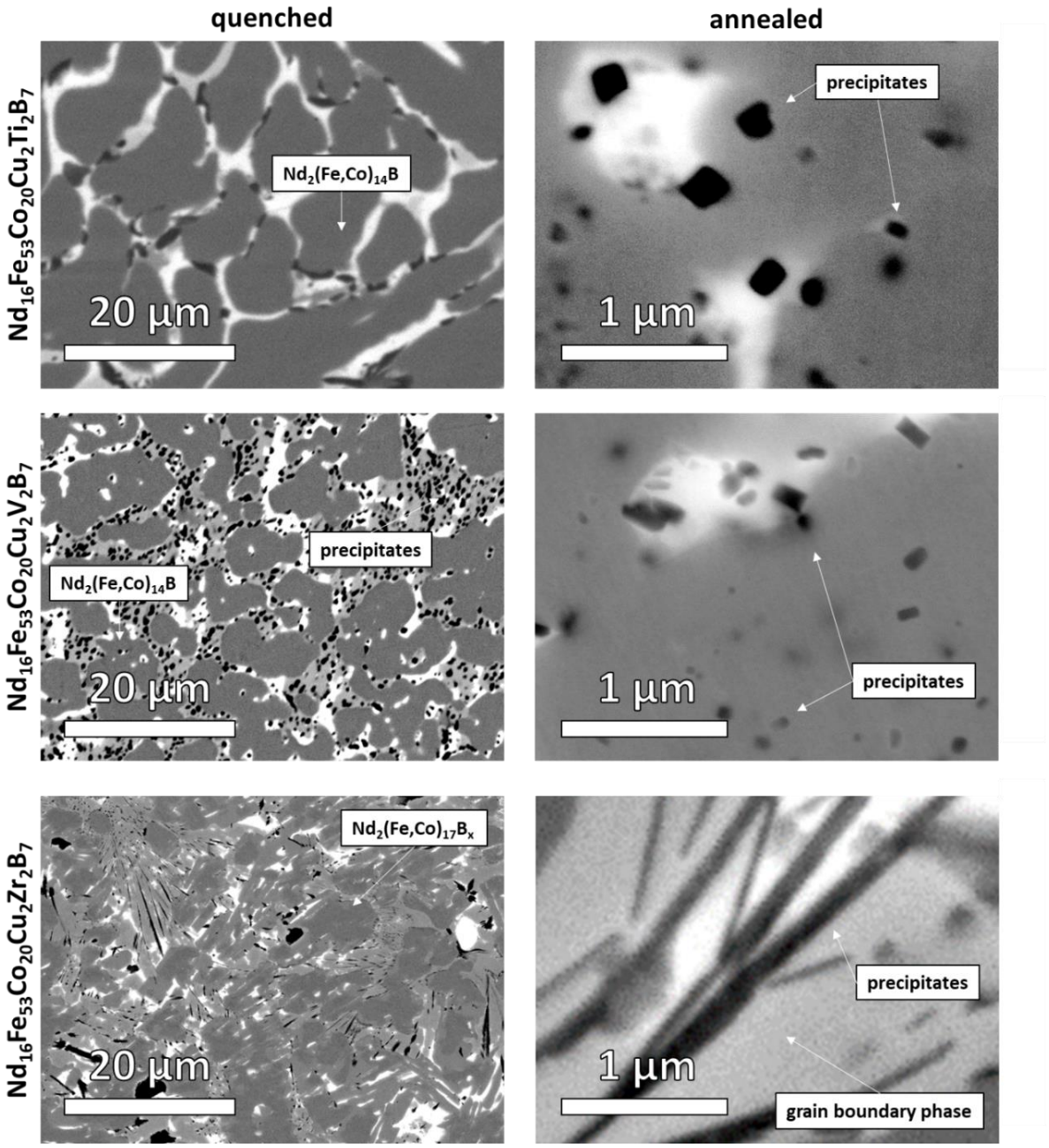

Figure 25: SEM-BSE images of the quenched (left) and annealed (right) microstructure for the $Nd_{16}Fe_{53}Co_{20}Cu_2$**TM**$_2B_7$ composition with **Ti, V** and **Zr**. For all samples, the microstructure shows the occurrence of boride phases in dark contrast in quenched and annealed state. Whereas the hard magnetic $Nd_2Fe_{14}B$ is the primary solidification product in the Ti and V sample (grey contrast), the Zr sample shows the occurrence of metastable $Nd_2Fe_{17}B_x$ phase in form of dendritic grains embedded in the $Nd_2Fe_{14}B$ phase after quenching.

Whereas Ti and V show rectangular, almost cubic shape (Figure 25 b,d), the Zr containing sample shows needle-like shape of the precipitates (Figure 25 f). Although the true quantification of composition and crystal structure of the precipitates cannot be determined by SEM only, the dark contrast, no Nd and (Fe,Co) intensity and high B intensity in EDX indicate that these precipitates have to be binary borides such as TiB_2, VB, V_2B_3 and ZrB_2.

Addition of Ta and W reveal a very different microstructure in quenched state. In these samples, the primary solidification product is α-Fe which is visible as dendritic grains in dark BSE contrast (Figure 26 a, c). Besides that, $Nd(Fe,Co)_4B$ grains are observed and intergranular $Nd(Fe,Co)_2$ and Nd-rich phase. The high melting refractory metals form metallic precipitates both in the quenched and annealed state. Besides large accumulations, very fine precipitates are observed after the annealing treatment within the $Nd_2(Fe.Co)_{14}B$ grains and within the grain boundaries.

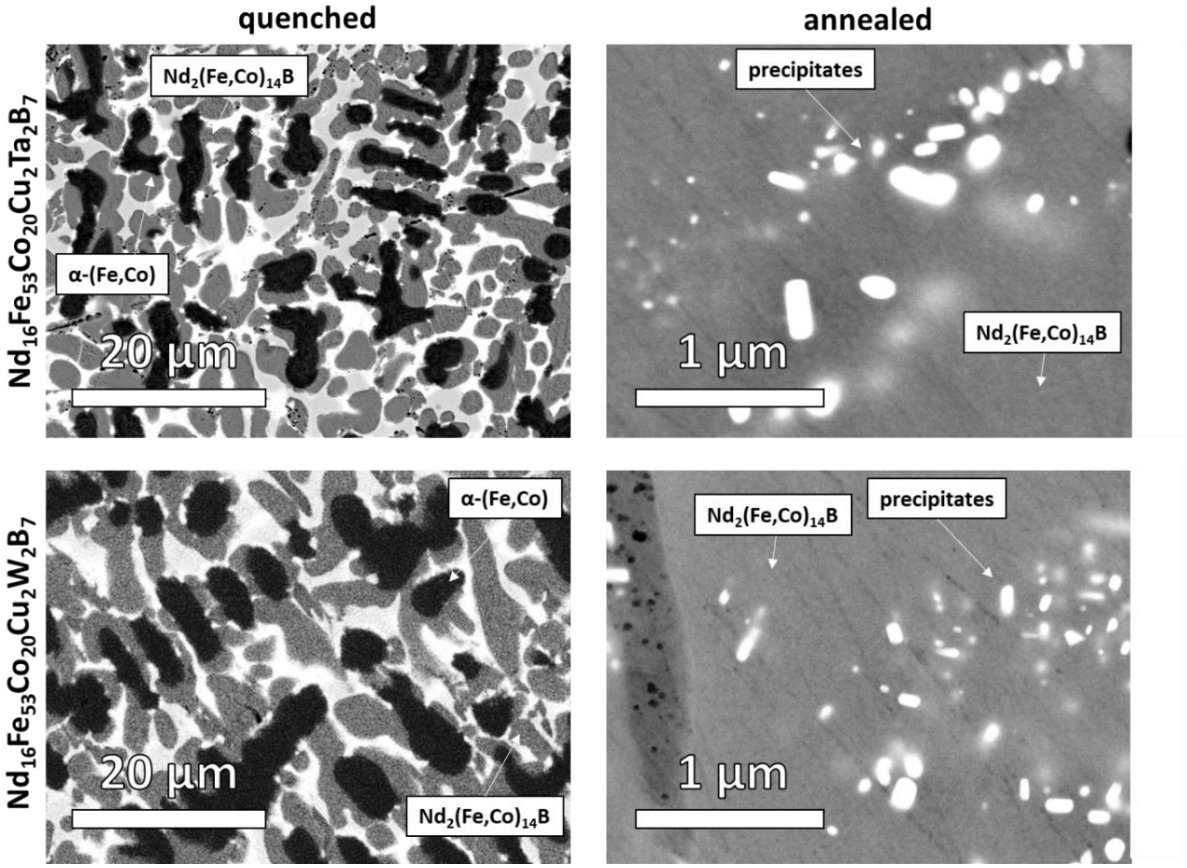

Figure 26: SEM-BSE images of the quenched (left) and annealed (right) microstructure for the $Nd_{16}Fe_{53}Co_{20}Cu_2\mathbf{TM}_2B_7$ composition with **Ta** and **W**. The primary solidification product is α-Fe after quenching. Both samples show the formation of metallic precipitates of the corresponding refractory metals.

In summary, three different groups of precipitates could be determined in $Nd_{16}Fe_{53}Co_{20}Cu_2TM_2B_7$. First, Mo and Nb are forming globular $Fe(Nb,Mo)_2B_2$ precipitates which are only present in the annealed samples. Elements Ti, V and Zr are forming binary boride phases in rectangular/ cubic or needle like shape which are visible both in the quenched and annealed state. The metals Ta and W are forming metallic inclusions which are present in quenched and annealed state indicating very low solubility and insufficient temperature to melt these metals completely due to their high melting points.

The most important observation is, that only Nb and Mo show large amount of the metastable $Nd_2(Fe,Co)_{17}B_x$ phase after the quenching experiment. At the same time, the precipitates are only present in the annealed state, indicating that the metastable phase has a high solubility of Mo and Nb and passes a decomposition reaction during the heat treatment. These observations indicate that the elements Mo and Nb can increase the stability of the $Nd_2(Fe,Co)_{17}B_x$ and are important to realize high fraction of the metastable phase. Furthermore, it is known that a large undercooling of the melt is necessary to form the metastable phase. The very stable binary boride phases such as TiB_2 and ZrB_2 can act as nucleation sites for the crystallization of the melt during the quenching. Although the grain size is reduced by this effect, the formation of the metastable phase can be suppressed and the competing phases α-(Fe,Co) and $Nd_2Fe_{14}B$ will occur as primary solidification products.

Besides the effect on the stabilization of the metastable phase, the element additions have a severe impact on the magnetic properties (Figure 27). After the annealing treatment, the highest coercivity is reached for the alloy with Nb and Mo addition with $\mu_0 H_C = 0.75$ T and $\mu_0 H_C = 0.85$ T respectively. This coincides with the formation of the metastable phase and the decomposition leading to $Nd_2Fe_{14}B$ and $Fe(Nb,Mo)_2B_2$. The high magnetization for the samples containing Ta and W can be explained by the high fraction of α-Fe. At the same time, this also explains the low coercivity in these samples.

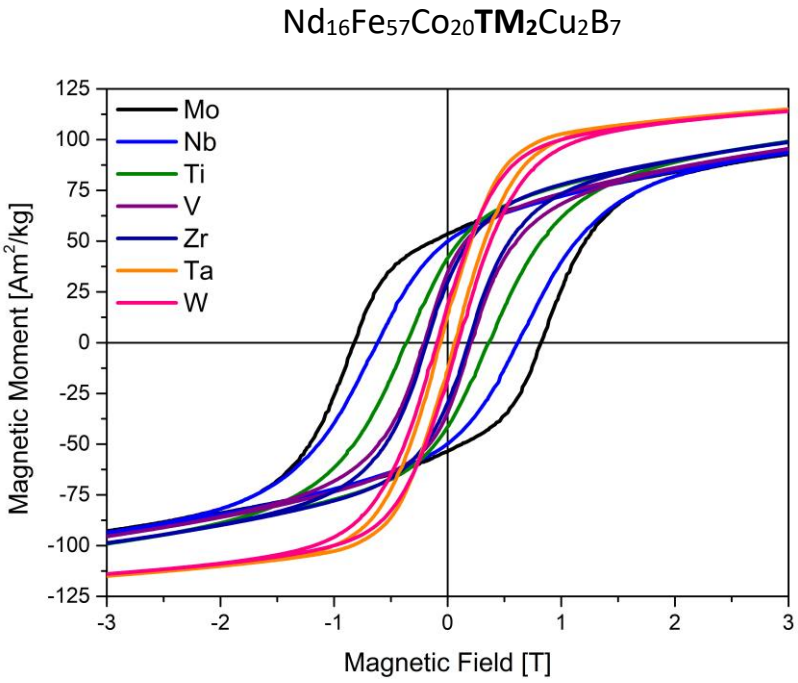

Figure 27: Magnetic hysteresis at room temperature for the systematic substitution of $Nd_{16}Fe_{57}Co_{20}\mathbf{TM_2}Cu_2B_7$ by Mo (black), Nb (blue), Ti (green), V (purple), Zr (dark blue), Ta (orange) and W (pink). The highest coercivity is found for the Mo and Nb samples which both show similar microstructures with metastable $Nd_2Fe_{17}B_x$ phase after quenching and Mo- and Nb-Fe-B precipitates after annealing.

So far, the reason for the magnetic hardening mechanism is not clear and only the effect of the transition metal addition in a multi-component $Nd_{16}Fe_{53}Co_{20}Cu_2TM_2B_7$ alloy are observed. In this regard, more systematic investigation on the $Nd_{16}Fe_{53}Co_{20}Cu_2Mo_2B_7$ alloy composition and the effect of each element on the phase stability and magnetic hardening effect is shown in the following chapters. Furthermore, the role of the annealing treatment and the magnetic hardening effect will be discussed.

4.2. Investigation of Magnetic Hardening in $Nd_{16}Fe_{77-x-y-z}Co_xCu_yMo_zB_7$ (x = 20, y =2, z = 2)

The following chapter contains data and figures which have been published in [146].

To investigate further the phase stability and magnetic properties by utilizing the formation of metastable phase in Nd-Fe-B, a starting ternary composition was chosen with a stoichiometry of $Nd_{16}Fe_{77}B_7$. The systematic modification was done by remaining the Nd to B ratio. All element substitutions have been done by replacing the Fe content. Since it is known that Cu and Mo act mostly on the grain boundary phase and/or are forming secondary phases and precipitates, two distinct alloy systems can be distinguished, the Nd-Fe-B and quaternary Nd-Fe-Co-B batches with respective substitution by Mo and Cu.

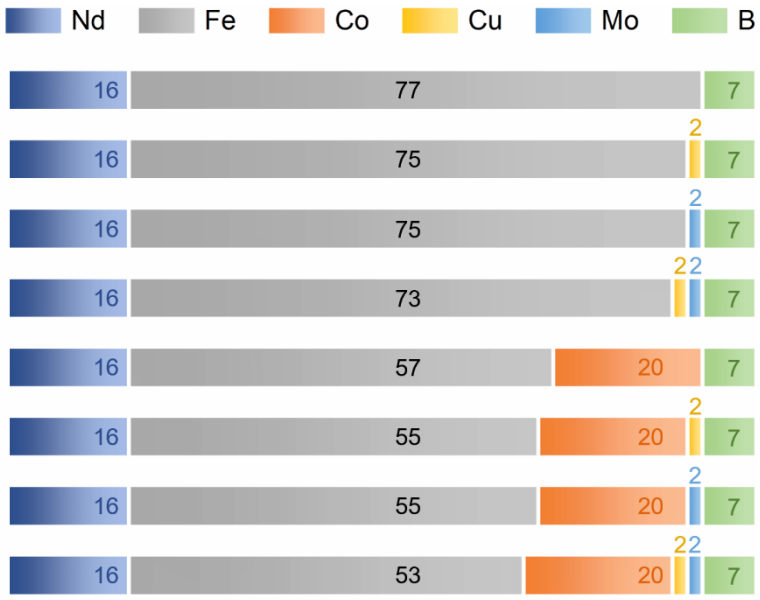

Figure 28: Systematic alloy modification of the Nd-Fe-B and Nd-Fe-Co-B master alloys. The samples were prepared to analyze the effect of the additional elements on the formation of the metastable phase and the coercivity. The substitutions were done by replacing the Fe fraction. The Nd to B ratio was kept constant.

The experimental set-up was kept the same as before. Small samples of < 3 mm were remolten in a tube furnace at 1300 °C and quenched in water after 5 minutes in the furnace. The microstructures in SEM-BSE contrast are shown in the left images of the corresponding quenched samples in Figure 29. The annealing process was similar to that is used for production of sintered permanent magnets: high temperature annealing at 1075 °C for 30 minutes, followed by cooling with 300 K/min to 500 °C, dwelling for 1 hour and furnace cooling to room temperature. The treatment has been investigated in prior experiments. The microstructure after the annealing are shown in the right part of the corresponding samples in Figure 29.

For the ternary Nd-Fe-B alloy (Figure 29a), dendritic α-Fe appears in dark BSE contrast, the matrix $Nd_2Fe_{14}B$ phase is grey, the bright contrast corresponds to the Nd-rich grain boundary phase. Compared to this sample, the additions of Cu (Figure 29(c)) and both Cu and Mo (Figure 29 (g)) leads to a grain refinement, but α-Fe remains the primary solidification product. An exception in this series is the $Nd_{16}Fe_{75}Mo_2B_7$ sample (Figure 29 (e)) which shows the metastable $Nd_2Fe_{17}B_x$ phase in dark grey contrast as the primary solidification product instead of α-Fe.

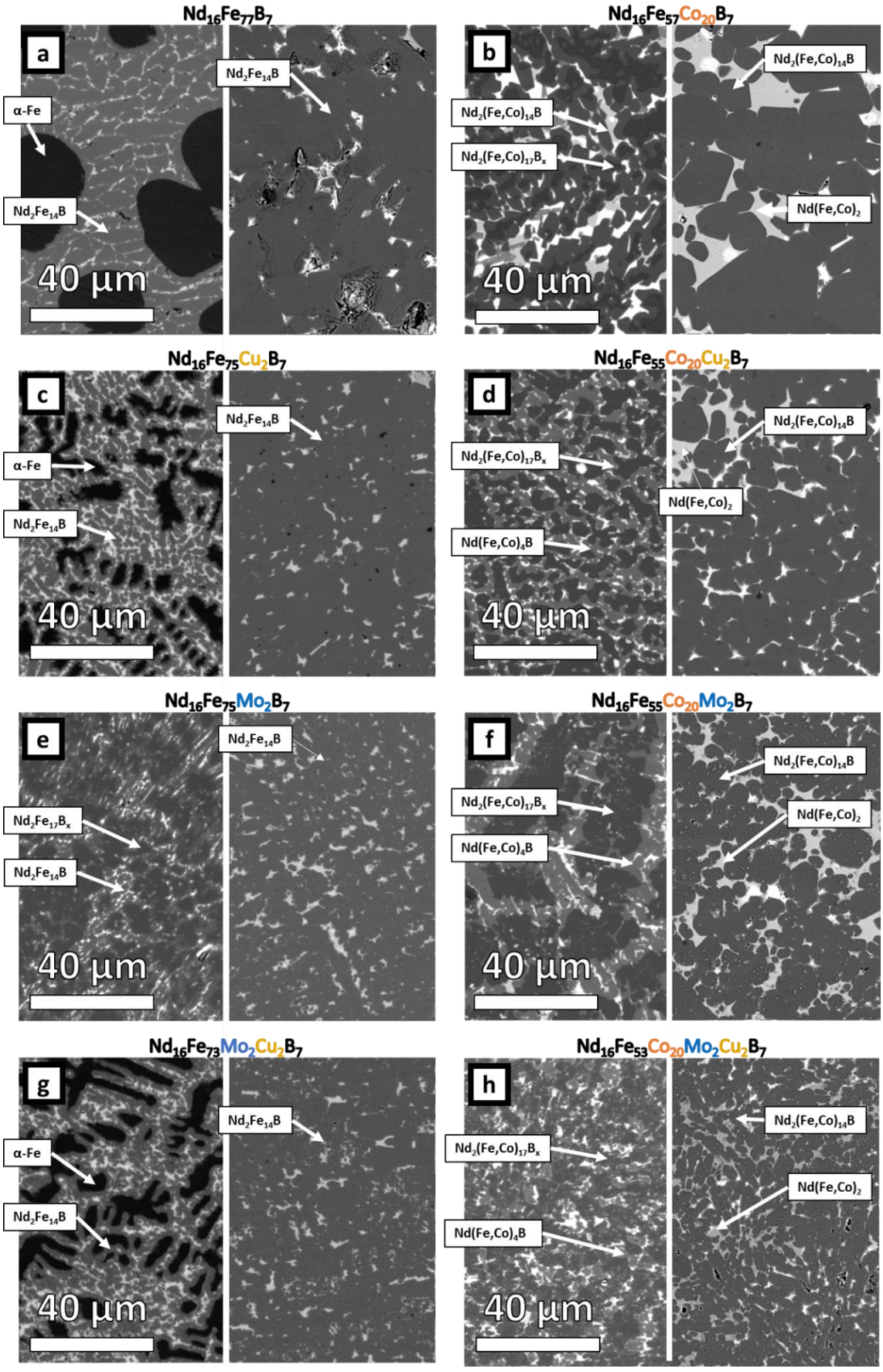

Figure 29: SEM-BSE micrograph after quenching (left part of the image) and annealing (right part of the image). The Nd-Fe-B sample series is shown on the left side (a,c,e,g). The series with Co addition is shown on the right (b,d,f,h).

The right part of the images (Figure 29a, c, e, g) shows the microstructure of these samples after annealing. All samples consist of hard magnetic $Nd_2Fe_{14}B$ grains and a Nd-rich phase, whereas both metastable $Nd_2Fe_{17}B_x$ and α-Fe phases are fully transformed by heat treatment. The addition of Cu and Mo leads to grain refining effect after the heat treatment. However, the samples show a non-continuous grain boundary matrix phase. This indicates that the microstructure is not ideal to obtain high coercivity. The point of contact between hard magnetic grains of different orientation are critical spots for domain nucleation during demagnetization and are tried to be avoided during permanent magnet production.

The addition of Co changes drastically the solidification behavior of the samples. The quenched sample (Figure 29b) shows a core-shell-like structure of the grains. In the center of the grains the dark $Nd_2(Fe,Co)_{17}B_x$ phase was found which is surrounded by a layer of the $Nd_2(Fe,Co)_{14}B$ phase. Introducing both Co and Cu (Figure 29d) leads to a refinement, whereas the addition of Co and Mo (Figure 29f) leads to a coarsening of the microstructure. Addition of Co, Cu and Mo (Figure 29h) leads to a very fine microstructure consisting of $Nd_2(Fe,Co)_{17}B_x$ grains surrounded by the $Nd(Fe,Co)_4B$ and Nd-rich phase in quenched state.

After the annealing, a bimodal size distribution with grains larger than 40 μm and smaller than 5 μm was found in the $Nd_{16}Fe_{57}Co_{20}B_7$ sample (Figure 29b). The grain boundary phases are Nd-rich phase (very bright contrast), and the $Nd(Fe,Co)_2$ Laves phase which is confirmed by XRD although the binary $NdFe_2$ phase does not exist at ambient conditions. Further addition of Cu, Mo and both Mo and Cu leads to a grain refining effect and in the $Nd_{16}Fe_{53}Co_{20}Cu_2Mo_2B_7$ sample (Figure 29 (h)) with $Nd_2(Fe,Co)_{14}B$ grain size below 10 μm. In addition, these grains are well separated by the (Nd,Cu)-rich and $Nd(Fe,Co)_2$ grain boundary phase resembling the microstructure of a sintered Nd-Fe-B magnet. The occurrence of additional phases such as $Nd(Fe,Co)_4B$ and $Nd(Fe,Co)_2$ does agree with the existing literature, especially on rapid solidified and annealed Nd-Fe-Co-B based material [96], [98], [147], [148]. The formation of such phases is related to the high Co content in these alloys.

X-ray diffraction analyses (XRD) has been performed for all as-quenched and annealed samples in order to identify the occurring phases in these alloys more precisely. The corresponding diffraction pattern and Rietveld fits are shown in the Figure 30 and Figure 31.

After annealing, the $Nd_2Fe_{14}B$ phase has the largest fraction for all samples, however the quenched state depends strongly on the composition. The strong influence of the dopants on the microstructure in quenched and annealed state is apparent when comparing the $Nd_{16}Fe_{77}B_7$ and $Nd_{16}Fe_{53}Co_{20}Cu_2Mo_2B_7$ samples which are shown in Figure 30 and Figure 31 a) and h) respectively. In the quenched state, the measured intensities for the ternary alloy can be fitted with the $Nd_2Fe_{14}B$, α-Fe and metallic Nd phases. In contrast, $Nd_{16}Fe_{53}Co_{20}Cu_2Mo_2B_7$ does show the formation of $Nd(Fe,Co)_2$, $Nd(Fe,Co)_4B$, $Nd_2(Fe,Co)_{14}B$ and $Nd_2(Fe,Co)_{17}B_x$ which leads to a complex diffraction pattern. It is important to mention that the metastable $Nd_2(Fe,Co)_{17}B_x$ phase could be assigned to the binary Nd_2Fe_{17} structure with rhombohedral $R-3m$ symmetry (space group 166) described by the phase prototype of Th_2Zn_{17}. By annealing, the transformation of the microstructure leads to the $Nd_2Fe_{14}B$ / $Nd_2(Fe,Co)_{14}B$ main phase in both quenched and annealed samples. The diffraction pattern are very similar for both samples after annealing, despite the formation of $Nd(Fe,Co)_2$ phase in the $Nd_{16}Fe_{53}Co_{20}Cu_2Mo_2B_7$ sample.

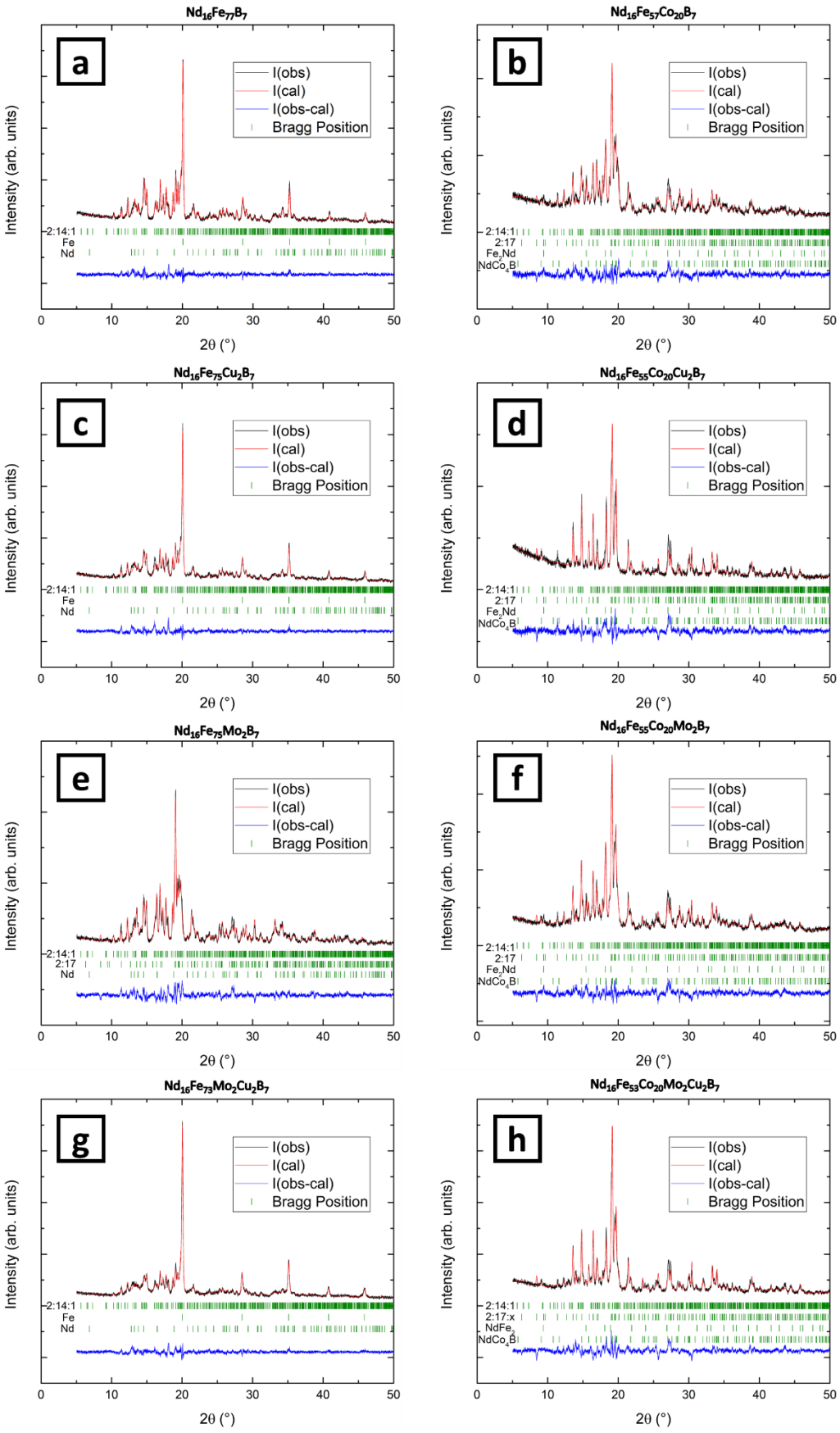

Figure 30: Powder XRD diffractograms of the quenched samples. The measured intensity in black is overlayed with the calculated intensity by Rietveld refinement. The difference is plotted in blue. The phases for the fit are chosen from the corresponding binary Nd-Fe or Nd-Co phases.

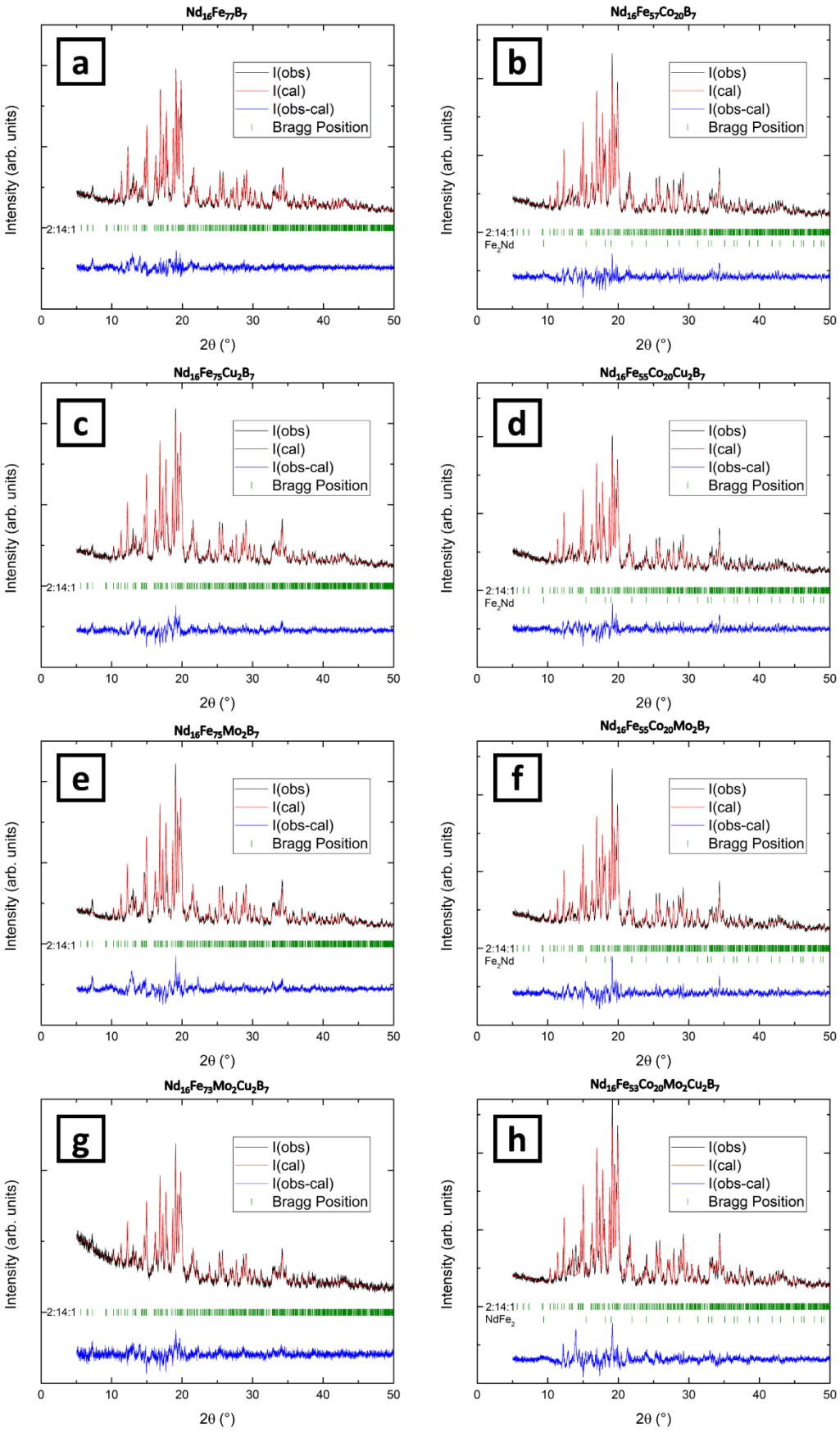

Figure 31: Powder XRD diffractograms of the annealed samples. The measured intensity in black is overlayed with the calculated intensity by Rietveld refinement. The difference is plotted in blue. The phases for the fit are chosen from the corresponding binary Nd-Fe or Nd-Co phases.

Based on the SEM-BSE characterization and XRD measurements on the corresponding samples, the phases could be identified and qualified. It has to be mentioned that a combinatorial analysis by XRD and image analysis has been needed since it is difficult to quantify the phase fractions of the finely distributed secondary phases. The corresponding phase fractions obtained by combination of EDX, XRD and image processing based on a Trainable Weka Segmentation [149] are shown in Figure 32. Especially the amount of grain boundary phase was very low, for some samples not existent, using XRD only. As it can be seen in the colored images in Figure 29, the machine learning based image analysis allows to separate and identify all phases by a pixel-based segmentation process. However, it is necessary to identify the phases in a prior step which makes XRD an inevitable characterization technique. Based on the segmentation, the phases are quantified via the area fraction of the SEM-BSE images.

It is important to mention, that the microstructure and occurring phases are much different from commercial Nd-Fe-B based magnets. Whether they are produced by sintering or hot deformation, the formation of secondary intermetallic phases is commonly considered to worsen the magnetic properties. First, they can increase the defect density at the hard magnetic grains and lead to a decrease in coercivity, especially if they are ferromagnetic (and soft magnetic). At the same time, they will lead to less formation of the $Nd_2(Fe,Co)_{14}B$ which will decrease the saturation magnetization of the sample and subsequently the remanence of the magnet. The quantification of the phases reveals that the secondary phases take up a large proportion of the microstructure. Further microstructural optimization including both improvement in alloy composition and annealing treatment are necessary to realize competitive magnetic properties compared to conventional Nd-Fe-B magnets.

However, in this work, a magnetic hardening effect which is based on the specific alloy modification and controlled heat treatment is observed, as shown in the magnetic hysteresis in Figure 33. For comparison, the two alloy series based on the Nd-Fe-B system in Figure 33a) and Nd-Fe-Co-B Figure 33b) are opposed. Apparently, the annealed samples without Co addition do not show coercivity higher than $\mu_0 H_C = 0.2$ T. The magnetization of the corresponding samples does not show large differences which agrees with the microstructural observations, indicating that the $Nd_2Fe_{14}B$ takes the largest fraction. The Nd-Fe-Co-B samples show a drastic improvement in coercivity by the annealing treatment. As soon as Cu and Mo are introduced to the system, the coercivity is doubling for the Cu containing sample (Figure 33b, green curve) and tripling for the Mo containing sample (Figure 33b, blue curve) compared to the ternary Nd-Fe-B sample. Highest coercivity of almost $\mu_0 H_C = 1$ T could be achieved by the simultaneous addition of Co, Cu and Mo. This striking value for bulk Nd-Fe-B based material without the use of advanced powder metallurgical processes is reached by the formation of metastable $Nd_2(Fe,Co)_{17}B_x$ and the subsequent microstructural transformation by heat treatment.

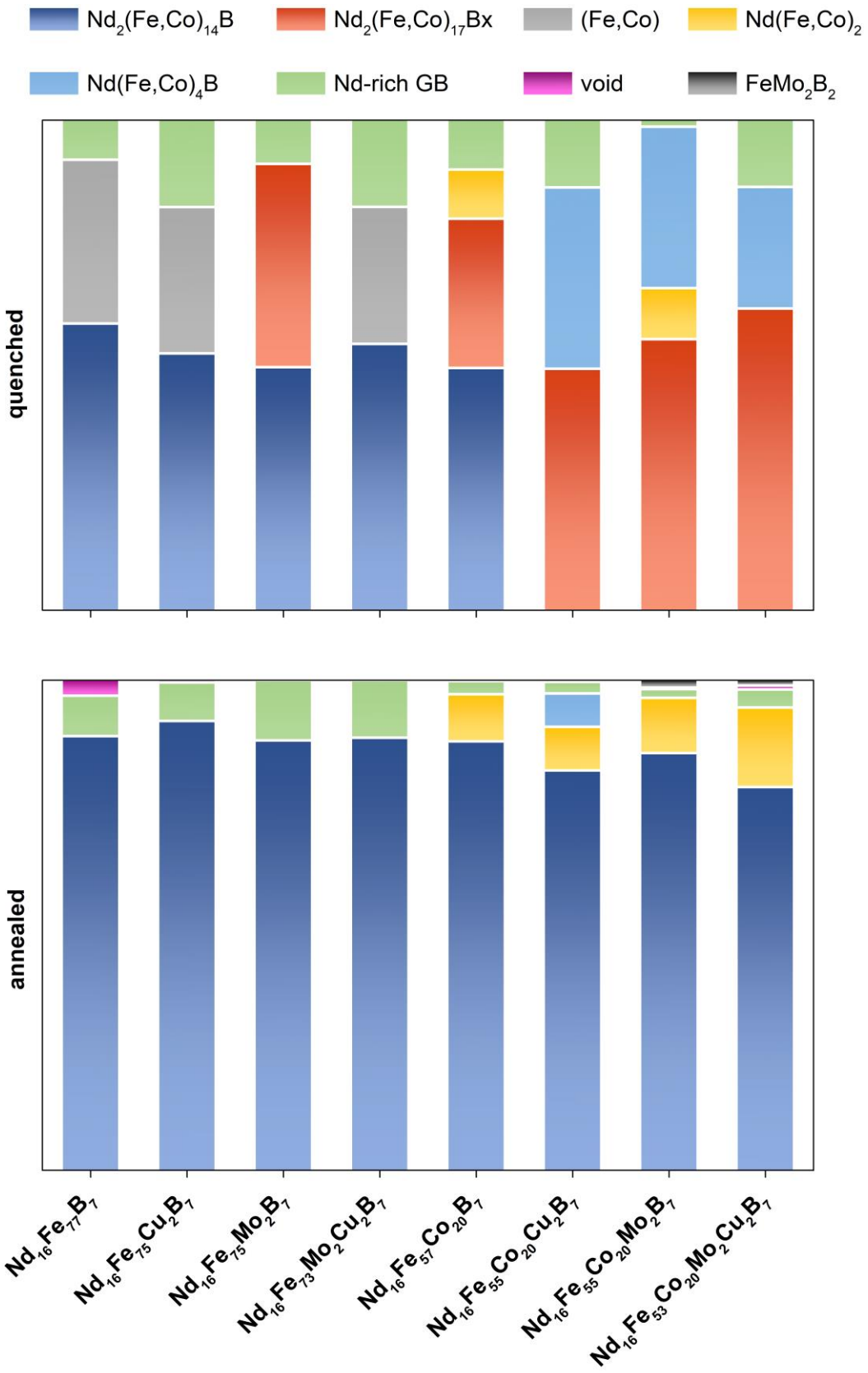

Figure 32: Phase fraction from image analysis and segmentation using ImageJ. The occurring phases are marked for the quenched (top) and annealed (bottom) sample. Besides the formation of the metastable $Nd_2(Fe,Co)_{17}B_x$ phase, the XRD and BSE characterization could show unusual secondary phases such as $Nd(Fe,Co)_2$ and $Nd(Fe,Co)_4B$. After the quenching, mostly metastable $Nd_2(Fe,Co)_{17}B_x$ and $Nd(Fe,Co)_4B$ are observed. After the annealing treatment the hard magnetic $Nd_2(Fe,Co)_{14}B$ and $Nd(Fe,Co)_2$ are present.

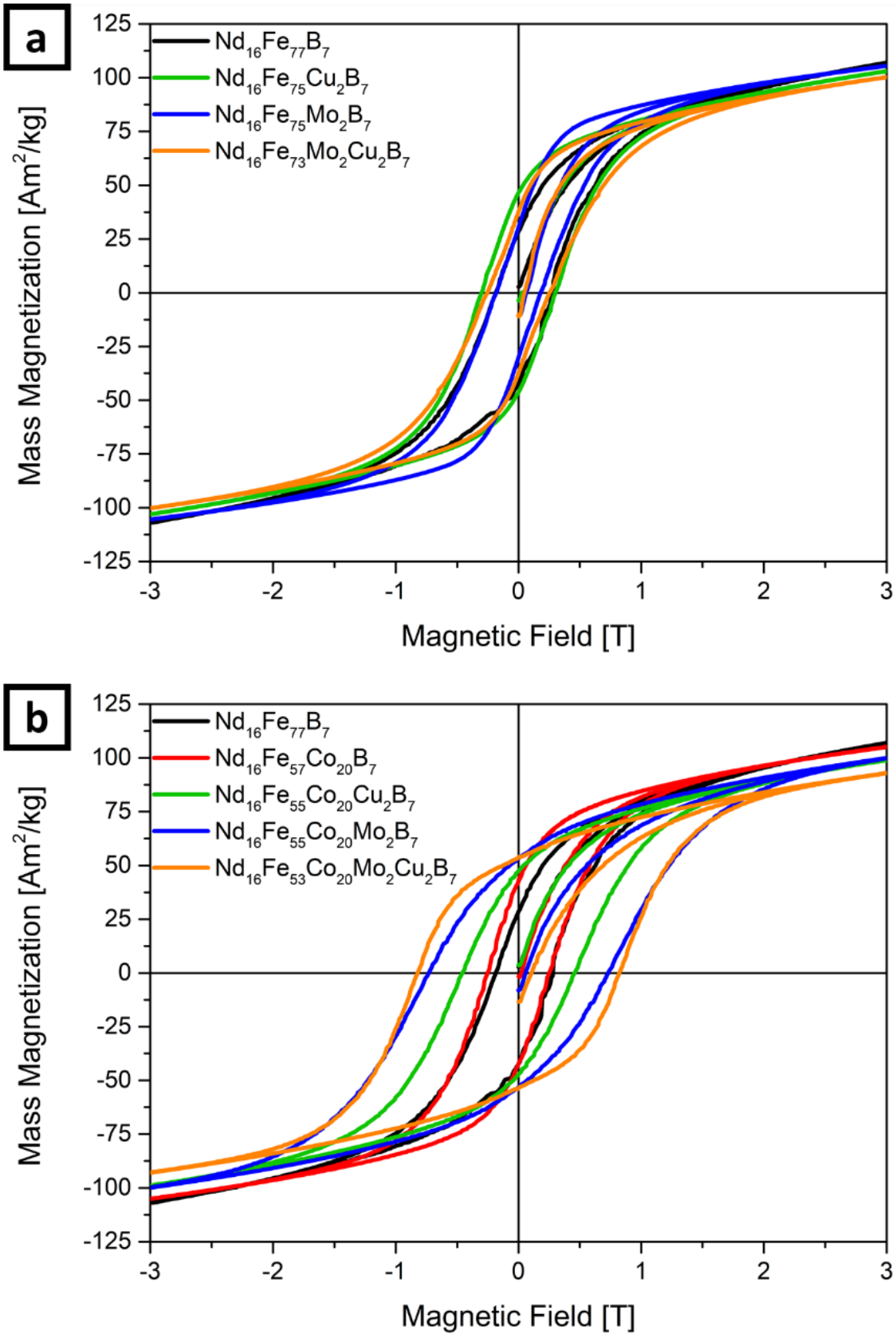

Figure 33: Magnetic measurements of the annealed samples without Co (top) and with Co addition (bottom). The hysteresis for the ternary Nd-Fe-B sample is shown in both plots to facilitate the comparison. The compositions without Co addition show a maximum coercivity around $\mu_0 H_C$ = 0.25 T. The elemental substitutions do not lead to a significant change of magnetic properties. Contrary to this, the addition of Cobalt drastically improves the coercivity of the samples. Addition of Co, Mo and Cu leads to the highest measured coercivity around $\mu_0 H_C$ = 0.8 T.

To comprehend the microstructural transformation during the heat treatment, thermomagnetic measurements were performed with the same quenched samples, which were used for the microstructural analysis. Both, the heating (Figure 34, red lines) and cooling (Figure 34, blue lines) curve between 350 K and 1200 K was recorded. The magnetization is given in arbitral units. The thermomagnetic measurements of the $Nd_{16}Fe_{77}B_7$ and $Nd_{16}Fe_{75}Cu_2B_7$ samples are in agreement with the results of the microstructural investigations. The α-Fe and the hard magnetic $Nd_2Fe_{14}B$ phase are reflected in the two Curie temperatures (T_C), which are indicated in in Figure 34a) and in Figure 34c). Both, the heating and cooling curves show a congruent $T_C \sim 585$ K for the $Nd_2Fe_{14}B$ phase and $T_C \sim 1030$ K for the alpha-Fe phase. As soon as Mo is alloyed, the metastable $Nd_2Fe_{17}B_x$ phase with a $T_C \sim 390$ K is formed and thus significant differences in the heating and cooling curves of the $Nd_{16}Fe_{75}Mo_2B_7$ and $Nd_{16}Fe_{73}Mo_2Cu_2B_7$ samples are observed. At this point, it should be noted that contrary to the SEM and XRD analysis, the sensitive magnetic measurements on the $Nd_{16}Fe_{73}Mo_2Cu_2B_7$ indicate the formation of the metastable phase.

In comparison to the Nd-Fe-B based alloys, the addition of Co has a significant effect on the phase formation and measured T_C, which can be seen by comparing the heating and cooling curves of the respective samples on the right graphs in Figure 34. As a reference of the respective sample, the cooling curve in blue shows only the T_C of the hard magnetic $Nd_2(Fe,Co)_{14}B$ phase and the α-(Fe,Co) phase. In contrast, the heating curve of the samples shows the transition temperature of the metastable phase at, compared to the $Nd_2(Fe,Co)_{14}B$ phase, lower temperatures. In the $Nd_{16}Fe_{57}Co_{20}B_7$ sample, the transition of the metastable phases is about $T_C \sim 710$ K (Figure 34b). The addition of the elements Cu and Mo leads to a shift of the transition towards lower temperatures (Figure 34d, f ,h)). Moreover, the temperature interval of the transition widens upon addition of the elements Cu and Mo, in contrast to the sharp T_C for the $Nd_2(Fe,Co)_{14}B$ phase. This may be due to the forcibly dissolved elements in the metastable phase by the high cooling rates, which may lead to inhomogeneities in composition.

In summary, the T_C of the respective phases is increased by the addition of Co, especially for the $Nd_2Fe_{14}B$ phase with $T_C \sim 585$ K to $T_C \sim 710$ K for the $Nd_2(Fe,Co)_{14}B$ phase. This effect has been known and the presented results agree with this trend. However, besides the indicated magnetic phases, the addition of Co, Mo and Cu elements does also lead to the formation of secondary phases which are seemingly paramagnetic and do not show high magnetization and a magnetic transition. This explains that some samples show a lower magnetization after the measurement despite the formation of α-(Fe,Co) as it can be seen in Figure 35 which shows the magnetic hysteresis of the samples before and after the measurement. An important observation, besides the magnetic transition temperatures, is that although the quasi-annealing treatment during the measurement does lead to a full transformation of the microstructure, the magnetic hysteresis before and after the measurements do not show a magnetic hardening effect as it can be seen in Figure 35. All samples show a soft magnetic behavior. The differences in magnetization can be explained by the different phase fractions depending on the element additions. Since the alloy compositions and especially the Co content differs, the phase diagram for the respective samples can be much different and lead to the formation of phases which are not necessarily ferromagnetic. Furthermore, the formation of soft magnetic α-(Fe,Co) phase is a known reason for low coercivity. A magnetic hardening can only be achieved by a controlled heat treatment resulting in a suitable microstructure. More systematic characterization of the microstructure is shown in the following, including elemental mapping by EDX, TEM and Kerr microscopy.

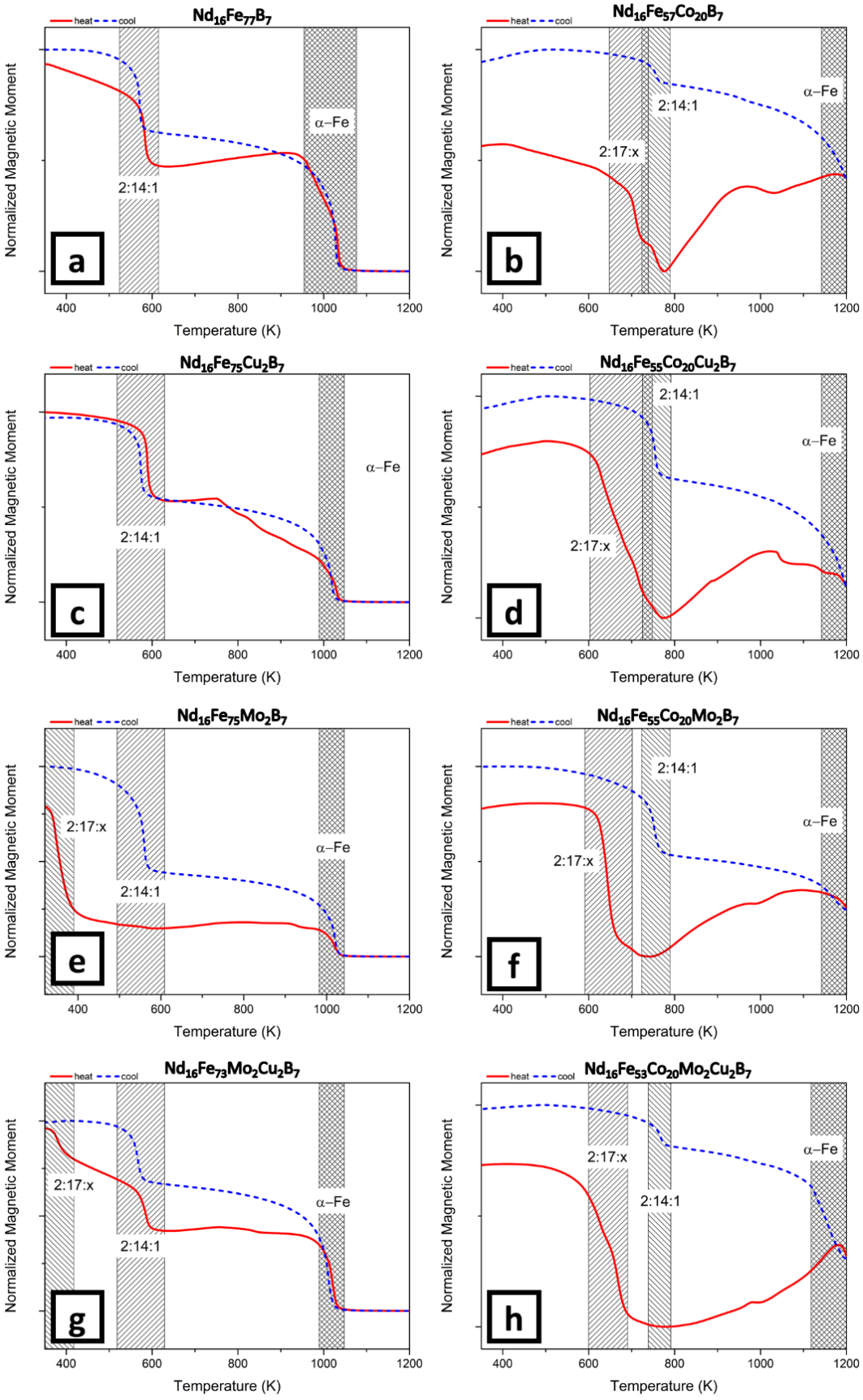

Figure 34: Thermomagnetic measurements of the Nd-Fe-Co-Mo-Cu-B samples in quenched state. The red curve shows the heating curve and the blue curve is cooling to initial state.

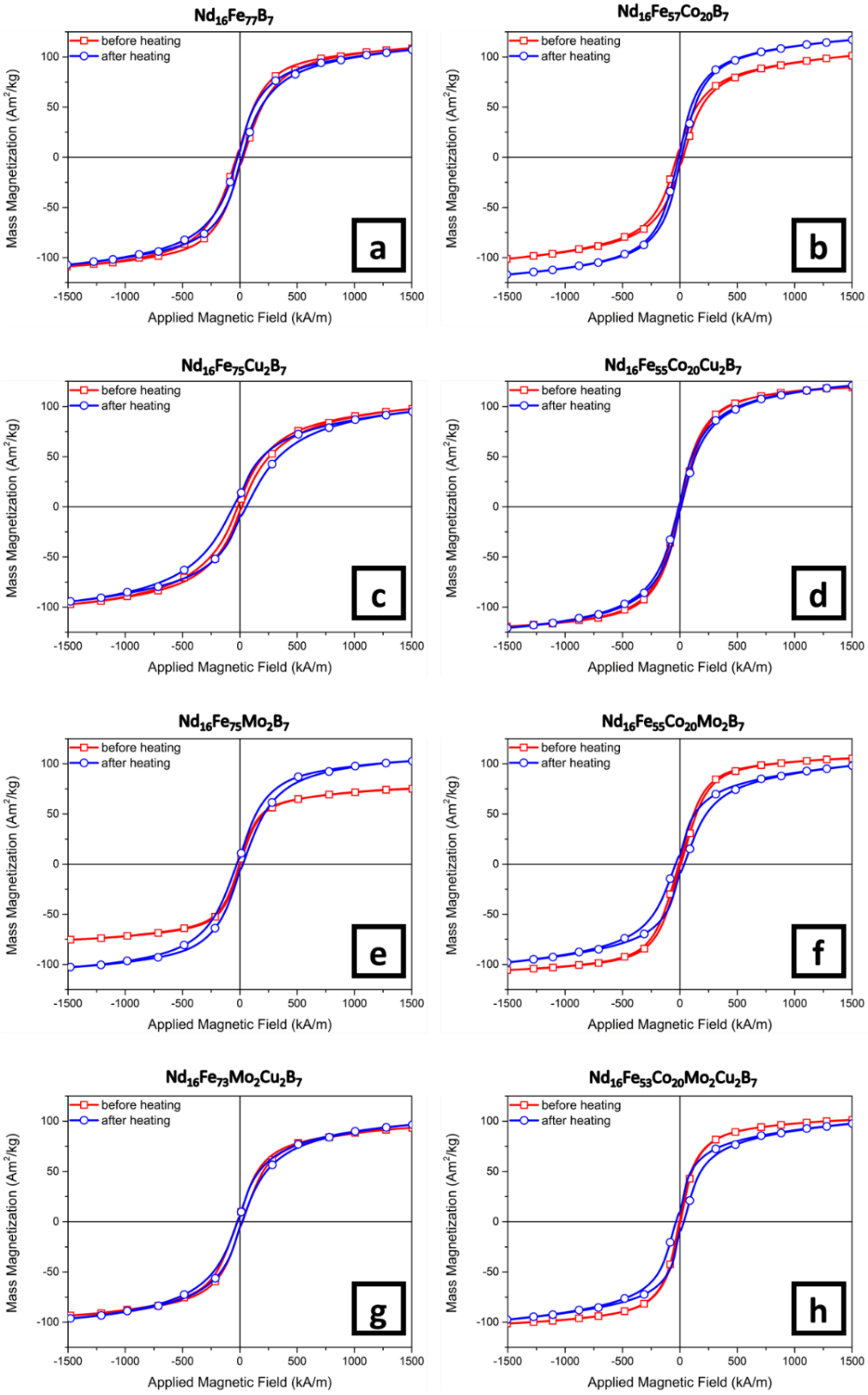

Figure 35: Magnetic hysteresis before and after thermomagnetic measurements of the Nd-Fe-Co-Mo-Cu-B samples. The samples are soft magnetic even after the annealing. This indicates that only a controlled annealing treatment leads to an increase in coercivity.

4.3. The Reason for Microstructural Transformation and Magnetic Hardening

The role of the annealing treatment for magnetic hardening in $Nd_{16}Fe_{53}Co_{20}Cu_2Mo_2B_7$ has been demonstrated. However, the microstructural transformation and the role of the substitutional elements on the microstructure and magnetic properties is yet unclear. So far, the importance of the element substitutions and resulting formation of the metastable phase becomes apparent when comparing the phase fraction of $Nd_2(Fe,Co)_{17}B_x$ with the achieved coercivity, shown in Figure 36. The magnetic hardening effect relies on the microstructural transformation and formation of the hard magnetic $Nd_2(Fe,Co)_{14}B$ phase. An increase in the phase fraction of $Nd_2(Fe,Co)_{17}B_x$ in as-quenched samples does therefore increase the effectiveness of the magnetic hardening by subsequent annealing. In this regard, simultaneously addition of Co, Cu and Mo only allows to obtain the largest fraction of the metastable phase and highest coercivity in this study. However, the true nature of the magnetic hardening effect is yet unclear.

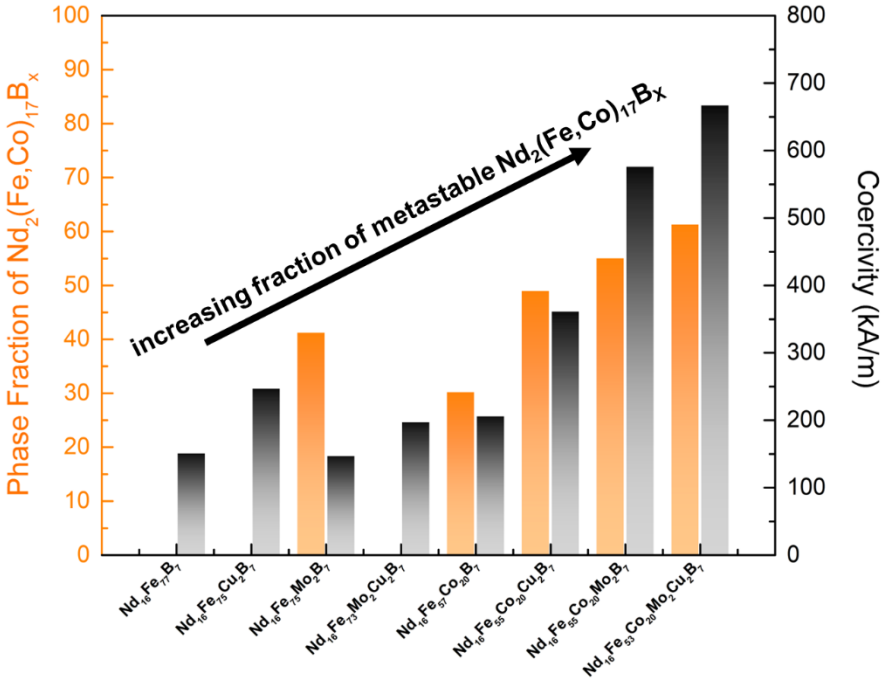

Figure 36: Correlation between the phase fraction of metastable $Nd_2(Fe,Co)_{17}B_x$ and the coercivity after annealing. The graph depicts that the magnetic hardening has a more powerful effect with increasing metastable phase fraction by addition of Co, Mo and Cu.

4.3.1. The Influence of Dopants on Phase Formation

To investigate the role of the elements on the phase stability and magnetic properties, qualitative element mapping using SEM-EDX is used to reveal the distribution of the elements Co, Cu and Mo in the quenched state (Figure 37, left) and after annealing (Figure 37, right) of the $Nd_{16}Fe_{53}Co_{20}Mo_2Cu_2B_7$ with highest coercivity. The mapping is performed on a representative region in the microstructure which contains all observed intermetallic phases. The distribution of Co, Cu and Mo for a sample in quenched state on the left (Figure 37 c, e , g) and the same sample after the annealing treatment (Figure 37 d, f , h).

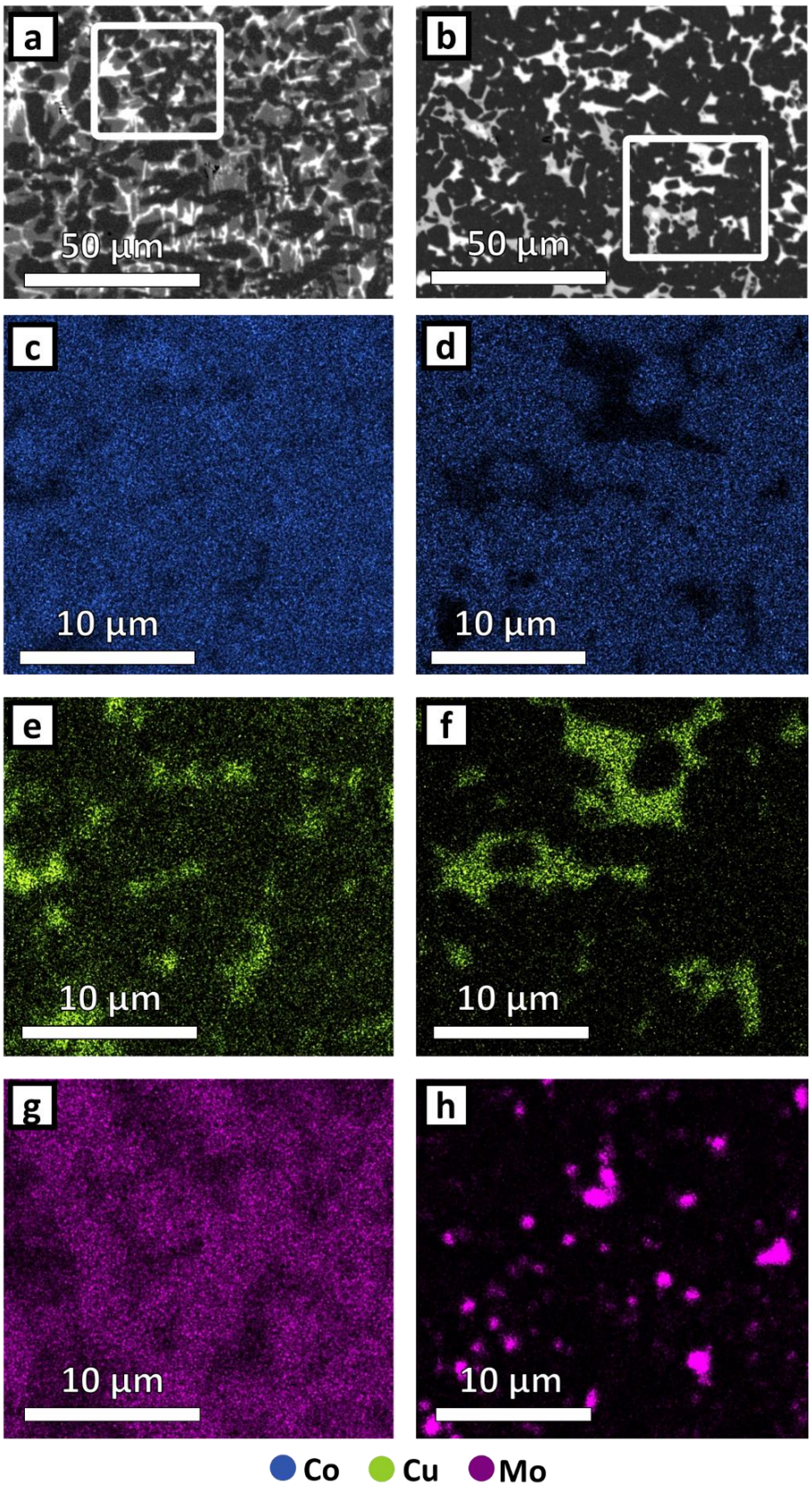

Figure 37: Qualitative element mapping by EDX of the substitutional elements in the quenched (left column) and annealed (right column) $Nd_{16}Fe_{53}Co_{20}Mo_2Cu_2B_7$ sample. The quenched state shows the occurrence of Co and Mo within the intermetallic grains, whereas the Cu seems to be localized in the grain boundary. After the annealing treatment, Co is found in the grains of hard magnetic $Nd_2(Fe,Co)_{14}B$ phase. The Cu is still localized in the grain boundaries whereas Mo is segregating by the temperature induced transformation.

The distribution of Co seems to be connected to the intermetallic ($Nd_2(Fe,Co)_{17}B_X$ and $Nd_2(Fe,Co)_{14}B$) grains both in quenched and annealed state. Local enrichments are not observed and the gaps can be attributed to the Nd-rich phase. The Cu distributions shows that this element is mainly found in the grain boundary and does not show a large solubility in the intermetallic phases. It resembles the negative of the Co distribution and appears to contribute mainly to the formation of intergranular Nd-rich matrix. In comparison, the Mo distribution shows a significant difference between the quenched and annealed state. In quenched state, the dendritic grains of the metastable phase can be seen by the Mo element contrast. The distribution is different from Co which indicates that Mo has a high solubility in the metastable phase but not in the other phases such as $Nd(Fe,Co)_4B$ or $Nd(Fe,Co)_2$. Apparently, the high solubility of Mo can be a reason to promote the formation of the metastable $Nd_2(Fe,Co)_{17}B_x$ phase.

4.3.2. TEM Investigation of the Microstructural Transformation

In order to observe the solid-state transformation of the metastable $Nd_2(Fe,Co)_{17}B$ phase, in-situ TEM annealing experiments (Figure 41**)** were performed on a quenched $Nd_{16}Fe_{53}Co_{20}Cu_2Mo_2B_7$ sample in cooperation with the *Advanced Electron Microscopy* division at TU Darmstadt. At first, a grain of the metastable phase was identified by EDX measurements (Figure 38) and electron diffraction (Figure 39). In agreement with the SEM-EDX results (Figure 37), a low Nd content and significant occurrence of Cu and Mo in the grain indicates, that it is not the hard magnetic $Nd_2(Fe,Co)_{14}B$ phase since its solubility for these elements is much lower.

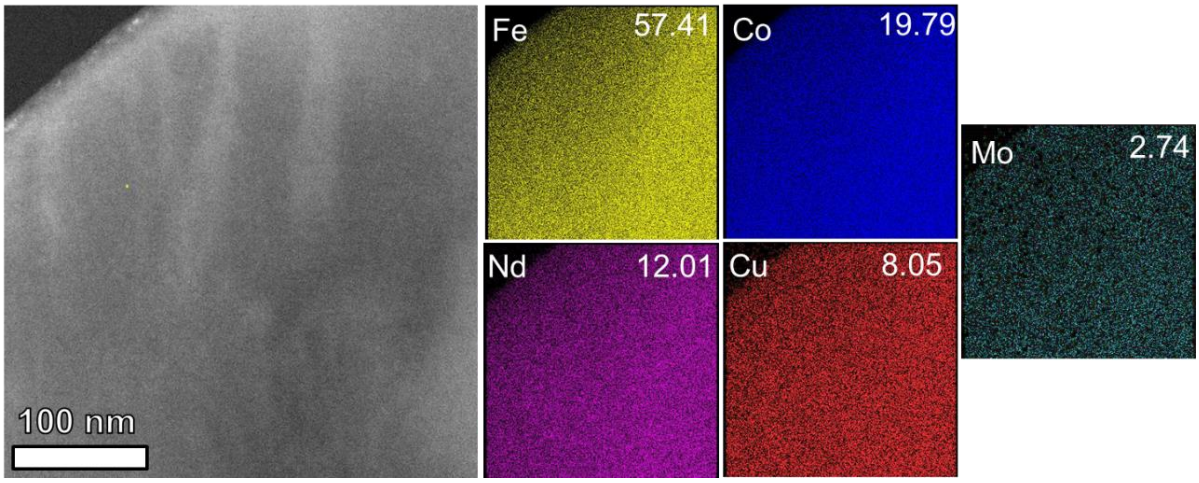

Figure 38: TEM-EDX mapping of the grain which was identified to be the metastable $Nd_2(Fe,Co)_{17}B$ and used for the in-situ annealing experiments.

In addition, the diffraction pattern of the grain selected for the in-situ experiments is consistent with the crystal structure of the Nd_2Fe_{17} phase which was extracted from the XRD measurements shown in Figure 30 and Figure 31. The simulated pattern and experimentally obtained pattern are shown in Figure 39, together with a high-resolution TEM image of the corresponding grain and the simulated FFT. Besides the identified metastable $Nd_2(Fe,Co)_{17}B_x$ phase, regions of with a crystal structure different from the $Nd_2(Fe,Co)_{17}B_x$ and $Nd_2(Fe,Co)_{14}B$ structure can be found which is attributed to the formation of a $Nd(Fe,Co)_4B$ phase in the quenched samples and has been shown in the SEM (Figure 29) and XRD investigations (Figure 30).

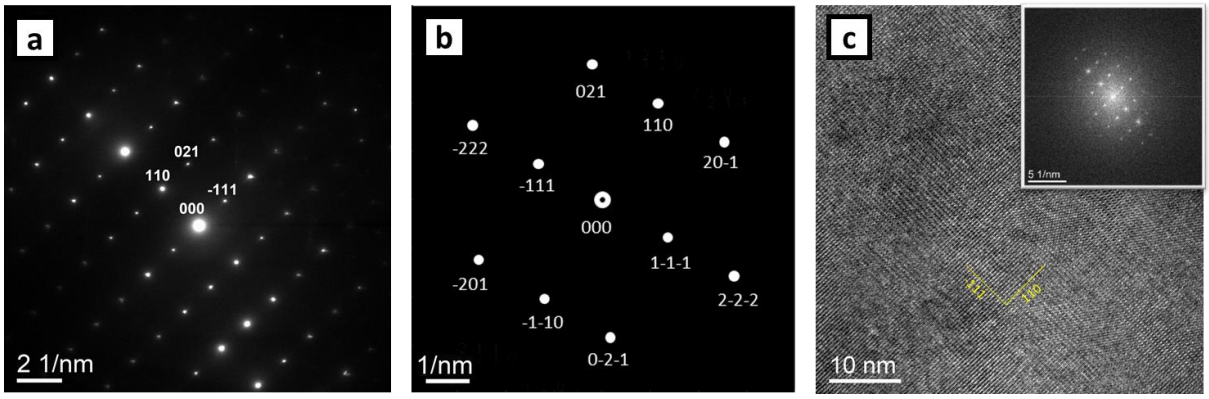

Figure 39: TEM investigation on the metastable $Nd_2(Fe,Co)_{17}B_x$ grain with a) diffraction pattern and indexed intensities along the Z = [1-12] zone axis together with the b) simulated diffraction pattern of the Nd_2Fe_{17} structure according to the XRD measurement and c) the corresponding HR TEM image with an insert of the FFT intensities.

The electron diffraction shown in Figure 40e) reveals a $CaCu_5$ type structure which agrees with the previous XRD investigations. Moreover, it is known that in the $CaCu_5$ type Nd-Co-B compounds, an ordered substitution of Boron for Cobalt is possible and several stoichiometries besides $NdCo_4B$ can occur such as $Nd_3Co_{11}B_4$ and $Nd_2Co_7B_3$ [150]. The investigations shown here indicate the formation of $NdCo_4B$ phase which has been observed in other rapid solidification experiments with Co-rich (Nd, Ce)-Fe-Co-B alloys [151], [152] showing the formation of such phases, specifically $NdCo_5$ and $NdCo_4B$. In this work, the role of the dopants in the $Nd_{16}Fe_{53}Co_{20}Cu_2Mo_2B_7$ alloy are yet unclear but could replace RE and/ or TM sites in this compound, respectively.

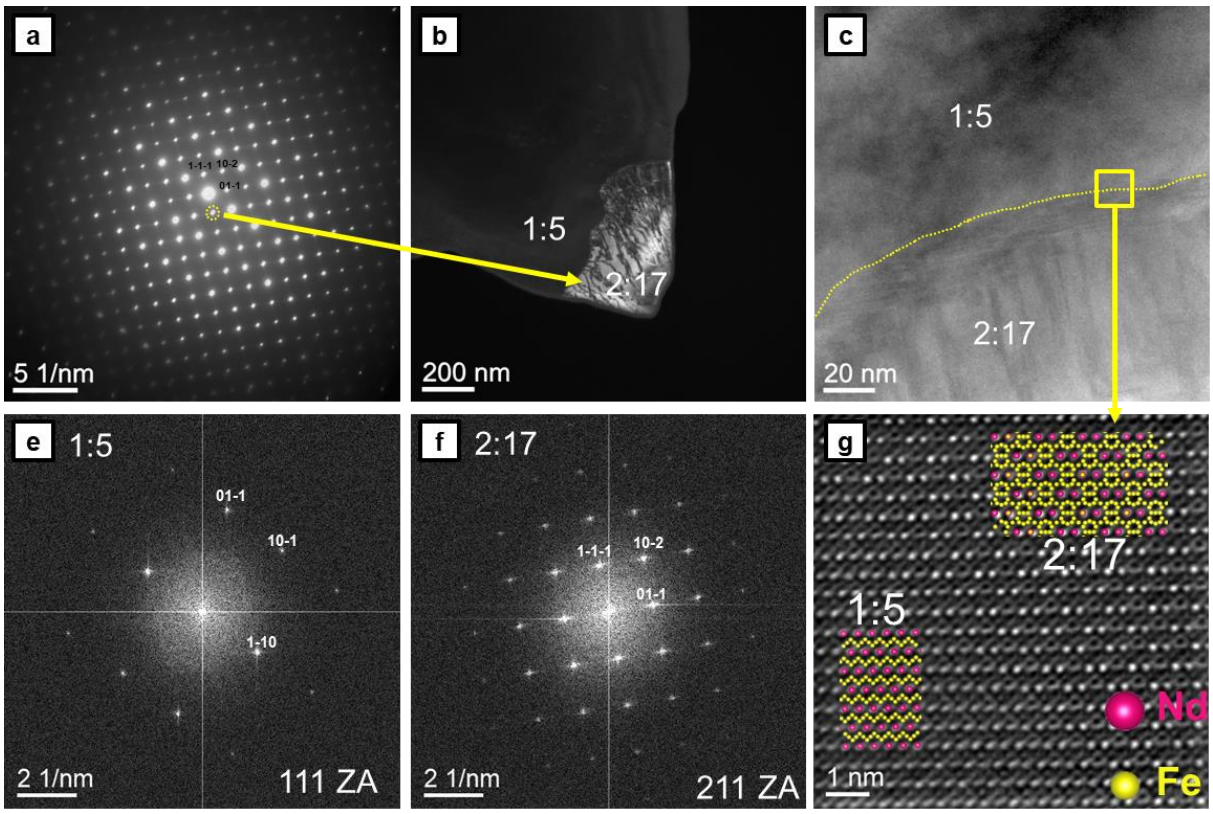

Figure 40: TEM investigation on a quenched $Nd_{16}Fe_{53}Co_{20}Cu_2Mo_2B_7$ sample. a) Shows the selected diffraction pattern of the b) $Nd_2(Fe,Co)_{17}B_x$ phase in bright contrast. c) Another phase with $CaCu_5$ crystal structure is observed in the sample which is adjacent to the $Nd_2(Fe,Co)_{17}B_x$ phase. g) atomic resolution with an overlay of the simulated crystal structures are shown together with the electron diffraction of the respective phases in e) and f).

Furthermore, this phase has not been observed after the annealing treatments neither by microscopy and XRD nor by thermomagnetic measurements which suggests that it is also metastable and must therefore be involved in the microstructural transformation like the $Nd_2(Fe,Co)_{17}B_x$ phase. However, further experiments are needed to explain the influence on the microstructure and magnetic hardening effect.

4.3.3. In-situ TEM Annealing Experiments on the metastable $Nd_2(Fe,Co)_{17}B_x$ Phase

For the in-situ annealing experiments, a homogeneous grain of the metastable $Nd_2(Fe,Co)_{17}B_x$ phase was selected as shown in Figure 38 and Figure 39. The by ion milling prepared sample was slowly heated on a sample TEM holder designed for this purpose. The images of the sample were continuously captured whereby the images in Figure 41 represent important microstructural transformations. During the heating experiments shown in Figure 41, the release of an amorphous phase out of the metastable $Nd_2(Fe,Co)_{17}B_x$ can be observed at a temperature around 600 °C. These are probably dissolvable elements (Mo and Cu) that are excluded from the metastable phase. At a temperature around 800 °C the transformation happens sudden, fast and crystal growth is observed, together with a thickening of the TEM sample. Unfortunately, this is the reason that the crystal structure and composition could not be determined afterwards. However, regarding the additional investigations of the microstructure by SEM and the magnetic characterization, it can be assumed that it must be the hard magnetic $Nd_2Fe_{14}B$ phase. Unfortunately, it was not possible to observe the formation of the Fe-Mo-B precipitates and possible intermediate crystal structures during the annealing. Nevertheless, the images demonstrate the thermal decomposition of the $Nd_2(Fe,Co)_{17}B_x$ together with the formation of a fine grained microstructure.

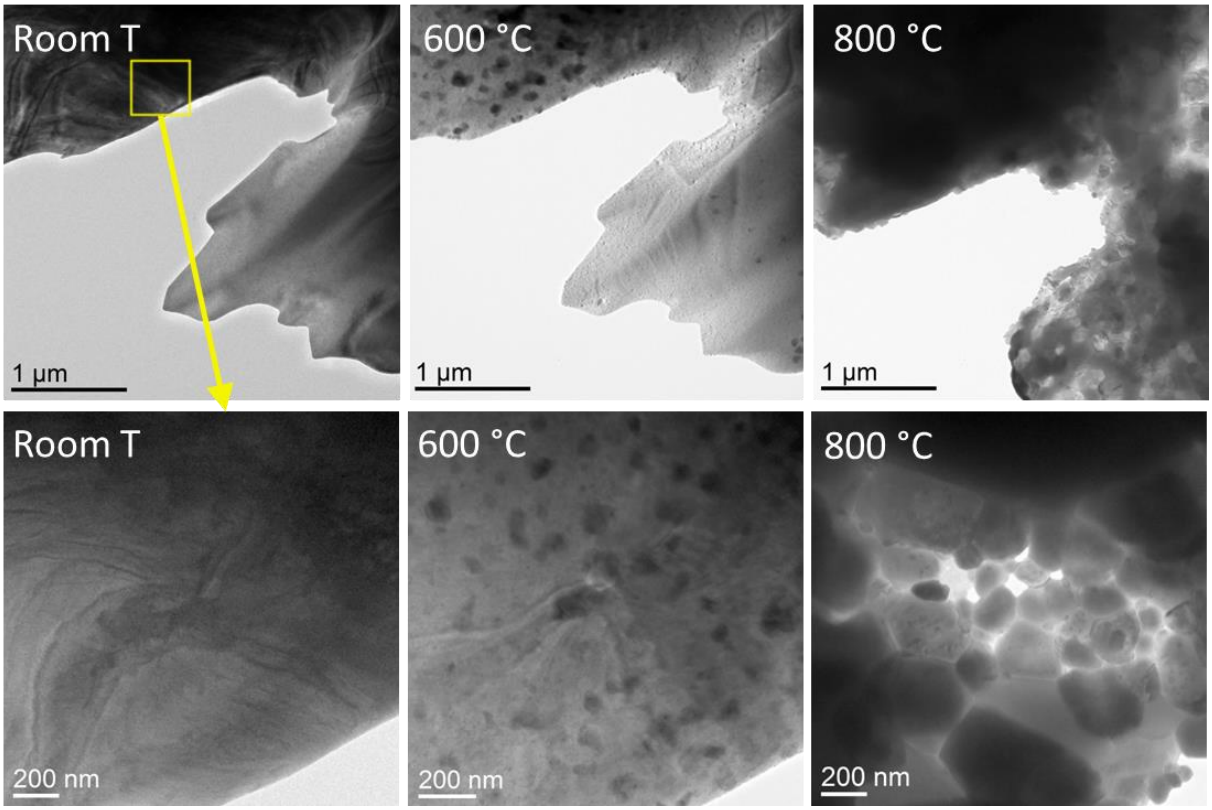

Figure 41: In-situ bright field TEM investigations of the metastable $Nd_2(Fe,Co)_{17}B_x$ phase upon heating. The upper row shows the microstructural transformation from room temperature up to 800 °C. The marked area indicates the region at higher magnification, which is shown in the lower row.

4.3.4. The Formation of Precipitates by Annealing

Even though the transformation of the microstructure is observed, the true reason for the increase in coercivity and the influence of the precipitates on the coercivity mechanism is unclear. As observed in the SEM-EDX mapping (Figure 37) and the in-situ TEM investigations in Figure 41, the annealing treatment leads to a decomposition of the metastable phase and segregation of Mo which is visible on micrometer scale. The local element enrichments indicate the formation of Mo containing intermetallic phases, however the previous characterization is not sufficient to verify the occurrence of this excretion. Therefore, a more detailed view on the microstructure of an annealed $Nd_{16}Fe_{53}Co_{20}Cu_2Mo_2B_7$ sample was done in cooperation with Dr. Andrey Mazilkin at the *Karlsruhe Nano Micro Facility* by using an aberration corrected Titan 80-300 TEM microscope (FEI Company) shown in Figure 42.

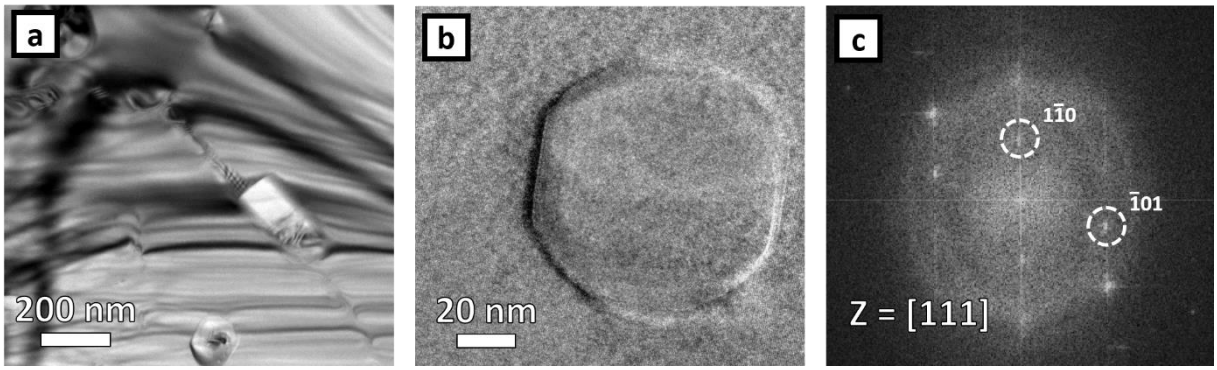

Figure 42: High Resolution - TEM images of the $FeMo_2B_2$ precipitates in the annealed $Nd_{16}Fe_{53}Co_{20}Mo_2Cu_2B_7$ sample. Image a) shows a triple junction between neighboring $Nd_2(Fe,Co)_{14}B$ grains with precipitates in the grain boundary and the grain interior. Image b) shows a precipitate at higher magnification and a non-epitaxial interface to the $Nd_2(Fe,Co)_{14}B$ matrix phase. The diffraction pattern in c) indicates the zone axis Z = [111] of the probed precipitate in b).

The images reveal that inter- and intragranular precipitates down to 10 nm in size are found within sample, besides the macroscopic precipitates up to 3 μm in size. In addition, electron diffraction on a free-standing particle in the sample could reveal the tetragonal crystal structure (No. 127; P4/mbm). Comparison between UCSD database and the Fast Fourier Transformed intensity of the diffraction pattern could prove that the precipitates are of the $FeMo_2B_2$ phase. In fact, the formation of precipitates and the beneficial effect on the magnetic properties has been shown by Shen et al. [153] in sintered Nd-Fe-Co-B magnets. The authors claim, that the addition of Mo leads to distortion in the $Nd_2(Fe,Co)_{14}B$ unit cell by partial substitution of Fe by Mo atoms, which is generally believed to decrease the magnetocrystalline anisotropy but can counteract the influence of high Co addition and therefore lead to a beneficial effect on coercivity. Moreover, the Mo enrichements are believed to increase the local nucleation field for reverse magnetic domains which leads to an increase in coercivity. At the same time, the secondary phase formation due to high Co addition (especially $Nd(Fe,Co)_2$) and the respective magnetic properties are believed to be altered and prohibited by Mo addition, prevailing the high coercivity. However, all claims of the authors cannot be confirmed. The quenched samples in this work are soft magnetic due to the absence of $Nd_2(Fe,Co)_{14}B$ phase. The subsequent heat treatment is necessary to form a microstructure of separated $Nd_2(Fe,Co)_{14}B$ grains which are the reason for an increase in coercivity. Here, the most important role of Mo (together with Co) is the stabilization of $Nd_2(Fe,Co)_{17}B$. The $FeMo_2B_2$ might have a beneficial effect on the separation of the $Nd_2(Fe,Co)_{14}B$ grains, however, the influence of Mo on the solidification behaviour resulting in a complex and instable microstructure after quenching is the foundation

for magnetic hardening. The increase in coercivity by heat treatment appears to be much more fundamental and a direct comparison to the sintering process of Nd-Fe-B magnets can be missleading.

4.3.5. Coercivitiy Mechanism and Hardening Mechanism

The observed formation of the metastable phase and complex microstructure is a suitable precursor to achieve fine grained microstructures and a separation of the hard magnetic grains by secondary intermetallic phases. As shown in Figure 43, the addition of Cu and Mo does lead to strong grain refining effect, which is known and agrees with observations on rapidly solidified Nd-Fe-B alloys [154]. However, although grain sizes of less than 10 μm could be reached within both the Nd-Fe-B and Nd-Fe-Co-B series, high coercivity could only be obtained by addition of Co, Cu and Mo which emphasizes the necessity for the solid-state transformation of the $Nd_2(Fe,Co)_{17}B$ phase, finally leading to well seperated and small $Nd_2(Fe,Co)_{14}B$ grains accompanied by high coercivity.

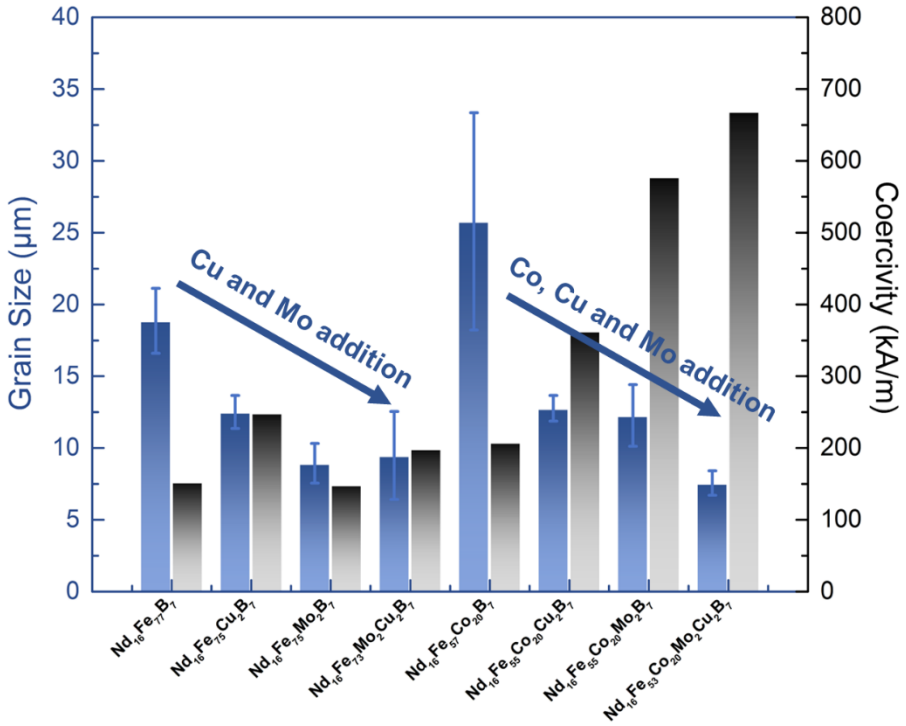

Figure 43: Correlation between the grain size of $Nd_2(Fe,Co)_{14}B$ and the coercivity after annealing. The graph depicts that Cu and Mo lead to grain refinement within the Nd-Fe-B and Nd-Fe-Co-B series. However, high coercivity can only be obtained by addition Co, Cu and Mo together.

The difference in magnetic properties of the $Nd_2(Fe,Co)_{17}B$ and $Nd_2(Fe,Co)_{14}B$ phase can be visualized by Kerr microscopy. The correspoding images of the $Nd_{16}Fe_{53}Co_{20}Mo_2Cu_zB_7$ with highest achieved coercivity is shown in Figure 44. The observed domains display the surface of randomly oriented, polished samples before (Figure 44a) and after the annealing (Figure 44b). The Kerr contrast in the metastable phase (Figure 44a) is very weak, however an undefined domain pattern in the grains is visible. Obviously, the metastable phase does not possess a strong uniaxial magnetocrystalline anisotropy which would lead to a pronounced Kerr contrast as it can be seen for the annealed sample with $Nd_2(Fe,Co)_{14}B$ grains (Figure 44b). In the corresponding annealed sample, the well-known stripe and star-like domains are observed

which represent the strong magnetocrystalline anisotropy of the $Nd_2(Fe,Co)_{14}B$ phase. Moreover, the grains do not seem to be magnetically coupled. The domains end and start at the grain boundaries which, together with the small grain size down to $<10\,\mu m$, resembles isotropic sintered Nd-Fe-B magnets with an idealized microstructure for high, nucleation controlled coercivity.

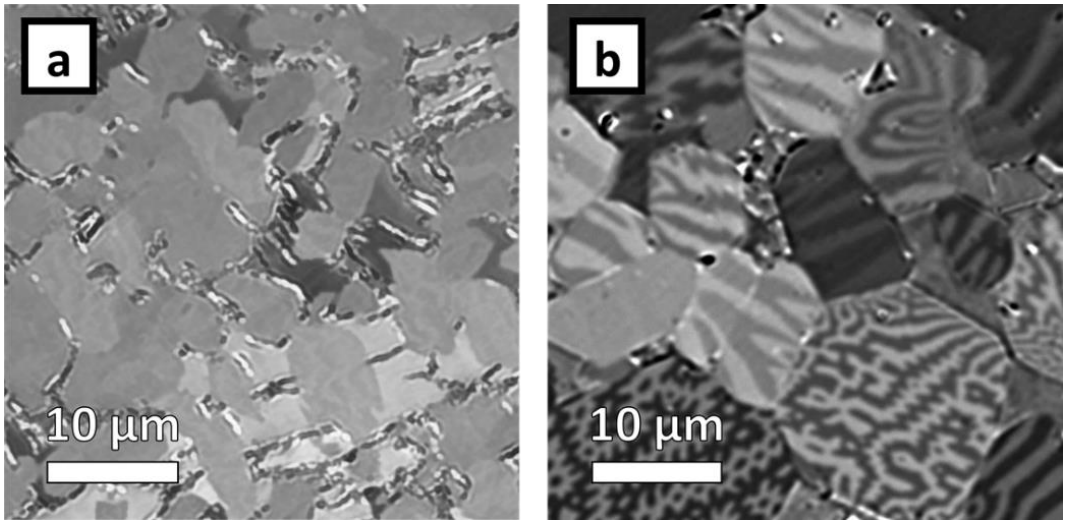

Figure 44: Kerr Microscopy of the a) quenched and b) annealed $Nd_{16}Fe_{53}Co_{20}Mo_2Cu_2B_7$ samples. The quenched sample shows no visible Kerr contrast in the grain boundary phase, which is found to be the paramagnetic $Nd(Fe,Co)_4B$. The grains of the metastable $Nd_2(Fe,Co)_{17}B_x$ phase show a weak Kerr contrast, indicating a ferromagnetic ordering but no uniaxial magnetocrystalline anisotropy. In contrast to this sample, the annealing leads the formation of the hard magnetic $Nd_2(Fe,Co)_{14}B$ phase with strong uniaxial magnetocrystalline anisotropy and pronounced Kerr contrast in image b).

The microstructure indicates a nucleation controlled coercivity mechanism which agrees with the initial magnetization of the corresponding samples. The magnetic susceptibility measured from the demagnetized state (Figure 45) does show a steep increase with low fields indicating the absence of strong pinning forces which would hinder the domain wall motion even at low fields.

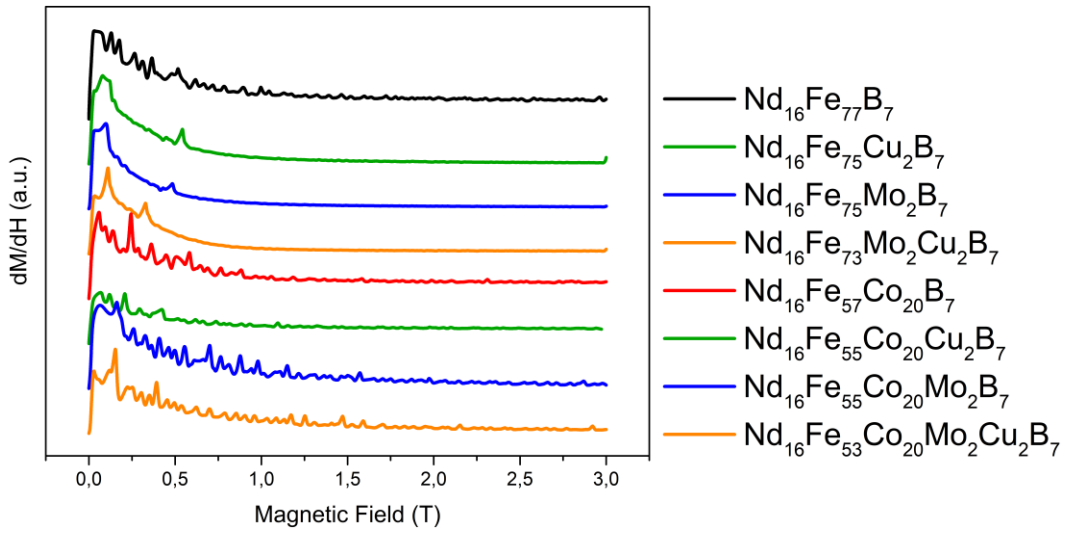

Figure 45: dM/dH over the applied magnetic field for the annealed samples. The initial magnetization shows high susceptibility in low fields, which indicates that no pinning forces against domain wall motion are present.

4.4. Magnetic Hardening in $Nd_{16}Fe_{53}Co_{20}Cu_2Mo_2B_7$ for Additive Manufacturing

Based on the magnetic hardening effect in Nd-Fe-Co-Mo-Cu-B samples, larger amount of material has been prepared by book mold technique. The chosen nominal composition was the same as in the previous experiments reaching coercivity up to $\mu_0 H_C$ = 1 T. The microstructure of the as-cast material and after the annealing treatment is shown in Figure 46.

The as-cast material shows a dendritic microstructure with large grain size which agrees with the expected features of the microstructure based on techniques such as induction or arc melting. The dendritic grains of $Nd_2(Fe,Co)_{14}B$ phase are embedded in a matrix of Nd,Cu-rich phase and intermetallic $Nd(Fe,Co)_2$ and $Nd(Fe,Co)_4B$. In comparison, the micrographs in Figure 46b) and d) represent the same material after a homogenization treatment for 3 days at 1000 °C. The left images represents the microstructure right after the homogenization treatment, which shows a more globular grain shape compared to the as-cast state. The same grain size and phases are observed in this sample. Most importantly, no formation of α-(Fe,Co) is observed. Furthermore, the annealing heat treatment intended for magnetic hardening does lead to very similar microstructures in both samples. The temperature profile shows a normalizing effect resulting in grains with high aspect ratio and size of several hundred μm.

The intention for the homogenization was to erase possible α-(Fe,Co) and increase the grain size of the intermetallic phases before milling in order to obtain a more brittle and homogeneous material which improves crushability of the obtained powder and possibly narrows the particle size distribution.

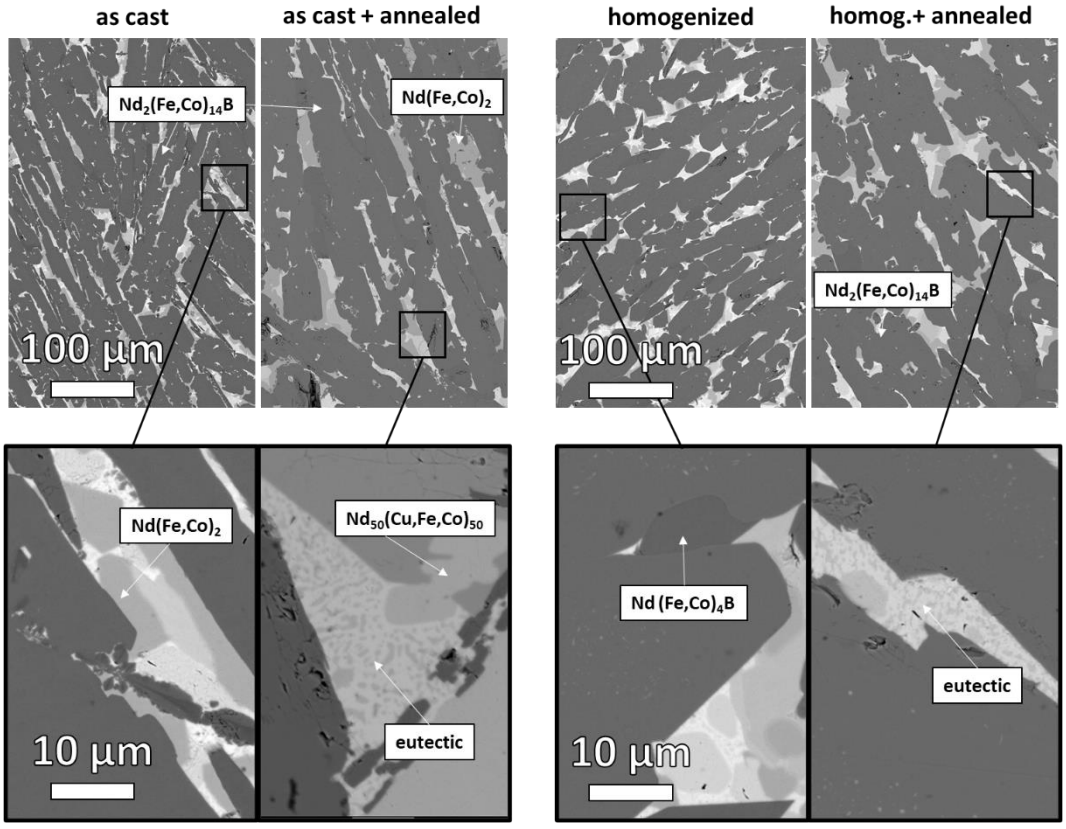

Figure 46: The SEM-BSE images show the microstructure of the ingot in as-cast state a) at low and c) higher magnification and the same sample after homogenization for 3 days at 1000 °C with b) low and d) higher magnification. The left part of the image corresponds to the as-cast state whereas the right insert represents the microstructure after heat treatment for magnetic hardening.

The powder for the PBF-LB experiments has been prepared by mechanical milling. The fractions between 20 μm and 63 μm have been separated by sieving. An exemplary SEM image (and corresponding image processing) and size distribution of the particles is shown in Figure 47. The first obvious observation is the irregular shape of the particles. Some of the particles show high aspect ratios and they tend to form agglomerates. The mean particle diameter is located around 26 μm which is already quite low for PBF-LB experiments. Furthermore, the image analysis reveals, that there are no particles above 50 μm present. A possible explanation can be the sieving process, during which the formation of agglomerates is problematic and can lead to the exclusion of particles close to the sieving mesh. In this case, it seems as if agglomerates above 63 μm are excluded although the distinct particles are smaller than the mesh. In summary, the results indicate that the irregular shape, high aspect ratio, wide particle size range and small average size are the reason for poor flowability and difficulties during the PBF-LB experiments.

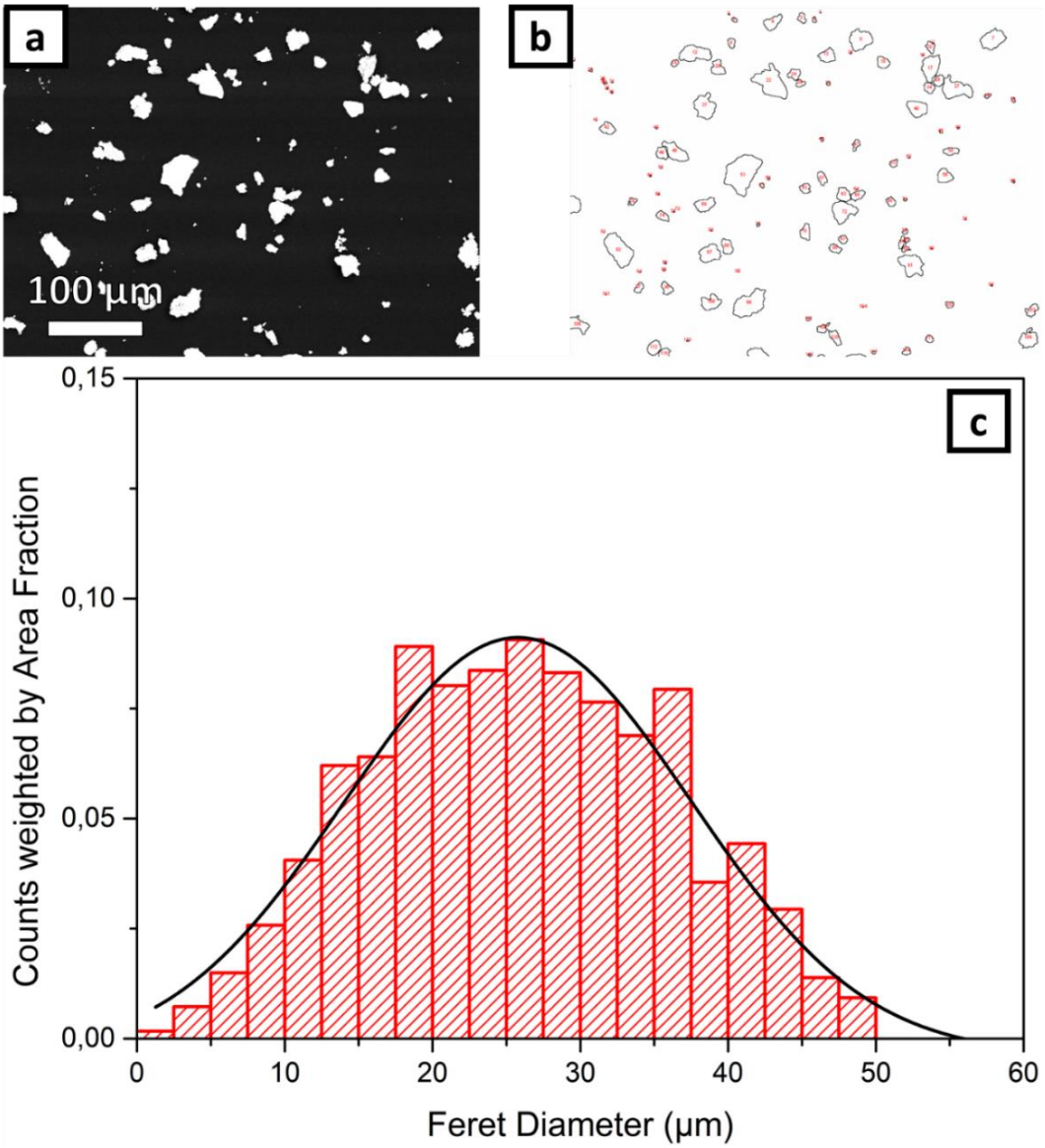

Figure 47: The images show examples of a) the SEM-BSE image of the powder particles of the optimized Nd-Fe-Co-Mo-Cu-B alloy for PBF-LB experiments and b) the corresponding image processing to quantify the Feret Diameter which is shown in c) in form of a histogram. Although the powders have been sieved by a 63 µm mesh size, the average diameter is much smaller.

Preliminary experiments on the printing behaviour of RE-based compounds have shown that the parameter space for printing is very narrow and the successful consolidation of powder until a bulk volume with defined geometry is difficult. In order to find an optimized parameter space for PBF-LB of the non-spherical powder, a methodology has been developed which was established for the work with such powders on laboratory scale. The successful cooperation with our colleagues, namely Jana Harbig, Julian Sebastian Storch and Holger Merschroth at the Institute for Production Management, Technology and Machine Tools has led to an internal standardized procedure for powder handling, process (parameter) optimization and characterization of functional magnetic materials. The method was specifically developed for material qualification using small amounts of powder < 100 ml with irregular shape, wide particle size distribution and poor flowability.

First, 1D line-scans are performed with variation of the line energy density. The quality feature is a continuous melt track which is optimized by tuning the scan speed in a subsequent experiment. In commercial production using AM techniques, high scan speeds are preferred to reduce the production time. However, the fast scan speeds can lead to negative effects on the consolidation and are a limiting factor. Looking at the definition for the line energy density E_l the correlation between laser power P_l and scan speed v_s becomes apparent.

$$E_l = \frac{P_l}{v_s * h}$$

Equation 18: Definition of line energy density.

The same E_l can be achieved by either very high or low laser power and scan speed. However, the melt track formation and width can be very different and will result in different hatch distances h to be used. From the measurable quantity of the melt track width S_{db}, the hatch distance can be estimated by the following formula which was modified based on the work of Meiners [155] and initially used the laser focus diameter F_d:

$$h \approx 0.7 * S_{db}$$

Equation 19: Estimation of the hatching distance h by using the melt track width S_{db}.

The fusion tests are examined by a light microscope and are shown in Figure 48 (1D). The corresponding parameters are given in the table below the image. For low laser power, no melting or discontinuous melting tracks of the powder on the platelet are observed. High laser power leads to vaporization of the entire powder material and of the uppermost layer of the substrate platelet. The characterization by light microscopy aims for the evaluation of continuity and homogeneity in width of the melt tracks. Possible and expected negative effects are the occurrence of the Balling effect, crack formation, evaporation and possible separation of alloying elements which are only investigated by light microscopy. The domain of the line energy density range in which continuous melting occurs is considered to be a possible indicator for the material-specific process window. The line energy density with the best appearance is used as a starting point for the subsequent tests. In this work, the most interesting region seems to be around a line energy density of 0.2 J/mm. The melt lines show a constant width, however, small artifacts can be observed which indicate Balling phenomena. Since there is no clear trend between laser power and Balling effect, the only possible explanation is the powder quality, distribution and layer thickness which can have an important impact on the condition of the melt track.

Based on the line experiments, the second step is the optimization of the two-dimensional melting behavior using the non-spherical powder. For the consolidation of several powder layers, the hatch distance is chosen based on the average melt track width from the previous step following Equation 19 resulting in a value of $\sim 90\ \mu$m. The powder was applied manually after each completed layer.

The parameters from the 1D experiments can only be indicative. Contrary to the very local and defined energy absorption during the line scans, the already solidified areas and residual powder can have a tremendous effect on the parameter space. The heat input associated with each exposed vector cannot be dissipated directly. Instead, an unknown portion of the thermal energy accumulates in the vicinity of the exposure, forming heat affected zones and giving rise to a complex solidification process. Furthermore, the powder layer thicknesses can differ by an undetermined factor due to the irregular shape and high aspect ratio of the non-spherical particles and the manual application of the powder. Therefore, it is necessary to investigate a parameter region which is only guided by the 1D line scan experiments. The corresponding images are given in Figure 48 (2D) with the respective printing parameters below.

1D line scans

Line Energy Density [J/mm] h = 90 µm	0,02	0,04	0,06	0,08	0,10	0,12	0,14	0,16	0,18	0,20	0,22	0,24	0,26	0,28	0,30	0,32	0,34	0,36	0,38
Laser Power [W]	10	20	30	40	50	60	70	80	90	100	110	120	130	140	150	160	170	180	190

2D area scans

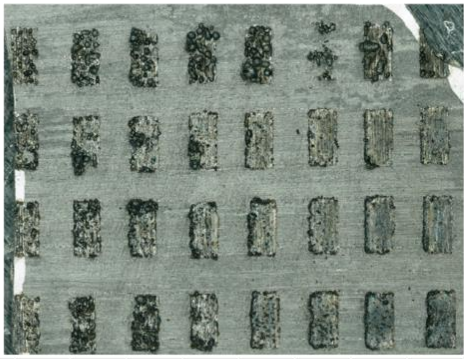

Line Energy Density [J/mm] h = 90 µm	0,08	0,11	0,14	0,17	0,20	0,23	0,26	0,30
25 W	213	277	179	147	125	108	96	86
75 W	938	682	536	441	375	326	288	258
125 W	1563	1136	893	753	625	543	480	431
175 W	2188	1590	1250	1029	875	761	673	603

3D bodies

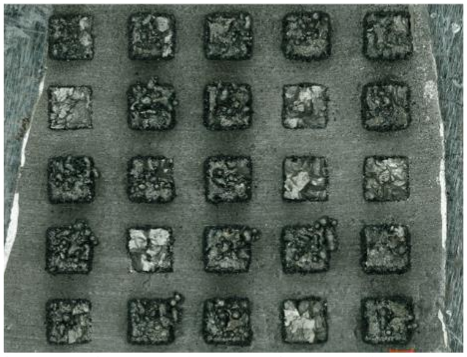

Line Energy Density [J/mm] h = 90 µm	0,16	0,18	0,20	0,22	0,24
110 W	688	611	550	500	458
	688	611	550	500	458
130 W	813	722	650	591	542
	813	722	650	591	542
150 W	938	833	750	682	625

Figure 48: Optical microscopy images and the corresponding printing parameters are shown. a) shows the 1D line scans to narrow the parameter space. B) shows the first area scans with 2 layers of powder. Finally, the printing of bodies is shown in c). Some of the samples show cracks and poor shape accuracy which is observed in several experiments with non-spherical powders.

It is important to mention that for easy comparison, the line energy density was calculated with a hatch distance of $h = 1$, which enables the direct comparison to the parameters of the 1D line scans. However, the actual hatch distance was calculated to be 90 μm. The most interesting region is above a line energy density of 0.2 J/mm and a laser power higher than 25 W. The surface seems to be smooth and continuous, contrary to the incomplete layers and Balling effect for low line energy density and laser power. The parameter region of interest agrees with the 1D experiments but seem to shift towards higher line energy densities.

The final step is the consolidation of 3D volume bodies with simple geometry by using the automated powder application and a parameter set based on the previous 1D and 2D experiments. The first obvious challenge is the powder layer application by the blade, which is not a trivial task for non-spherical powders. It is possible to estimate the effective layer thickness based on the particle size distribution.

$$d_{eff} = D_{90} * 1.5$$

Equation 20: Estimation of a suitable effective layer thickness d_{eff} based on the known particle size distribution and D_{90} value. [156]

However, the irregular shape and high aspect ratio of some particles does not necessarily follow this empirical rule. Therefore, the layer thickness was determined before the actual printing job. The distance between substrate and blade was increased until a uniform powder layer was realized. In this case, a suitable layer thickness was found to be 80 μm which is quite high compared to the particle size distribution but is influenced by the irregular shape of the particles. The scanning strategy was not under investigation. The scan vectors within one layer were parallel. Each following layer was rotated by 90 °.

The corresponding images and parameters are shown in Figure 48c). An apparent problem is the demolition of the samples by the blade during or after the powder application. Some of the samples show clear fracture surfaces and bad surface quality and shape accuracy. At this stage, it is not clear which aspect has the strongest influence on the print quality. Although the rheological properties of the powder are known to have a severe impact, the solidification of multiple brittle intermetallic phases and large temperature gradients can be the reason for the mentioned macroscopic defects and several reoccurring errors which are depicted in Figure 49.

Besides the incompletion of the print, the formation of cracks is the most severe problem. The related issues can be the demolition of the sample during printing but also the mechanical instability after the consolidation. It is important to mention, that cracking does occur within the sample but is always observed between the substrate and the built volume. This indicates that the thermal transport is not sufficient. A possible way to overcome this problem is the use of a heating stage which prevents thermal shock and reduces the thermal gradient between the local melt pool and previous solidified layers of powder and substrate. Besides the macroscopic defects, the SEM-BSE images in Figure 49 reveal microstructural characteristics which are based on the local and fast solidification of the material. Figure 49c) shows the formation of distinct inhomogeneities. Besides RE-rich accumulation in very bright contrast, regions of dendritic grain shape and distinguishable BSE contrast are observed. In case of the Nd-Fe-B based alloys under investigation, three phases are competing to be the primary solidification product, namely α-(Fe,Co), $Nd_2(Fe,Co)_{14}B$ and the metastable $Nd_2(Fe,Co)_{17}B_x$ phase. The indicated regions show the formation of α-(Fe,Co) which are not beneficial for the magnetic properties since this phase is soft magnetic. These regions are located at boundaries between melt tracks

indicating that surface defects such as oxide particles or evaporation of RE elements during the previous consolidation of a powder layer are the reason for the formation of inhomogeneities and α-(Fe,Co) phase. The only possible solution seems to be the prevention of oxidation by reduction of oxygen content during the printing.

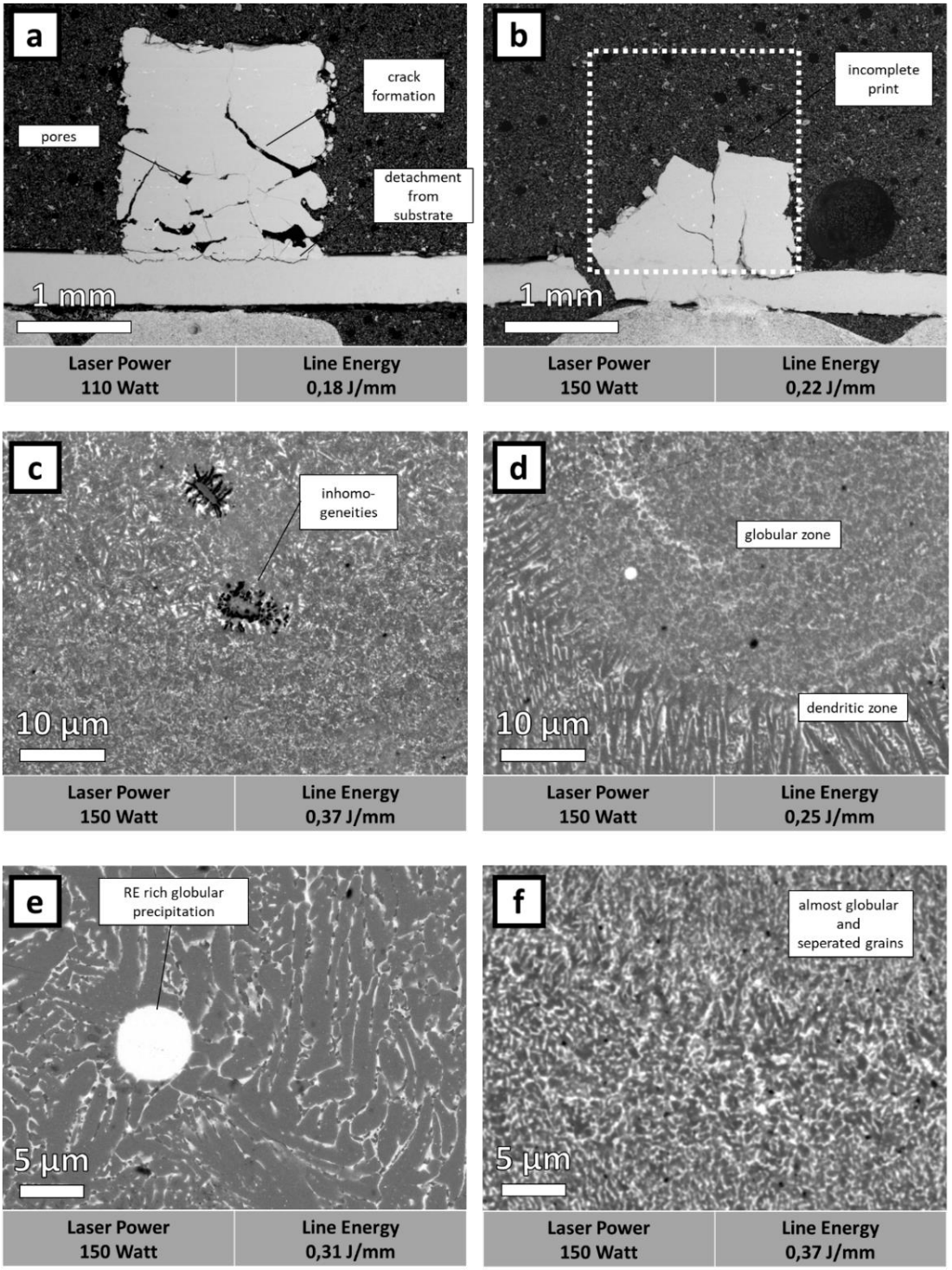

Figure 49: Reoccurring errors and features in the microstructure of RE-based samples produced by PBF-LB. The SEM-BSE images show the Nd-Fe-Co-Mo-Cu-B alloy after PBF-LB with marked characteristics. The corresponding printing parameters are listed below the image. The first obvious observation is the formation of cracks which all samples have in common. The cracking occurs within the sample and most importantly between the substrate and the printed body. During the automated printing process, uneven powder application or melting results poor shape accuracy, layer connectivity and even the tearing of the sample by the blade.

Related to the observed inhomogeneities are the boundaries of the melt tracks which show the occurrence of dendritic columnar grains. A sharp transition between a globular zone and the dendritic grains is visible. Most importantly, the growth direction of the dendrites relates to the printing direction which indicates the direction of the heat conduction. The SEM images indicate that an oriented growth can be possible by controlled thermal gradients. However, dendritic grains are not beneficial for the magnetic properties. Such grains usually show low coercivity, thus globular grains of the hard magnetic $Nd_2(Fe,Co)_{14}B$ are desired. The right SEM-BSE image in Figure 49f) depicts a microstructure region with almost ideal microstructure. The globular grains are below 5 μm and are well separated by a RE-rich grain boundary phase. Unfortunately, the BSE contrast reveals, that multiple phases are present and the hard magnetic $Nd_2(Fe,Co)_{14}B$ phase is accompanied by the formation of secondary phases.

A more detailed view on completed 3D body prints of this composition is given in Figure 50 which shows the samples in as-print state and after the annealing treatment which were all manufactured in the optimized parameter range.

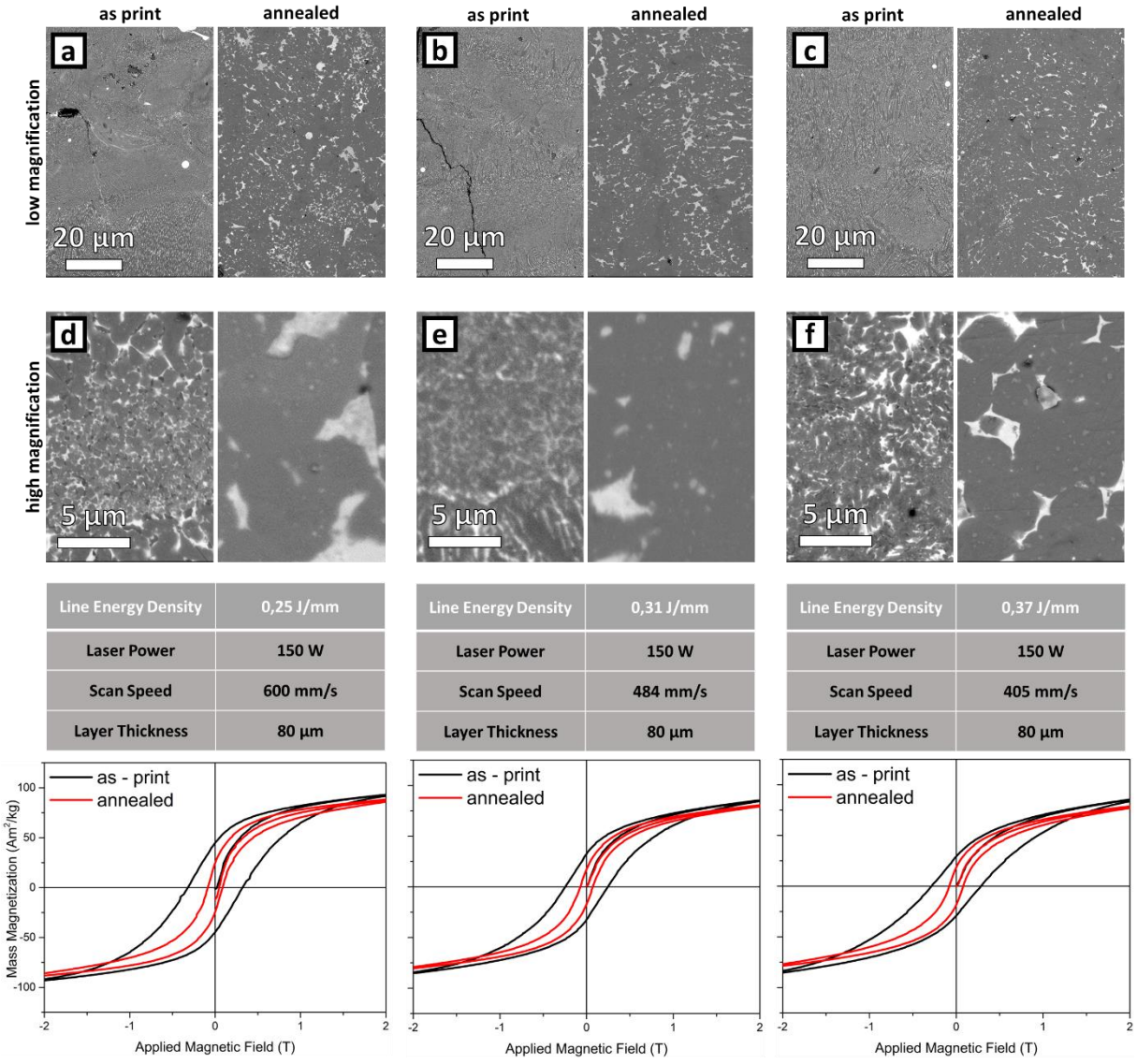

Figure 50: The SEM-BSE images show the microstructure of the Nd-Fe-Co-Mo-Cu-B alloy after PBF-LB with different parameters at low magnification (upper row) and higher magnification (bottom row). The corresponding sample in as-printed state is on the left whereas the right image shows the sample after annealing. The heat treatment leads to a severe change of the microstructure.

The corresponding printing parameters of the shown samples in SEM-BSE contrast are listed in the tables below the respective images, together with the magnetic hysteresis in as-print and annealed state. No clear trend or correlation in grain size and shape in dependence of the print parameters are found and the differences in microstructure are difficult to be assessed as it is generally very inhomogeneous. However, this does indicate that the developed parameter window was successfully narrowed by the chosen method and led to parameter sets of reproducible samples. The corresponding images in Figure 50a), b) and c) indicate different microstructural regions with both dendritic and globular grains. The melt tracks and heat affected zones cannot be distinguished easily. At higher magnification in Figure 50d), e) and f), the BSE contrast reveals that multiple intermetallic phases are forming, however the formation of α-(Fe,Co) could be suppressed in all samples. The only exceptions are the inhomogeneities which show clear distinguishable dark dendrites in BSE contrast (shown in Figure 49).

In comparison to the quenching experiments of the respective alloy, the observed microstructural features are very different. Dendritic grains of $Nd_2(Fe,Co)_{14}B$ are forming accompanied by the formation of intergranular $Nd(Fe,Co)_2$ and $Nd(Fe,Co)_4B$. The formation of $Nd_2(Fe,Co)_{17}B_x$ is not observed. After the annealing treatment, the grain size is increasing and bright precipitates can be observed within the $Nd_2(Fe,Co)_{14}B$ which indicate the $FeMo_2B_2$ phase. The corresponding micrographs after heat treatment are shown on the right and indicate interconnected grains of the $Nd_2(Fe,Co)_{14}B$ phase which are not favourable for high, nucleation controlled coercivity. Comparing these results to the previous experiments on the magnetic hardening of Nd-Fe-Co-Mo-Cu-B does clearly show that a direct adaptation to the production via PBF-LB is not possible. The highest obtained coercivity is measured for the samples in as-print state. However, it does not reach the expected coercivity of $\mu_0 H_C = 1$ T. In fact, the highest coercivity does barely reach $\mu_0 H_C = 0.5$ T. More systematic work on the annealing treatment and a refinement of the printing parameters is necessary to improve the magnetic properties. So far, the dendritic grains in as-printed state disappear and globular grains with intergranular intermetallic phases are present after subsequent annealing. This is accompanied by abnormal grain growth and interconnected grains which has a negative effect on the coercivity. Moreover, the observed inhomogeneities and high incidence of crack formation indicates that strong, local temperature gradients occur, which need to be monitored and controlled in subsequent investigations.

5. High Coercivity in Bulk Pr-Fe-Cu-B based Alloys by Temperature-Induced Microstructural Transformation

Parts of the results shown in this chapter 5 have already been reviewed and published. [135]

5.1. Alloy Modification and Development Regarding High Coercivity in Bulk State

The Pr-Fe-Cu-B alloy system is known to provide high coercivity without elaborate production techniques. The reason seems to rely on the well separated hard magnetic $Pr_2Fe_{14}B$ grains which are embedded in a multiphase matrix of Pr,Cu-rich grain boundary and an intermetallic $Pr_6Fe_{13}Cu$ phase. However, the analog material system based on Nd-Fe-Cu-B shows lower coercivity. First experiments reveal that although the same phases are present, the Pr-based system seems to possess much higher coercivity. The first composition and annealing treatment was adapted from literature whose corresponding SEM-BSE and magnetic properties are shown in Figure 51.

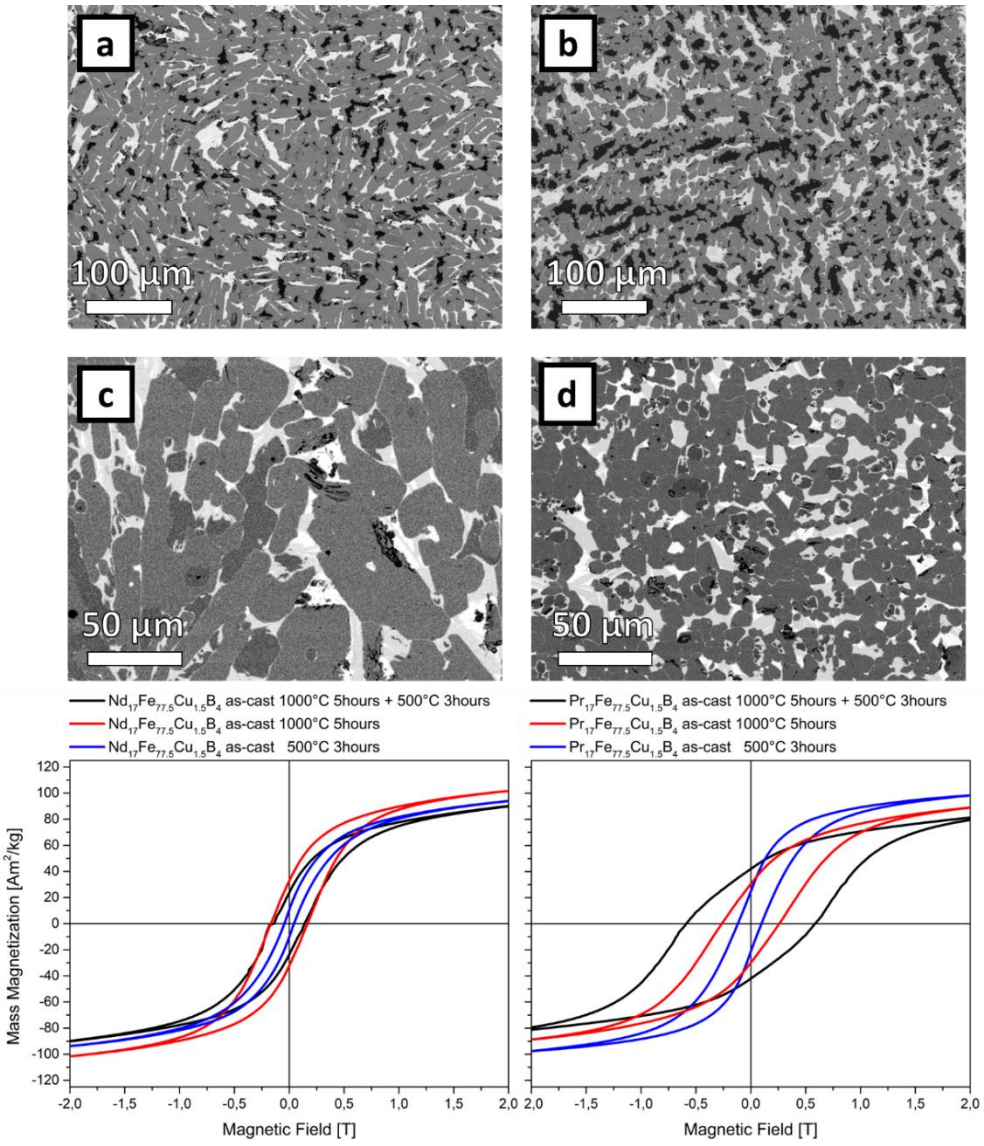

Figure 51: The initial composition of $(Pr,Nd)_{17.5}Fe_{77.5}Cu_{1.5}B_4$ was adapted from literature for initial tests. The comparison between the Nd-based (a, c) and Pr-based (b, d) compound with the respective hysteresis after different annealing conditions is shown. The combination of high and low temperature is necessary to develop full coercivity. However, substantial increase and large absolute coercivity is only found for the Pr-based sample.

The BSE images of the as-cast $Nd_{17.5}Fe_{77.5}Cu_{1.5}B_4$ sample are shown in Figure 51a). Like in the $Pr_{17.5}Fe_{77.5}Cu_{1.5}B_4$ (Figure 51b), hard magnetic 2:14:1 phase and α-Fe coexist in the sample. After the annealing treatment at 1000 °C and 500 °C, the α-Fe phase disappears, however $(Pr,Nd)_2Fe_{17}$ phase is forming in both samples. By comparing the annealed samples in Figure 51c) and d) the difference in grain size is prominent. Whereas the grains in the Nd-based samples are larger than 50 μm, even larger than in as-cast state, the Pr-based sample shows $Pr_2Fe_{14}B$ grains well below 50 μm. This can explain the difference in coercivity shown in the graphs below. Whereas the $Nd_{17.5}Fe_{77.5}Cu_{1.5}B_4$ shows coercivity below $\mu_0 H_C = 0.25$ T, the $Pr_{17.5}Fe_{77.5}Cu_{1.5}B_4$ sample reaches $\mu_0 H_C = 0.5$ T only by annealing of the as-cast state. It is important to mention, that the annealing treatment consists of a high temperature treatment at 1000 °C for 5 hours, followed by a low temperature annealing at 500 °C. Although these temperature regions are the same as in sinter treatments of Nd-Fe-B magnets, the microstructure in the presented samples completely changes. Furthermore, both annealing steps are necessary to develop full coercivity in the $Pr_{17.5}Fe_{77.5}Cu_{1.5}B_4$ sample.

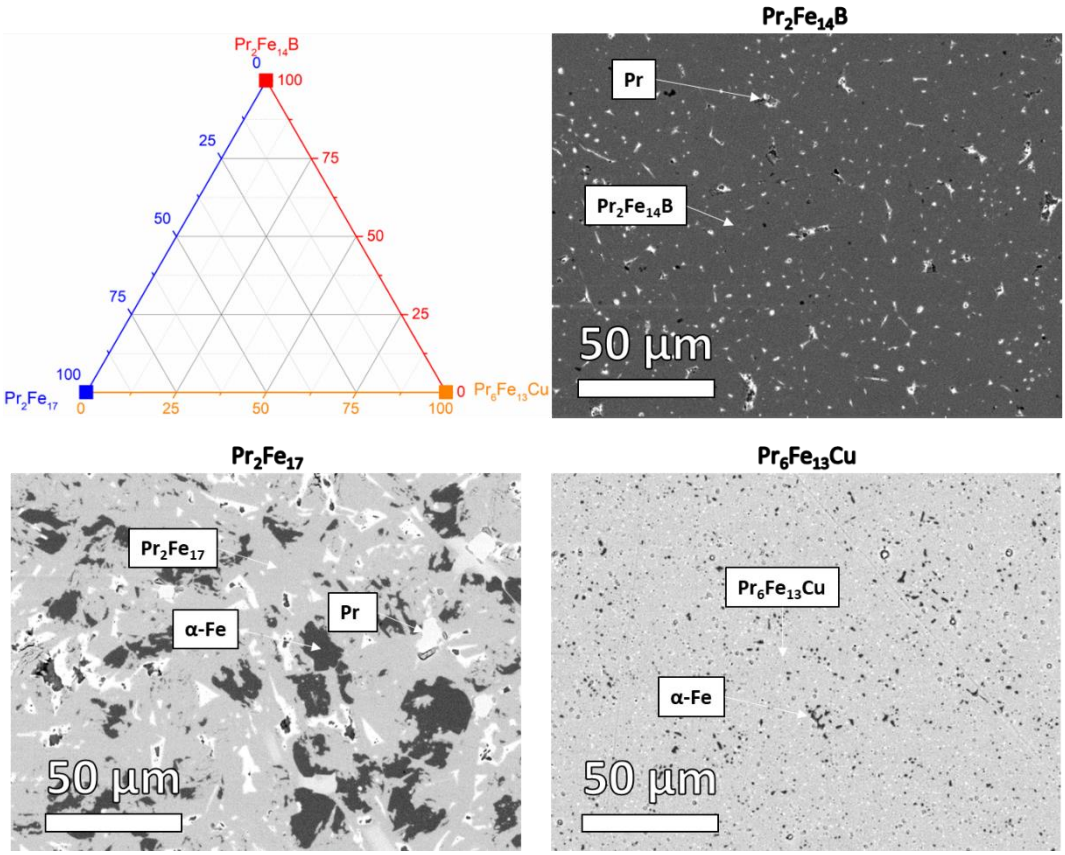

Figure 52: Master alloys for optimization. The mixtures for the screening tests are based on the $Pr_2Fe_{14}B$, $Pr_6Fe_{13}Cu$ and binary Pr_2Fe_{17} phases. The SEM-BSE images show, that already the initial sample show multiple phases in the microstructure. The attempts to achieve single phase material did not work. The master-alloys are used to screen the phase diagram by mixing calculated amounts by arc melting.

Further optimization of the Pr-Fe-Cu-B material system regarding the coercivity is shown in the following chapter. The practical approach is based on a quasi-ternary phase diagram bounded by the intermetallic phases which are found in the annealed samples. Therefore, master alloys of Pr_2Fe_{17}, $Pr_2Fe_{14}B$ and $Pr_6Fe_{13}Cu$ are prepared by induction melting and mixtures of the respective marked points in the diagram are prepared by arc melting and subsequent suction casting in a rectangular Cu mold forming a cavity of 5 x 1 x 50 mm. The corresponding SEM-

BSE images are shown in Figure 52. The samples in as-cast state show already a multiphase microstructure. The corresponding magnetic properties show soft magnetic behavior.

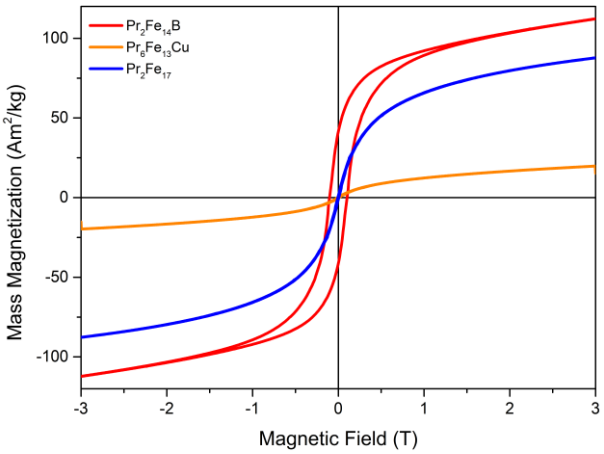

Figure 53: Magnetic properties of the master alloys used for the investigation of a quasi-ternary phase diagram.

The first approach was a broad compositional screening of the phase diagram as seen in Figure 55. The annealing treatment was kept the same for all samples and included a high temperature treatment at 1000 °C for 5 hours and a low temperature annealing at 500 °C for 3 hours. The SEM-BSE images show the occurrence of the same three phases, namely Pr_2Fe_{17}, $Pr_2Fe_{14}B$ and $Pr_6Fe_{13}Cu$. Sample 1 is located close to the $Pr_2Fe_{14}B$ phase and shows the smallest grain size of the series. However, the coercivity is quite low. Approaching the corner of Pr_2Fe_{17} does decrease the coercivity even further, since the fraction of soft magnetic Pr_2Fe_{17} increases. Sample 2 shows, that the $Pr_2Fe_{14}B$ phase forms a matrix with Pr_2Fe_{17} inclusions. Further increase leads to large grains of Pr_2Fe_{17} phase which are separated by a RE-rich grain boundary phase. Small inclusions of the $Pr_2Fe_{14}B$ are present, still, the coercivity is low. Approaching the $Pr_6Fe_{13}Cu$ corner does not improve the coercivity. Grains of Pr_2Fe_{17} are separated by the $Pr_6Fe_{13}Cu$ phase and small needle like grains of $Pr_2Fe_{14}B$ are observed. Even though sample 5 is located in the corner of $Pr_6Fe_{13}Cu$, large grains of the Pr_2Fe_{17} phase are observed which indicate the high stability of this phase. As soon as the Boron content is rising, the coercivity increases significantly. Both samples 6 and 7 show a very fine-grained microstructure with both $Pr_2Fe_{14}B$ and Pr_2Fe_{17} phase embedded in a $Pr_6Fe_{13}Cu$ matrix. Both samples reach a coercivity above $\mu_0 H_C$ = 1 T.

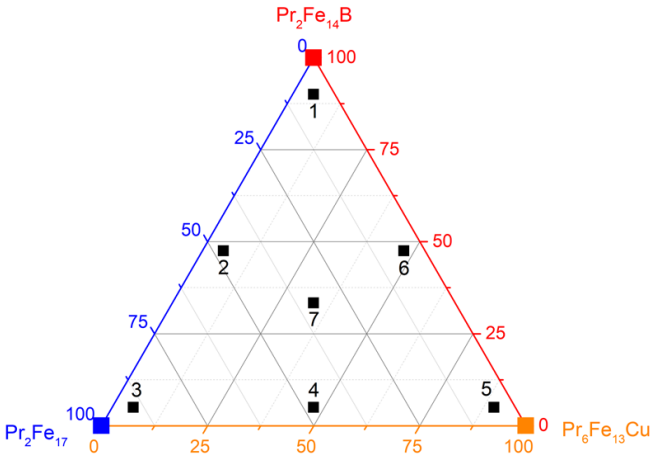

	Nominal Composition (atm. %)			
Point	**Pr**	**Fe**	**Cu**	**B**
1	12,6	81,8	0,3	5,3
2	12,1	84,9	0,3	2,8
3	11,6	87,9	0,3	0,3
4	19,8	77,5	2,4	0,3
5	28,1	67,1	4,5	0,3
6	20,4	74,5	2,4	2,8
7	17,4	78,9	1,7	2,0

Figure 54: Quasi-ternary phase diagram and the corresponding magnetic properties after annealing treatment for the marked samples.

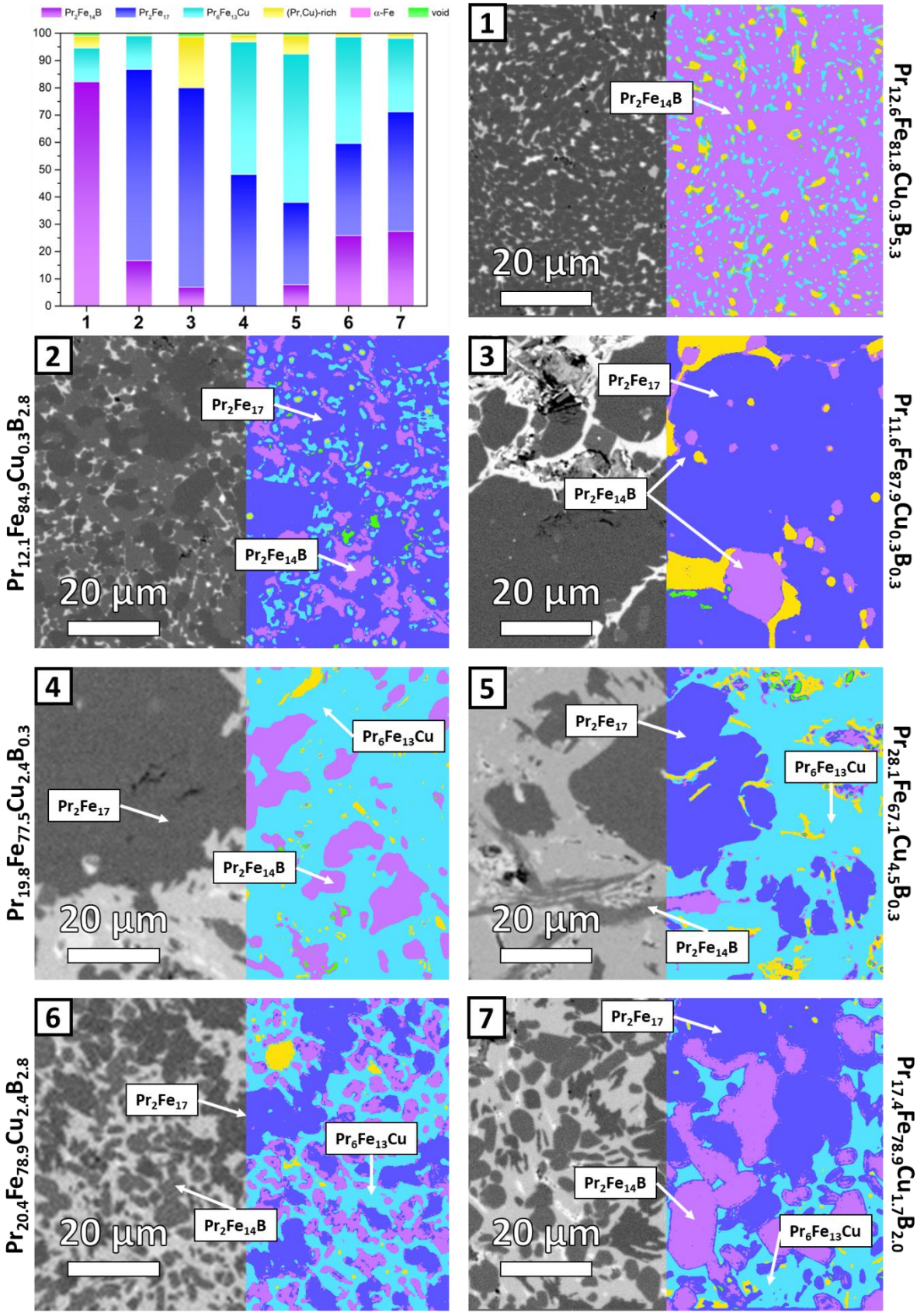

Figure 55: Optimization based on a quasi-ternary phase diagram. The SEM-BSE images and segmentation results are shown for the respective samples. The occurring phases are indicated and quantified. The phase fractions are given in the bar chart.

It is important to mention that the Pr_2Fe_{17} phase is found in every sample and no α-Fe phase could be observed. The high stability of the Pr_2Fe_{17} can be explained by the low Boron content in this phase diagram and the annealing treatment. The magnetic hysteresis indicate that the soft magnetic properties of this phase do deteriorate the hard magnetic properties. Even though high coercivity could be achieved, the hysteresis shows a kink in the second quadrant which indicate that fractions of the sample have low coercivity. However, the overall coercivity seems to be secured by a strong decoupling and separation of the hard magnetic $Pr_2Fe_{14}B$ phase. The matrix of $Pr_6Fe_{13}Cu$ phase seems to play an important role in the coercivity mechanism and is related to the hard magnetic properties of the samples.

5.2. Investigation of Coercivity in a Quasi-Ternary Phase Diagram

Based on the previous, broad screening of the phase diagram, it can be concluded that a certain amount of Boron is necessary not only to form the $Pr_2Fe_{14}B$ phase but also to prevent excessive amount of Pr_2Fe_{17}. At the same time, the formation of $Pr_6Fe_{13}Cu$ seems to have a beneficial effect on the coercivity. Therefore, further systematic investigations have been made by mixing master alloys of $Pr_6Fe_{13}Cu$ and I) FeB, II) Fe_2B and III) $Pr_2Fe_{14}B$ phase by arc melting. The ratios represent the percentage of formula units which were mixed based on the atomic percentages and used to calculate the necessary masses for the mixtures. The corresponding nominal compositions in atomic percentage are listed in the following table:

Table 4: Nominal compositions of the pre-alloy mixtures derived from the experiments in the "quasi-ternary" phase diagram in atomic percentage.

	$Pr_6Fe_{13}Cu$ + FeB				$Pr_6Fe_{13}Cu$ + Fe_2B				$Pr_6Fe_{13}Cu$ - $Pr_2Fe_{14}B$			
	Pr	**Fe**	**Cu**	**B**	**Pr**	**Fe**	**Cu**	**B**	**Pr**	**Fe**	**Cu**	**B**
80+20	25,4	64,1	3,9	6,7	25,4	60,7	3,9	10,0	28,2	66,7	3,9	1,1
70+30	22,2	64,4	3,4	10,0	22,2	59,4	3,4	15,0	26,5	68,4	3,4	1,7
60+40	19,0	64,7	2,9	13,3	19,0	58,0	2,9	20,0	24,7	70,0	2,9	2,3
50+50	15,9	65,0	2,4	16,7	15,9	56,7	2,4	25,0	23,0	71,7	2,4	2,9
40+60	12,7	65,4	2,0	20,0	12,7	55,4	2,0	30,0	21,3	73,4	2,0	3,4

I) $Pr_6Fe_{13}Cu$ + FeB

The SEM-BSE images and magnetic properties of the first series is shown in Figure 56. Large amount of FeB phase results in a microstructure with mainly $Pr_2Fe_{14}B$ phase and α-Fe for $Pr_{12.7}Fe_{65.4}Cu_2B_{20}$. Increasing the $Pr_6Fe_{13}Cu$ content induces the formation of a Pr,Cu-rich grain boundary phase and the coercivity is increasing, which can be seen in Figure 59b. The best sample with a coercivity of $\mu_0 H_C \sim 1.5$ T has been achieved for $Pr_{22.2}Fe_{64.4}Cu_{3.4}B_{10}$. This value is extraordinarily high for bulk samples. Obtaining such coercivity, in sintered and hot-pressed magnets, is not a trivial task. However, the Pr content is much higher compared to commercial magnets. The hard magnetic grains are fully diluted into a wide, continuous grain boundary phase. The hysteresis of all samples shows a kink in the demagnetization curve. This effect does generally indicate that fractions of the sample have lower coercivity. In this case, it can be assigned to grains of $Pr_2Fe_{14}B$ which are in direct contact and not magnetically decoupled but also to residual soft magnetic phases such as the Pr_2Fe_{17}.

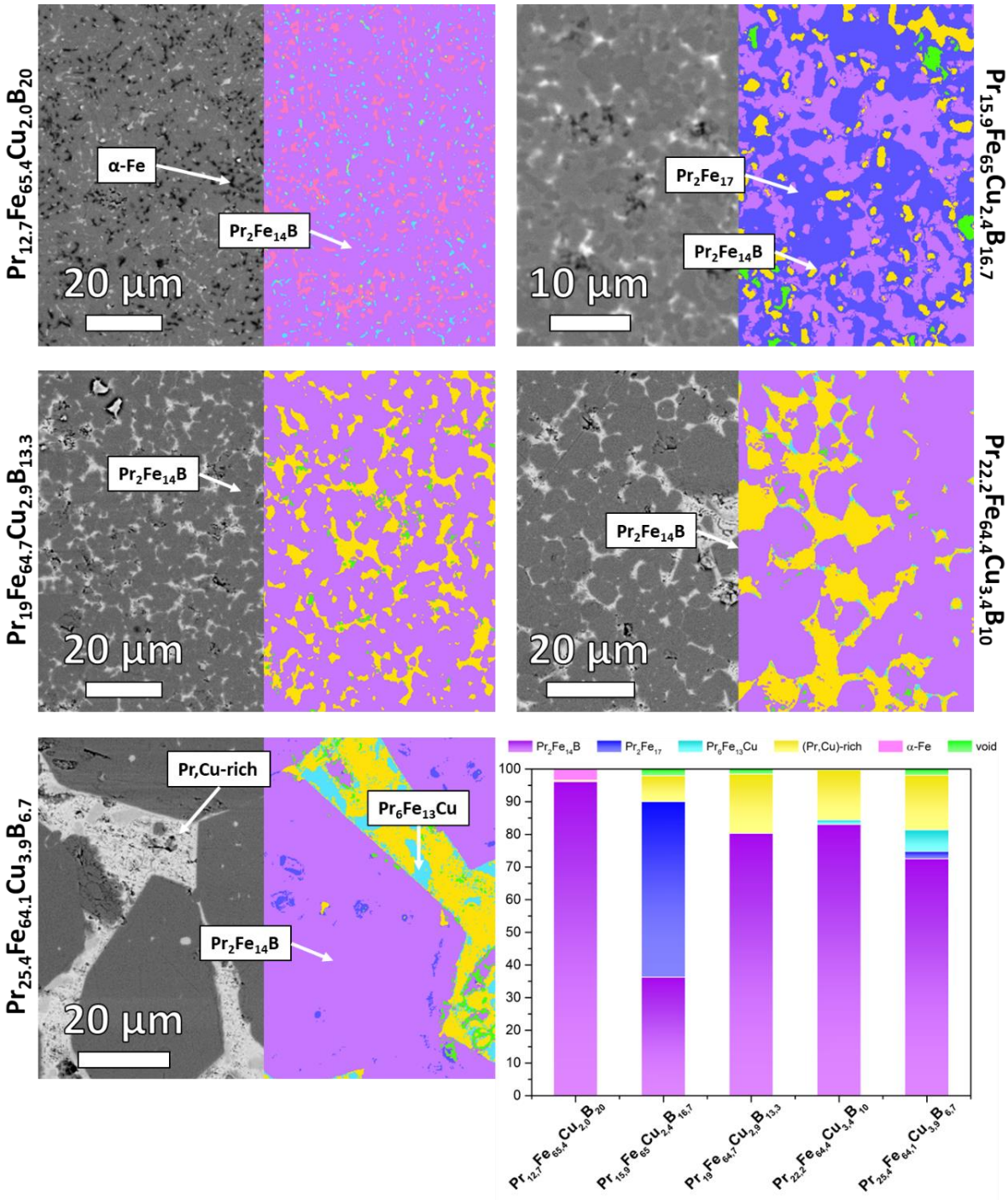

Figure 56: Further optimization approaches was done by mixtures of $Pr_6Fe_{13}Cu$ and FeB phase. Quantification of phase fractions from the SEM-BSE images of the corresponding samples after annealing is done by using a Trainable Weka Segmentation script. The phase fractions are given in the bar chart.

I) $Pr_6Fe_{13}Cu + Fe_2B$

Similar to the previous series, small amount of Fe_2B phase does lead to the formation of α-Fe and poor coercivity as seen for $Pr_{25.4}Fe_{60.7}Cu_{3.9}B_{10}$, with the corresponding hysteresis in Figure 59c. In fact, only the sample with equal mixture and composition of $Pr_{15.9}Fe_{56.7}Cu_{2.4}B_{25}$ shows coercivity of $\mu_0 H_C$ = 0.5 T. This series indicates that certain addition of Boron is necessary to form the $Pr_2Fe_{14}B$ phase but increasing the Fe content does not enable high coercivity. However, the magnetic hysteresis of the samples does not show the kink in the second quadrant. In comparison to the previous sample series, the microstructure does also contain interconnected

hard magnetic grains and the formation of soft magnetic phase. The true reason for the kink is therefore not clear.

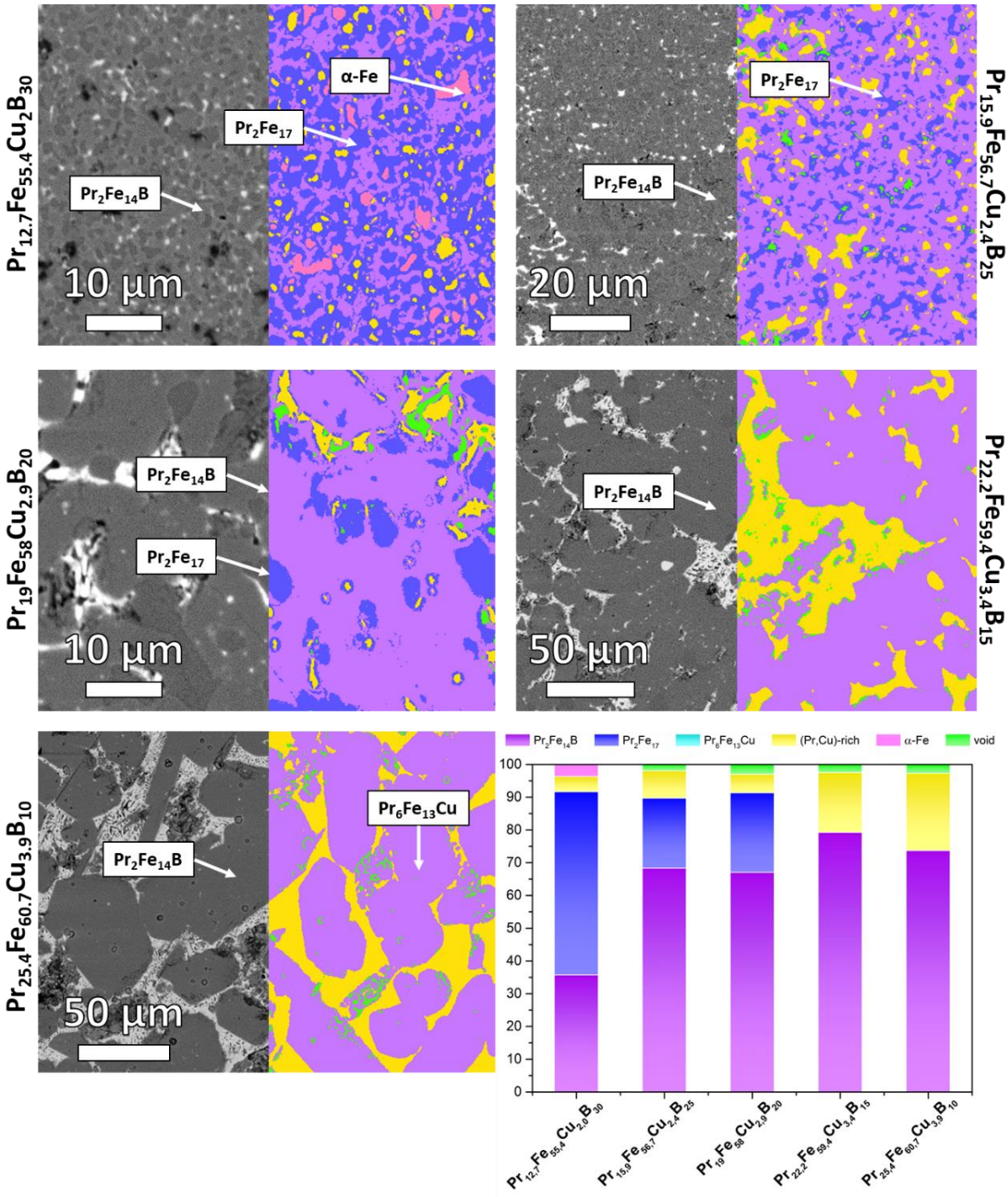

Figure 57: Further optimization approaches was done by mixtures of $Pr_6Fe_{13}Cu$ and Fe_2B phase. The images show main fraction of $Pr_2Fe_{14}B$ phase. Quantification was done by using a Trainable Weka Segmentation script in ImageJ. The corresponding phase fractions are given in the bar chart.

I) $Pr_6Fe_{13}Cu + Pr_2Fe_{14}B$

The last series shows an interesting effect. All samples consist of $Pr_2Fe_{14}B$ grains embedded and separated by a thick matrix of $Pr_6Fe_{13}Cu$ phase. Although Pr_2Fe_{17} phase can be observed, the coercivity for all samples is $\mu_0 H_C = 1$ T, which can be seen in Figure 59d. Clearly, the role of

the grain boundary phase is revealed. The formation of the $Pr_6Fe_{13}Cu$ phase is the reason for high coercivity in the Pr-Fe-Cu-B system. The increasing fraction of Pr_2Fe_{17} phase when the Boron content is reduced is leading to a kink in the magnetization curve due to the decreasing $Pr_2Fe_{14}B$ fraction. However, the coercivity remains despite the soft magnetic Pr_2Fe_{17}.

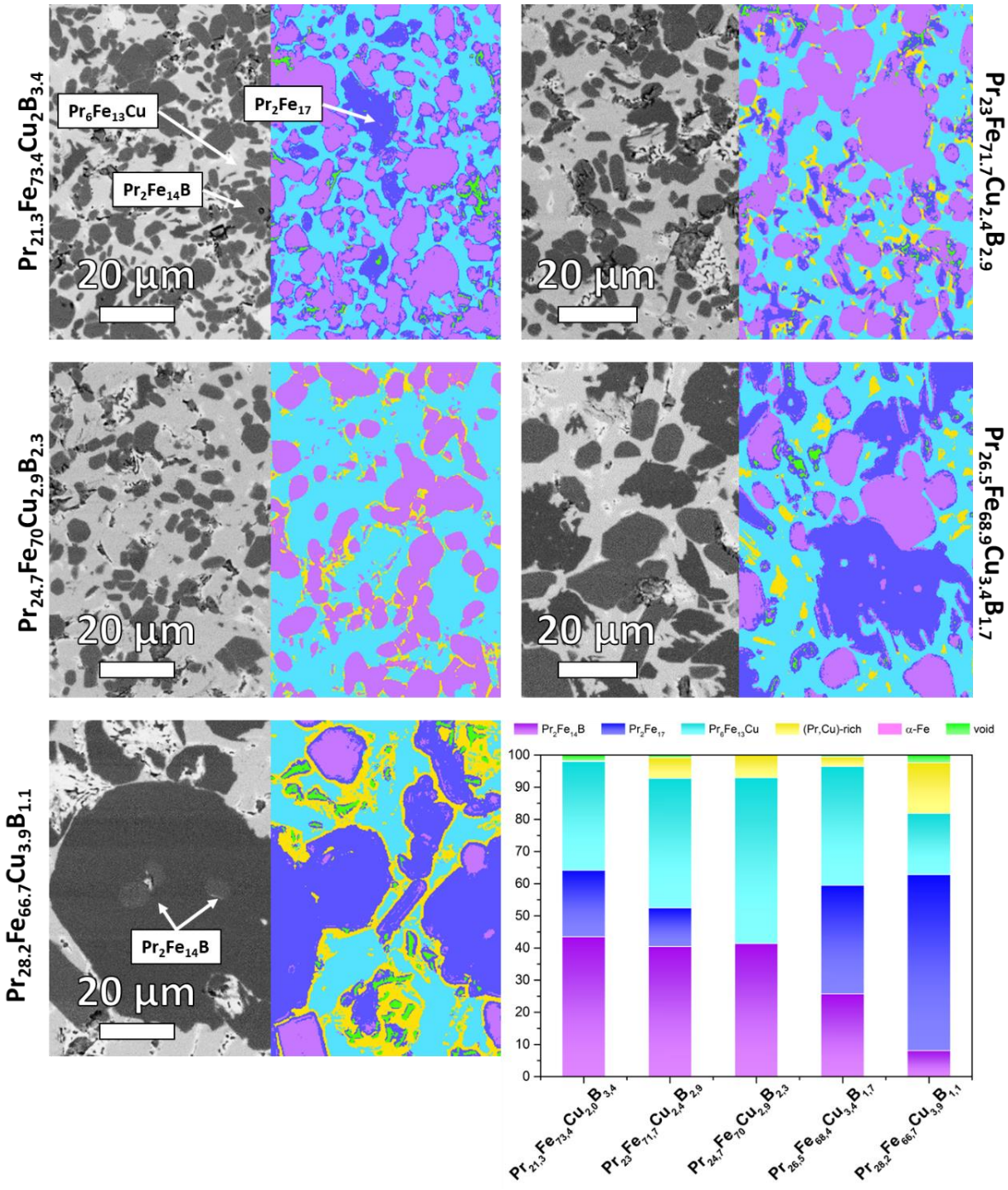

Figure 58: Further optimization approaches was done by mixtures of $Pr_6Fe_{13}Cu$ and $Pr_2Fe_{14}B$ phase. The images show grains of $Pr_2Fe_{14}B$ phase embedded and well separated by the $Pr_6Fe_{13}Cu$ phase. The fraction of $Pr_6Fe_{13}Cu$ phase is much higher compared to the previous sample series. All phase fractions from the image analysis are given in the bar chart.

The phase fractions obtained from the SEM-BSE analysis by segmentation is shown in the bar charts of the corresponding SEM-BSE images. The variation in magnetization at a measurement field of 3 T can be explained by the large fraction of secondary phases, especially the $Pr_6Fe_{13}Cu$.

High magnetization is found for samples with large fraction of $Pr_2Fe_{14}B$ phase, however, the coercivity does not follow this trend. The reason for high coercivity is not very obvious. From the idealized view on the coercivity mechanism in commercial (Nd,Pr)-Fe-B magnets, a low coercivity for large amounts of soft magnetic phases would be expected. However, despite large fraction of soft magnetic Pr_2Fe_{17} phase, high coercivity could be obtained. The reason seems to be the formation of the intermetallic $Pr_6Fe_{13}Cu$ phase. Samples with large fraction of this phase also possess high coercivity even with extensive amount of Pr_2Fe_{17} phase. The mechanism is based on a magnetic decoupling and separation, as well as an isolation of the hard magnetic $Pr_2Fe_{14}B$ grains. Especially the sample series of the mixtures between $Pr_6Fe_{13}Cu$ and $Pr_2Fe_{14}B$ indicate the importance of $Pr_6Fe_{13}Cu$ for high coercivity. All samples show a coercivity of $\mu_0 H_C$ = 1 T despite the presence of Pr_2Fe_{17}. The only exception in this series is sample 5 with a mixture of 80 % $Pr_6Fe_{13}Cu$ and 20 % $Pr_2Fe_{14}B$, which shows a major fraction of Pr_2Fe_{17} and therefore very low coercivity.

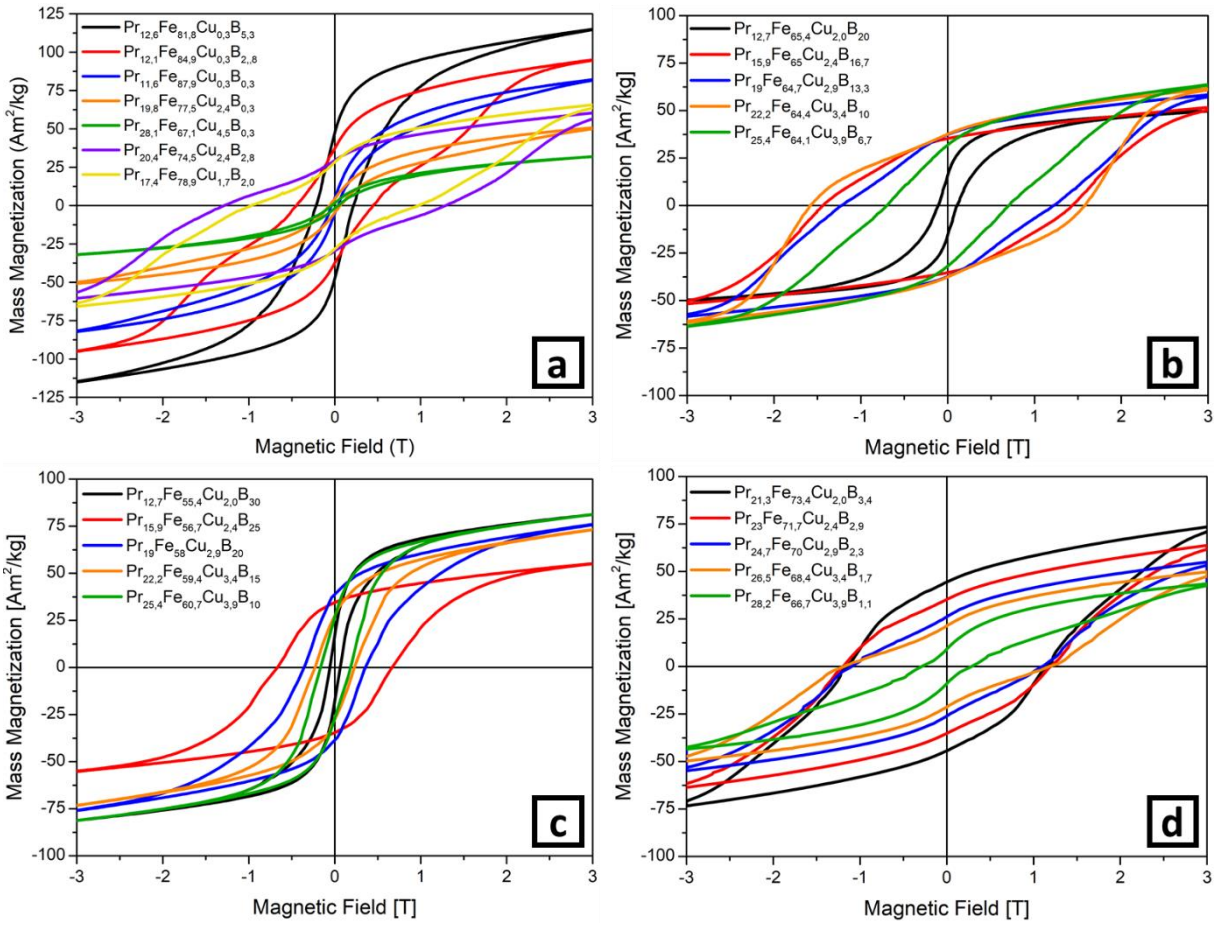

Figure 59: Hysteresis of the a) samples from the quasi-ternary phase diagram b) the mixtures of $Pr_6Fe_{13}Cu$ and FeB c) the mixtures of $Pr_6Fe_{13}Cu$ and Fe_2B and d) the mixtures of $Pr_6Fe_{13}Cu$ and $Pr_2Fe_{14}B$. Highest coercivity of $\mu_0 H_C$ = 1.6 T was achieved for the sample series in b) by mixing $Pr_6Fe_{13}Cu$ and FeB.

In conclusion, the Pr-Fe-Cu-B system allows to obtain high coercivity (up to $\mu_0 H_C$ = 1.6 T) for suction cast samples combined with a subsequent annealing treatment. The formation of a $Pr_6Fe_{13}Cu$ intermetallic phase and a high phase fraction seems to correlate with the increase in coercivity. As shown in Figure 60a), the coercivity in the quasi-ternary phase diagram increases with high amount of $Pr_6Fe_{13}Cu$, which leads to low magnetization due to dilution of the hard magnetic and high magnetization $Pr_2Fe_{14}B$ phase, as shown in Figure 60b). Further experiments based on mixtures between $Pr_6Fe_{13}Cu$ and FeB, Fe_2B and $Pr_2Fe_{14}B$ revealed that the formation

of the $Pr_6Fe_{13}Cu$ matrix and hard magnetic $Pr_2Fe_{14}B$ grains is an important feature for high coercivity. Especially within the series based on $Pr_6Fe_{13}Cu$ and $Pr_2Fe_{14}B$, high coercivity of $\mu_0 H_C = 1.2$ T could be maintained due to the large fraction of $Pr_6Fe_{13}Cu$. Within this series, the decrease in magnetization is a result of depletion in Boron and subsequently low phase fraction of the $Pr_2Fe_{14}B$ phase. However, it could be demonstrated that high coercivity does not depend on the $Pr_6Fe_{13}Cu$ phase formation but generally on the formation of a thick grain boundary, which can be seen in the sample series based on the mixture of $Pr_6Fe_{13}Cu$ and FeB. Although there is no $Pr_6Fe_{13}Cu$ observed, the coercivity is high due to the Nd-rich grain boundary and a decoupling of the hard magnetic grains. As a conclusion within this work, a beneficial effect on the coercivity by the formation of the $Pr_6Fe_{13}Cu$ phase is shown. However, a necessity for the formation of this phase cannot be concluded.

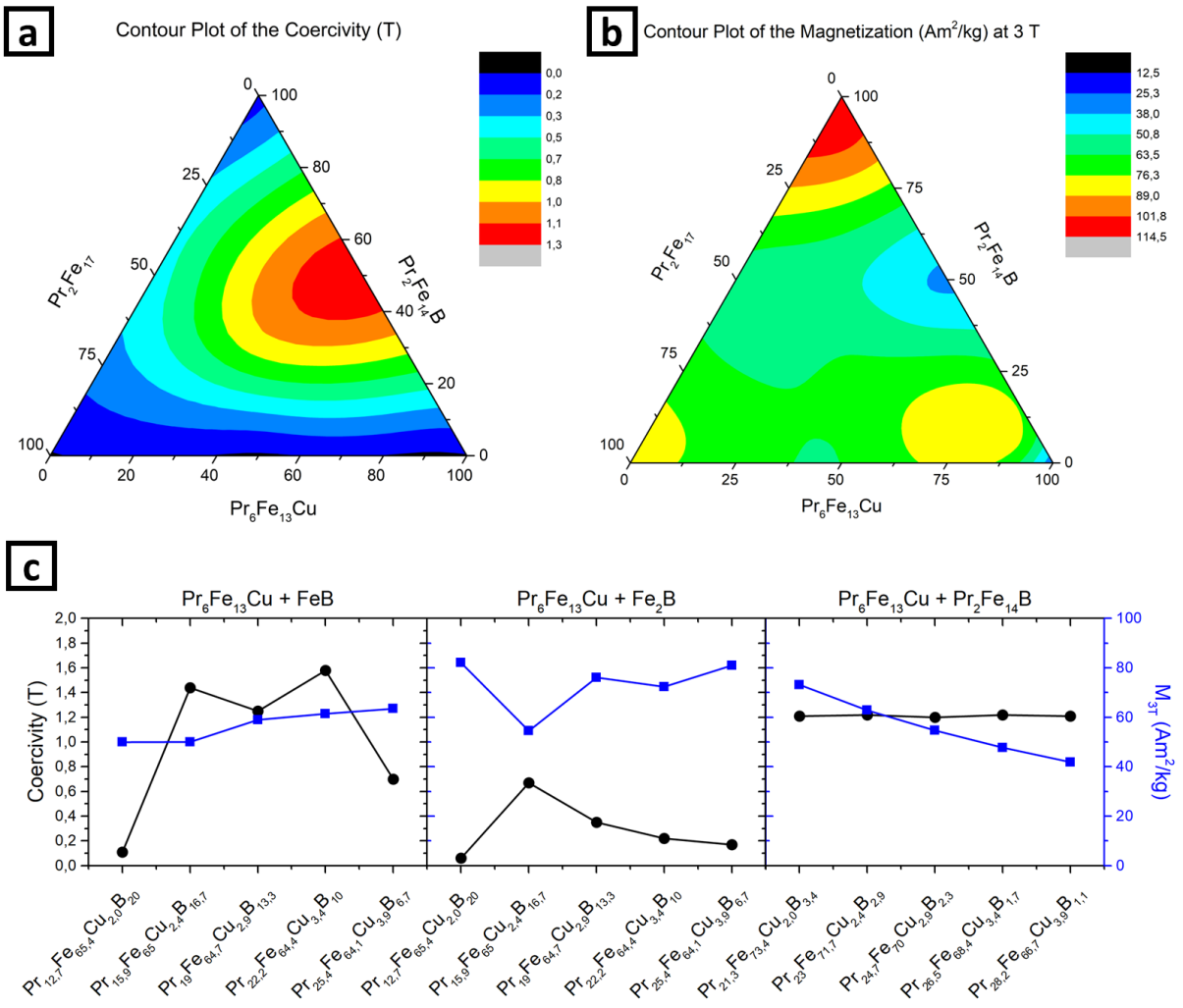

Figure 60: Summary of the observed magnetic properties in form of a contour plot in the quasi-ternary phase diagram for a) coercivity and b) magnetization at an external field of 3 T. The coercivity and magnetization at 3T for the mixtures of $Pr_6Fe_{13}Cu$ are shown in c).

5.3. Optimization and Qualification of Pr-Fe-Cu-B towards Additive Manufacturing

The following chapter contains data and figures which have been published in [135].

The systematic study based on a quasi-ternary phase diagram has shown, that it is possible to achieve coercivity in bulk samples of Pr-Fe-Cu-B by heat treatments. The SEM-BSE and EDX measurements indicate, that the formation of Pr_2Fe_{17} is difficult to avoid since it is very stable

in this part of the phase diagram. However, coercivity can be obtained although the Pr_2Fe_{17} is present. The most important feature seems to be the formation of an intergranular phase and/or $Pr_6Fe_{13}Cu$ phase which separates the $Pr_2Fe_{14}B$ phase. In fact, all samples with high coercivity show the occurrence of a pronounced grain boundary region. In order to compare the results of this work into the context of existing literature, the following overview table is shown:

Table 5: Comparison between Pr-Fe-Cu-B samples regarding composition, preparation and obtained coercivity.

Composition in at %							
Pr	**Fe**	**Cu**	**B**	**preparation**	**annealing**	**μ_0H_C [T]**	**Ref.**
37.2	44.4	3.4	15	suction cast	1000 °C - 3h 500 °C - 5h	1.5	this work Figure 56, 4
21.3	**73.4**	**2**	**3.4**	**suction cast**	**1000 °C - 3h** **500 °C - 5h**	**1.2**	**this work** **Figure 58, 1**
20.55	73.8	2	3.7	hot deformation	1000 °C - 3h 500 °C - 5h	1.85	Marcondes et al. [21]
17	76.5	1.5	5	cast	900 - 1100 °C 600 - 750 °C	0.8	Hadjipanayis et al.[22]
17	76.5	1.5	5	cast	1000 °C - 24h	0.75	Shimoda et al. [27]
17	76.5	1.5	5	hot compaction	1000 °C - 24h	1	Shimoda et al. [27]
17	76.5	1.5	5	hot rolling	1000 °C - 24h	1	Shimoda et al. [27]
17	76	1.5	5.5	hot compaction	1000 °C - 10h 500 °C - 2h	1.4	Kajitani et al. [20]

The first obvious observation is that independent of the composition and the preparation method, a high temperature annealing is necessary to develop full coercivity. The chosen temperature at 1000 °C is similar to sintering temperatures of Nd-Fe-B magnets and corresponds to the phase region of hard magnetic $Pr_2Fe_{14}B$ and liquid phase. In the case of the Pr-rich and B-lean compositions shown here, additional binary Pr_2Fe_{17} phase is forming which is found in samples from this work and in literature. However, the reason for the high temperature annealing is the reduction of soft magnetic α-Fe which increases coercivity. Some of the works indicate that the high temperature annealing is sufficient to develop high coercivity up to μ_0H_C = 1 T. However, highest coercivity is only achieved by a subsequent annealing at 500 °C. The reason seems to be the formation of intermetallic $Pr_6Fe_{13}Cu$ phase which agrees with the existing literature. In fact, based on the systematic study in the quasi-ternary phase diagram a composition with high coercivity of μ_0H_C = 1.2 T and reasonable Pr-content could be pointed

out: $Pr_{21.2}Fe_{73.4}Cu_2B_{3.4}$. This composition is almost the same as in the work of Marcondes et al. [21] and shows lower coercivity due to the missing hot deformation step. Seemingly, this region in the phase diagram shows promising coercivity, no discontinuity in the demagnetization curve and relatively high magnetization which relies on the annealing treatment and the associated formation of $Pr_6Fe_{13}Cu$ phase, minimum fraction of Pr_2Fe_{17} phase and well separated hard magnetic $Pr_2Fe_{14}B$ grains.

Regarding the consolidation by PBF-LB, high coercivity can be expected for the chosen composition of $Pr_{21}Fe_{73.5}Cu_2B_{3.5}$. It is known that the local melting by laser and fast solidification can lead to a fine microstructure of printed samples. The effect of the initial microstructure before the annealing treatment on the resulting coercivity after heat treatment is shown by comparing samples of the $Pr_{21}Fe_{73.5}Cu_2B_{3.5}$ composition prepared in as-cast condition (induction melting, large grain size) and after suction casting.

The corresponding SEM-BSE images and magnetic hysteresis of the as-cast samples are shown in Figure 61. In order to demonstrate that the Pr-Fe-Cu-B system shows higher coercivity than the Nd-based composition, the respective samples are shown in direct comparison. In as-cast state, both compositions show the occurrence of α-Fe phase, hard magnetic $(Pr,Nd)_2Fe_{14}B$ and a RE,Cu-rich grain boundary phase. The α-Fe phase does not show a dendritic shape as it would be expected for the primary solidification product. The slow cooling rate in the induction furnace and ceramic crucible can be the reason for an “in-situ” annealing. It is evident, that despite the same melting procedure, the grain size of the Pr-based sample is much lower compared to the Nd-based sample. After the annealing treatment (1000 °C for 5 hours followed by 500 °C for 3 hours) both samples show platelet shaped grains of $(Pr,Nd)_2Fe_{14}B$, the $(Pr,Nd)_2Fe_{17}$ phase and a matrix of metallic RE,Cu-rich phase together with intermetallic $(Pr,Nd)_6Fe_{13}Cu$. Besides the smaller grain size of the Pr-based samples, another important feature is observed. The $Pr_2Fe_{14}B$ grains are well separated by a continuous matrix of the $Pr_6Fe_{13}Cu$ phase. This indicates that a magnetic decoupling and reduction of surface defects can explain the high coercivity in this alloy. The $Nd_2Fe_{14}B$ grains in the corresponding Nd-based sample are in direct contact with each other and/ or with the Nd_2Fe_{17} phase. The formation of a $Nd_6Fe_{13}Cu$ phase and matrix is less pronounced. The achieved coercivity of $\mu_0H_C = 0.25$ T is only half of the corresponding Pr-based sample with $\mu_0H_C = 0.5$ T. Both, the difference in grain size and insufficient decoupling of the hard magnetic grains can explain the noticeable difference in coercivity.

Further evaluation of the magnetic properties has been done by preparing single crystals of the $(Pr,Nd)_6Fe_{13}Cu$ phase. The crystals have been prepared by liquid flux method. Alloys with the composition $Nd_{42}Fe_{54}Cu_4$ and $Pr_{42}Fe_{54}Cu_4$ were prepared by induction melting under protective Argon atmosphere. The ingots were placed in zirconia crucibles and sealed in quartz ampules under Argon atmosphere. The heat treatment consisted of (i) heating to 1350 °C for 5 min, (ii) cooling with 1 K/min to 1000 °C, and (iii) dwelling at 1000 °C for five days, (iv) cooling to 500 °C with a rate of 300 K/h, and (v) annealing for one week with subsequent quenching in water. The composition of the extracted crystals was determined by EDX. Magnetization curves of the single crystals are shown in Figure 61e and 2f, respectively. The single crystals exhibit weak magnetic behavior with magnetic susceptibility $\chi = 27 \times 10^{-5}$ m^3/kg for $Nd_6Fe_{13}Cu$ and $\chi = 25 \times 10^{-5}$ m^3/kg for $Pr_6Fe_{13}Cu$. With decreasing temperature, the magnetic susceptibility gradually increases. This reinforces the common understanding of Nd–Fe–B magnets, that the hard magnetic 2:14:1 grains need to be separated and magnetically decoupled by a non-ferromagnetic intergranular phase.

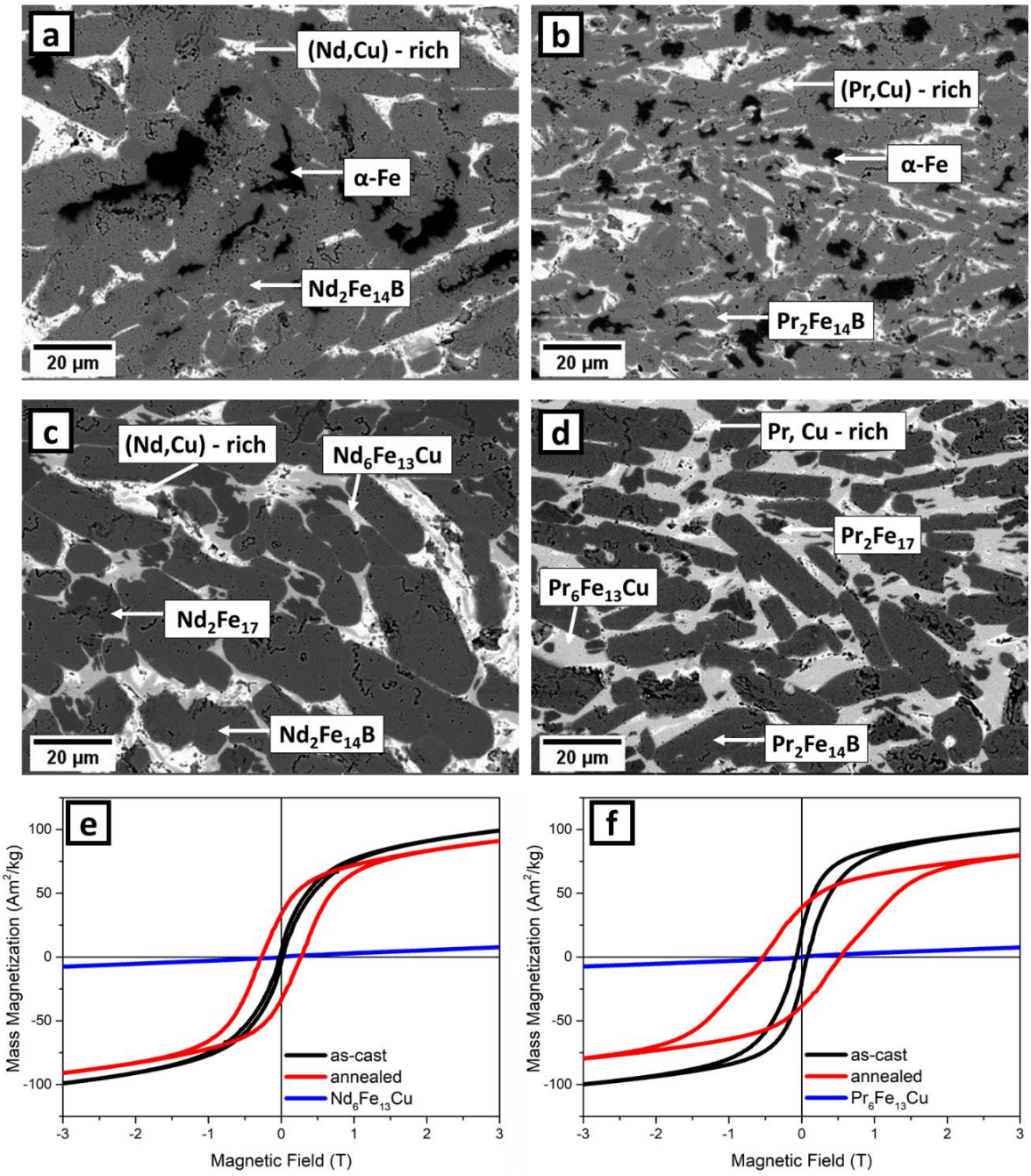

Figure 61: SEM-BSE images of the $(Pr,Nd)_{21}Fe_{73.5}Cu_2B_{3.5}$ composition. In comparison, the Pr-based (a) and Nd-based (b) compounds are shown in as-cast and annealed state together with their magnetic properties. Higher coercivity is reached for the Pr-based system. However, the standard casting by induction melting leads to large grains and lower coercivity compared to the previous optimization experiments.

Obviously, the initial microstructure and grain size does affect the microstructure after annealing and therefore the coercivity. The local melting and solidification during PBF-LB leads to very fine microstructures with cooling rates in the order of 10^3-10^4 K/s. To qualify and test material for the use in PBF-LB, suction casting with less than 10 g of the material can be used to achieve similar microstructures. This techniques allows to reach cooling rates in the order of 10^3 K/s [143]–[145] or even higher depending on the geometry of the die. The SEM-BSE images and magnetic hysteresis of the suction cast and annealed samples is shown in Figure 62. As observed in the cast samples, the suction cast microstructure consists of dendritic α-Fe, $(Pr,Nd)_2Fe_{14}B$ and a RE,Cu-rich grain boundary phase. Both samples are soft magnetic in the

suction cast state. After the annealing treatment, the microstructure shows the formation of $(Pr,Nd)_2Fe_{14}B$, the $(Pr,Nd)_2Fe_{17}$ phase and a matrix of metallic RE,Cu-rich phase together with intermetallic $(Pr,Nd)_6Fe_{13}Cu$ which is consistent with the previous experiments. Both samples show a significant increase in coercivity, in fact, twice as high as in the cast state. However, the Nd-based sample does only reach $\mu_0 H_C = 0.5$ T, half of the coercivity achieved in the Pr-based samples. Although the $Nd_2Fe_{14}B$ seem to be well separated by the $Nd_6Fe_{13}Cu$ phase, the grain size of the Pr-based sample is much higher, thus possess higher coercivity of $\mu_0 H_C = 1$ T. Based on the suction cast experiments, it could be shown that the use of $Pr_{21}Fe_{73.5}Cu_2B_{3.5}$ for PBF-LB will lead to an expected coercivity of $\mu_0 H_C = 1$ T.

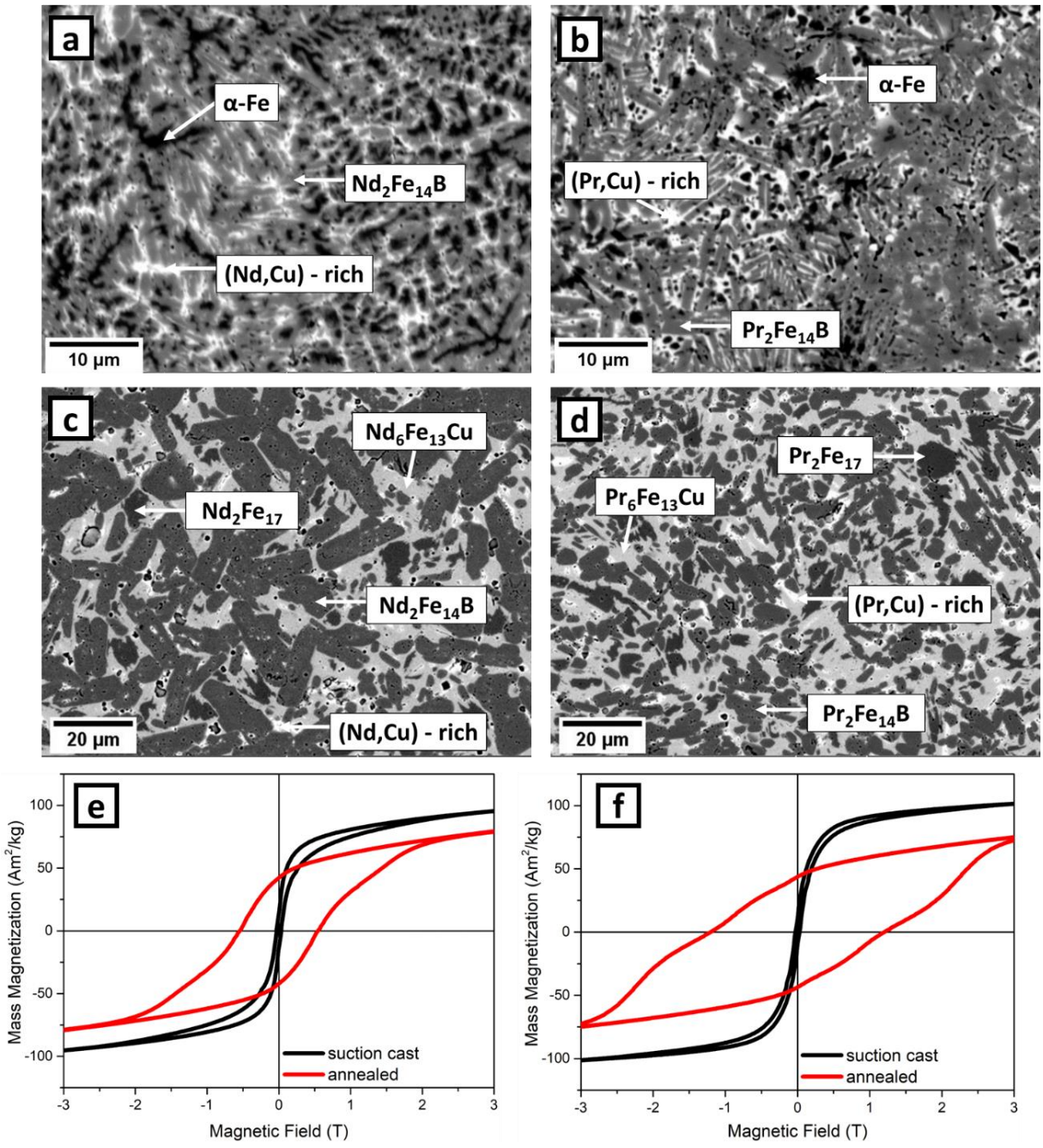

Figure 62: SEM-BSE images of the suction cast and annealed samples of $Pr_{21}Fe_{73.5}Cu_2B_{3.5}$ composition for Pr-based (a) and Nd-based (b) samples. The coercivity does not reach the expected values which indicates that the upscaling of the material was not successful. Oxidation or RE evaporation could be the reason for lower coercivity after the annealing.

5.4. High Coercivity in Pr-Fe-Cu-B Alloys for Additive Manufacturing

Additive Manufacturing of intermetallic, hard magnetic materials is certainly not a trivial task. As it is reported in literature and observed in this work, careful design of the alloy and optimized processing are requirements to achieve highest performance. The use of PBF-LB is a relatively new production technique and much different from the powder metallurgical routes for Nd-Fe-B based magnets. The most important difference is the re-melting of the powder, local and uncontrolled solidification and resulting appearance/ disappearance of undesired/ desired microstructural features which decide about the coercivity. It is commonly accepted that the microstructure of commercial Nd-Fe-B sintered magnets is close to the "ideal" and consists of single crystalline $Nd_2Fe_{14}B$ grains (usually of 2-10 μm size) surrounded by a continuous layer of Nd-rich phase with a thickness of only a few nanometers resulting in a strong nucleation-type coercivity. At the same time, the PBF-LB printed Nd-Fe-B-based alloys consist of a very fine, dendritic microstructure where the solidification and phase distribution cannot be easily controlled. In this regard, the investigations and observations based on a quasi-ternary phase diagram formed by Pr_2Fe_{17}, $Pr_2Fe_{14}B$ and the $Pr_6Fe_{13}Cu$ phase have revealed the high coercivity in bulk material by annealing treatment in Pr-Fe-Cu-B alloys can be realized, almost independent from the prior consolidation method. A high temperature annealing, for several hours, leads to the formation of the hard magnetic $Pr_2Fe_{14}B$ phase. The former microstructural features have completely vanished. After a low temperature annealing, again for several hours, the $Pr_6Fe_{13}Cu$ phase is forming which is accompanied by a severe increase in coercivity. The magnetic hardening effect seems to be well suited to realize hard magnetic samples by PBF-LB. Therefore, material with $Pr_{21}Fe_{73.5}Cu_2B_{3.5}$ has been prepared for PBF-LB experiments.

Ideally, a spherical, atomized powder is preferably used during Additive Manufacturing. However, devices for this purpose (on lab-scale and commercially) are not easily accessible. Therefore, a large induction melting device at IWKS facility has been used since the batch sizes on lab scale are limited up to 30 g. Consequently, the experiments are based on non-spherical, mechanically milled powder. An empirical observation based on preliminary experiments was that the grinding process is challenging due to the high, ductile Pr content and α-Fe phase in as cast condition. Therefore, the cast ingots were hydrogen decrepitated at 10 bar H_2 pressure and room temperature. For the milling in the large-scale experiment, a pin-mill (Hosokawa Alpine Picoline®) was used. Afterwards, the powder was annealed under dynamic vacuum for two hours at 600 °C to desorb the hydrogen (de-hydrogenation).

The images and particle size analysis of the prepared powder for PBF-LB are shown in Figure 63. Based on SEM-BSE images as seen in Figure 63a), the particles are separated, labeled and the size was quantified by image analysis. By using 5 to 10 images with <100 particles, it was assured to have a sufficient statistic. The corresponding histogram is shown in Figure 63c) which represents the counted particles weighted by the area fraction over the corresponding Feret (or caliper) diameter. The optical inspection of the particles reveals the non-spherical, quite irregular shape. Although most of the particles seem to be rather equiaxed, some particles with high aspect ratio are observed. Furthermore, very fine particles cannot be avoided by the sieving process. The shown powder represents the size fraction which was used for the PBF-LB experiments. Sieves of 63 μm and 20 μm mesh size were used. However, the size distribution shows that the average size of the powder with ~20 μm is much larger than expected and the largest fraction of the powder is smaller than the mesh size of 20 μm. The reason can be that the sieving was not sufficient and/or the formation of agglomerates which behave like large particles but, in fact, consist of much smaller particles.

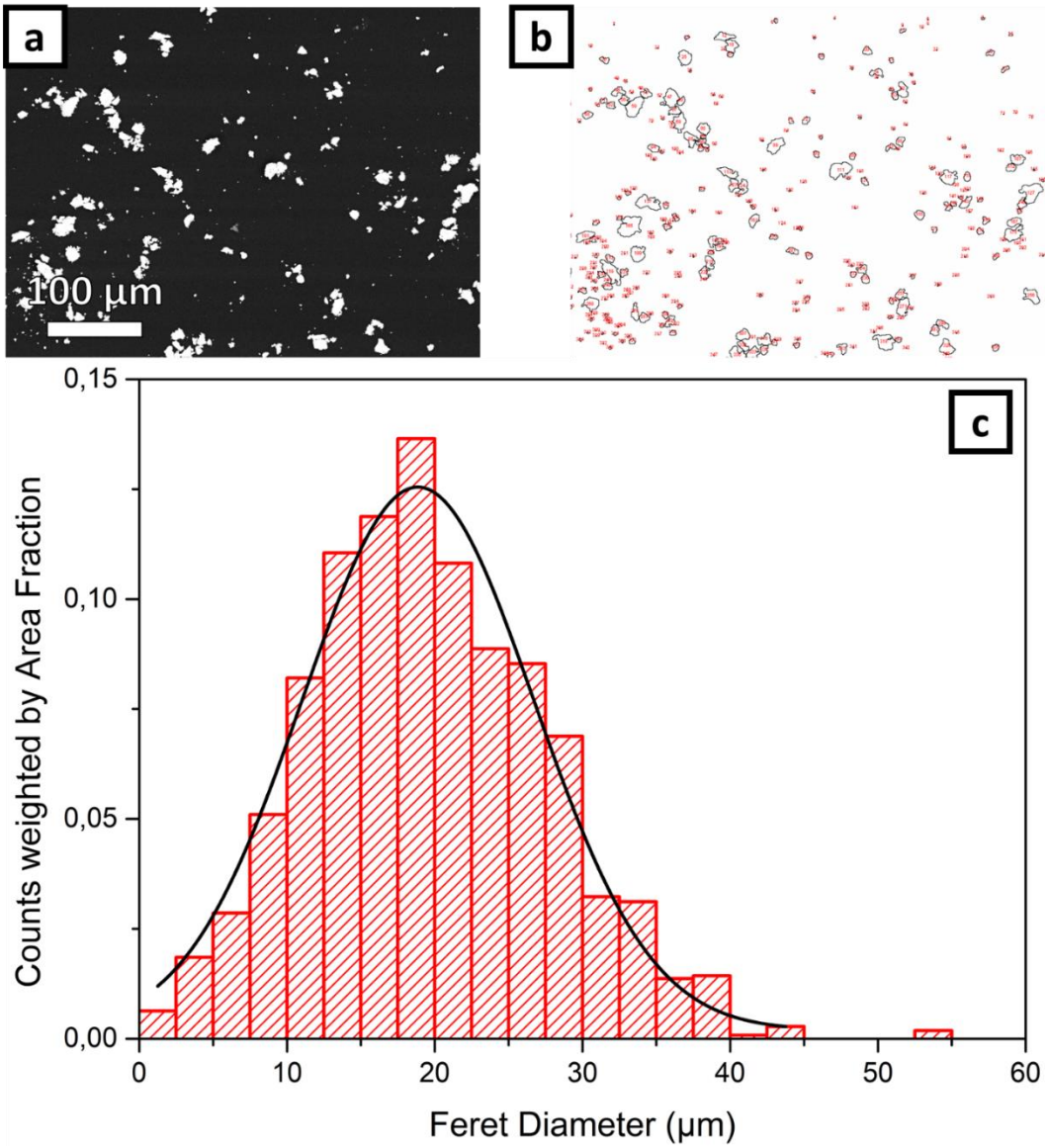

Figure 63: The images show examples of a) the SEM-BSE image of the powder particles of the optimized Pr-Fe-Cu-B alloy for PBF-LB experiments and b) the corresponding image processing to quantify the Feret Diameter which is shown in c) in form of a histogram. Although the powders have been sieved by a 63 µm mesh size, the average diameter is much smaller.

At first, the PBF-LB processing window was investigated by consolidation of 3 layers of the prepared powder. For these tests, the powder was applied manually. The laser power was varied between 50, 100, 150 and 195 W together with a variation in scanning speeds between 500, 1000, 1500, 2000, 2500 and 3000 m/s resulting in 24 parameter sets. The hatch distance was kept at 60 μm for all experiments. The rectangular printed samples are shown in Figure 64a. Low laser power and high scan speeds resulted in unmolten areas, whereas higher energy input by high laser power and low scan speeds led to balling effect. The best parameter region with a homogeneous melting of the powder and surface quality was found for a laser power of 195 W and a laser speed between 1500 and 2000 mm/s. For the printing of multiple layers, the same parameters were used, however the scan speed was varied between 1500 and 2000 mm/s. Since the powder was applied automatically by a brush, the layer thickness was fixed to 50 μm.

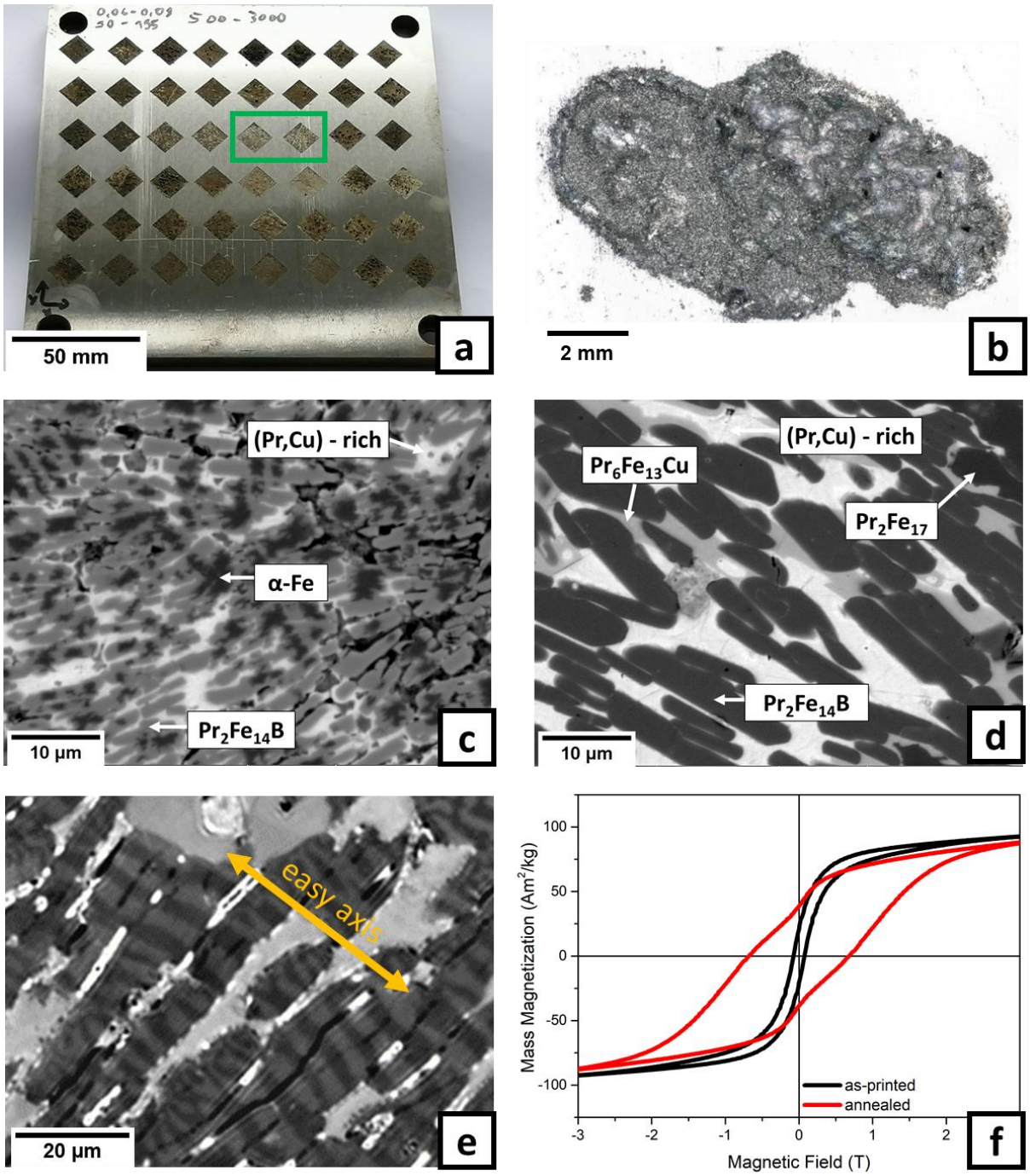

Figure 64: a) the optimization of the PBF-LB parameter space with the optimal setting marked in green, b) PBF-LB printed bodies with the intended position and shape in blue and the shift and overlap of subsequent layers due to a collision with the blade, c) BSE microstructure after PBF-LB process, d) BSE microstructure after annealing, e) magnetic Kerr contrast of the sample after PBF-LB processing and annealing and f) hysteresis loops (room temperature) for as-printed and annealed sample.

Unfortunately, the irregular, non-ideal morphology of the powder was the reason that only one sample was printed successfully. Due to variation in the actual layer thickness, the brush collided with the consolidated layers and ripped the samples from the substrate. The sample shown in Figure 64b was printed using an optimal parameter set with laser power of 195 W, a laser speed of 2000 mm/s. As indicated in the image, the final shape was not achieved due to a collision with the brush. The microstructure in SEM-BSE contrast is shown in Figure 64c. The occurring phases and length scales are very similar to the corresponding suction cast sample.

Primary solidification product seems to be α-Fe which is surrounded by the hard magnetic $Pr_2Fe_{14}B$ phase and a Pr,Cu-rich grain boundary phase. Smaller voids are visible which can occur due to the water-based fine polishing step. However, the microstructure after the annealing (Figure 64d) reveals the formation of platelet like grains of $Pr_2Fe_{14}B$ which are embedded in a thick Pr,Cu-rich matrix together with intermetallic $Pr_6Fe_{13}Cu$.

In agreement with the previous experiments, the annealing treatment leads to a significant increase in coercivity reaching $\mu_0 H_c = 0.75$ T. Although the phases and grain size distribution are similar to the suction cast and annealed samples, the high coercivity of $\mu_0 H_c = 1.2$ T could not be reproduced after PBF-LB. The observed difference can be associated with the necessity of optimization of each individual step along the processing chain. It has to be mentioned that the high aspect ratio of the $Pr_2Fe_{14}B$ grains indicates the preferred growth along certain crystallographic directions. Additional Kerr microscopy (Figure 64e) showing the domain patterns of the $Pr_2Fe_{14}B$ grains reveal that the magnetic hard c-axis lies perpendicular to the long grain axis, meaning the preferred growth of the a-b crystal plane. Seemingly, the directional solidification can be used to produce texture magnets by Additive Manufacturing. Controlled thermal gradients between the melt and substrate plate can be utilized to achieve columnar growth and a high degree of texture. In fact, subsequent work by Goll et al. [142] on the same alloy composition could show, that a 26 % higher remanence compared to the cast material could be achieved, which is denoted to the thermal gradient during PBF-LB.

6. Summary of the work and Outlook

Novel (Pr,Nd)-Fe-B based material systems have been investigated and tested for the purpose of producing permanent magnets by Laser-Powder-Bed-Fusion (PBF-LB). The goal of this work was to explore a specific alloy modification to induce solid-state transformations which lead to magnetic hardening independent of the uncontrolled solidification during PBF-LB. Following the synthesis and characterization on lab-scale, promising compositions were upscaled and tested within the PBF-LB process.

6.1. High Coercivity in Pr-Fe-Cu-B Alloys

The first alloy system is based on the hard magnetic properties of Pr-Fe-Cu-B alloys. After optimization of the composition regarding the coercivity, mechanically milled powder was printed by PBF-LB. In as-printed state, the samples are soft magnetic, only reaching a coercivity of less than $\mu_0 H_C = 0.2$ T. It has been shown that the subsequent annealing treatments are necessary to develop the hard magnetic properties. In as-cast condition, the samples show the occurrence of a complex microstructure with soft magnetic α-Fe, Pr_2Fe_{17} intergranular Pr-Cu eutectic and the minor fraction of hard magnetic $Pr_2Fe_{14}B$. A high temperature annealing at 1000 °C is necessary to reduce the amount of α-Fe phase but only the low temperature annealing at 500 °C develops full coercivity. The reason is based on the formation of a $Pr_6Fe_{13}Cu$ phase. Single crystals of the respective phase have shown a weak magnetic nature. The decoupling and separation of the hard magnetic $Pr_2Fe_{14}B$ during the formation of the intergranular phase is believed to be the reason for the coercivity up to $\mu_0 H_C = 1.2$ T. Most importantly, the magnetic properties translate to the printed samples reaching $\mu_0 H_C = 0.75$ T. The respective samples cannot be distinguished from as-cast material after the annealing treatment, indicating that only the heat treatment is responsible for magnetic hardening. Further optimization of the alloy composition and applied temperatures can result in a reduction of secondary phases and increase the saturation magnetization, finally leading to higher remanence. In addition, the microstructure of PBF-LB samples revealed the possibility to realize a high degree of texture by controlled thermal gradients during the processing. In summary, the achieved magnetic properties of the investigated Pr-Fe-Cu-B material system are promising to realize additive manufactured permanent magnets with competitive magnetic properties and BH_{max}.

6.2. Magnetic Hardening in Nd-Fe-Co-TM-Cu-B Alloys

Further systematic work on the formation and transformation of a metastable $Nd_2(Fe,Co)_{17}B_x$ phase has shown the possibility for a novel magnetic hardening effect. At first, systematic alloy modification showed that elements such as Co, Cu and Type II dopants such as Mo and Nb are necessary to 1) stabilize the metastable phase and 2) to provoke the formation of intermetallic precipitates. This mechanism led to coercivity of almost $\mu_0 H_C = 1$ T for bulk samples. Independent from the goal of 3D printed magnets, the novel magnetic hardening mechanism is interesting for the commercial production of Nd-Fe-B magnets and improving coercivity. The realization of a metastable phase and microstructure which can be transformed by subsequent heat (or hydrogen) treatment can be adapted in the powder metallurgical production processes.

However, the printed samples of the same composition did not show the expected coercivity values. Inhomogeneous microstructure, RE depletion and insufficient densification seem to be the reason for low coercivity in as-print and annealed state. Independent of the AM processing, the formation and transformation based on the metastable phase is a novel approach to

magnetic hardening of Nd-Fe-B magnets. In the context of this work, the “magnetic hardening” refers to the enhancement and optimization of the coercivity of a magnet. In general, this can be obtained by different approaches for example by heat treatments such as the “post-sinter-annealing” for sintered Nd-Fe-B or the grain refinement of the hard magnetic $Nd_2Fe_{14}B$ phase. However, the “magnetic hardening” does not indicate the “coercivity mechanism” which can be very different depending on the material system. In a simplified view, the coercivity can be dominated by the nucleation of reverse magnetic domains and unimpeded domain wall propagation within the grain or by the domain wall pinning on chemical gradients, secondary phases and precipitates.

The reported magnetic hardening effect could allow to decrease the grain size below the state-of-the art of sintered and hot deformed magnets. The grain refinement is based on segregation of the elements Cu and Mo, which are solved in the metastable phase but not the hard magnetic $Nd_2(Fe,Co)_{14}B$ which could be shown by elemental mapping of the respective samples. Optimizing the composition and annealing treatment can improve the coercivity of the magnets substantially.

6.3. Technical Relevance of Additive Manufactured Permanent Magnets

Besides the problem of low coercivity and controlling the microstructure, the Additive Manufacturing route bares more fundamental, practical problems. The powder production is the first task to consider. In this work, non-spherical powders with insufficient flowability have been used. The flowability is affected by the arbitrary shape of the powder particles but also the particle size distribution. Due to static and magnetic adhesive forces, it is difficult to separate the fine particles and satellites which do not only decrease the flowability but show high reactivity and oxygen pick-up. Ideally, spherical powder by atomization or spheroidization techniques should be used to increase the printability and careful sifting of the powders prevent the risks of fine particles is necessary.

The consolidated samples by laser powder bed fusion have shown a very narrow processing region for Nd-Fe-B based material. In this work, the optimization of the process parameters was based on 1D line scans, followed by 2D area scans and finally the 3D printing of volumes, which are always necessary for new materials. However, achieving fully dense and true-to-shape bodies is a challenging task which is not only based on the printability of the powder but the evaporation of RE elements due to their low vapor pressure and crack formation due to their inelastic mechanical properties. To overcome this problem and improve the densification, a heated substrate plate would allow to decrease the temperature difference between melt and already solidified material and prevent the formation of cracks due to residual stresses. Furthermore, the use of similar material as a substrate plate was found to be beneficial on the crack formation during the experimental work. From this finding, it becomes apparent that print-in designs and compositional gradients in printed magnetic components will be a challenge and reveal several unexplored problems.

Although the elemental modifications and alloys presented in this work show interesting and novel features of achieving hard magnetic properties, the obtained values of the printed samples in this work are still incomparable to the state-of-the art magnet production. Besides the low coercivity, all samples are isotropic and have low magnetization due to high element additions. The $(BH)_{max}$ is much lower than conventional hot deformed or sintered magnets. Even if the

properties would be comparable and competing with today's magnets, in its current state, it is difficult to consider Additive Manufacturing as a replacement for existing and established production techniques.

Regarding the production chain of magnets, it becomes apparent that the phase from RE-oxides to the powder production is the same and has the same environmental impact and loss in material. The difference and advantage of Additive Manufacturing manifests in the magnet production and application. Additive Manufacturing is considered to be resource efficient due to net-shape fabrication (which would avoid post-processing steps) and no loss of material during production. Furthermore, the complex geometries are the basis for new application possibilities. Print-in designs and specific magnetic stray field could be realized only by AM. However, this leads to an apparent problem, the recycling of magnets. Mixture of components from different materials would complicate the disintegration and refurbishment and, contrary to the promised advantages, impair the environmental impact. In summary, permanent magnet production by Additive Manufacturing is distinguished from conventional production methods by its high geometrical freedom. If the magnetic properties of optimized alloys reach comparable properties, such magnets would occupy a niche market focused on applications that require specific and complex prerequisites in geometry and stray field.

6.4. Concluding Remarks and Suggestions to Further Research

The materials under investigation show interesting microstructural effects leading to magnetic hardening. The elemental modifications are the reason for the formation of metastable phases and secondary intergranular, intermetallic phases. These microstructures are fundamentally new and go beyond conventional production of permanent magnets and indicate that the existing assumptions for ideal microstructures in Nd-Fe-B magnets need to be critically reconsidered. Both the Pr-Fe-Cu-B and Nd-Fe-Co-Mo-Cu-B alloys under investigation have shown the formation of large quantities of secondary intermetallic phases which are considered to be non-beneficial for coercivity of magnets. However, this study reveals that such microstructures can reach coercivities of $\mu_0 H_C = 1$ T or higher and the formation of secondary phases is necessary to develop hard magnetic properties in bulk material. Incorporating these results into existing powder metallurgical production chains could allow to increase the coercivity of Nd-Fe-B magnets even higher towards the expected theoretical limit. Especially the use of a magnetic hardening by utilizing the formation of a metastable $Nd_2Fe_{17}B_X$ phase has not been shown prior to this work. The magnetic hardening is connected to the formation of paramagnetic precipitates which do not seem to affect the nucleation-based coercivity mechanism commonly found in sintered Nd-Fe-B magnets. Further research on the formation of precipitates with ferro-, ferri- or antiferromagnetic ordering could allow to achieve nano-composite magnets with remanence enhancement and/ or increased coercivity by pinning of domain wall motion.

The Additive Manufacturing of Nd-Fe-B based material has shown the necessity for further systematic studies on the microstructure formation and careful process monitoring during the consolidation. In collaboration with the Institute of Production Management, Technology and Machine Tools, a methodology to qualify, test and optimize the process with less than 100 g has been established successfully. Based on this approach, reoccurring defects such as voids and crack formation and the possibility to achieve texture based on controlled thermal gradients

can and have to be investigated in the future. Especially the use of modern equipment for melt pool monitoring, such as high-speed-camera and pyrometer, together with controllable thermal gradients by a heatable building platform and laser with variable intensity profile to control the melt pool would allow to systematically investigate the process – microstructure – property relation.

7. Literature

[1] S. Bobba, S. Carrara, J. Huisman, F. Mathieux, and C. Pavel, “Critical Raw Materials for Strategic Technologies and Sectors in the EU - a Foresight Study,” 2020.

[2] European Comission, “Critical raw materials.” [Online]. Available: https://ec.europa.eu/growth/sectors/raw-materials/areas-specific-interest/critical-raw-materials_en.

[3] European Raw Materials Alliance (ERMA), “About ERMA.” [Online]. Available: https://erma.eu/.

[4] European Institute of Innovation and Technology – Raw Materials (EIT RawMaterials), “Developing raw materials into a major strength for Europe.” [Online]. Available: https://eitrawmaterials.eu/.

[5] B. J. Smith, M. E. Riddle, M. R. Earlam, C. Iloeje, and D. Diamond, “Rare Earth Permanent Magnets: Supply Chain Deep Dive Assessment,” 2022.

[6] European Raw Materials Alliance, “Rare Earth Magnets and Motors : A European Call for Action,” 2021.

[7] O. Gutfleisch, “Controlling the properties of high energy density permanent magnetic materials by different processing routes,” *J. Phys. D. Appl. Phys.*, vol. 33, no. 17, pp. R157–R172, Sep. 2000.

[8] O. Gutfleisch, M. A. Willard, E. Brück, C. H. Chen, S. G. Sankar, and J. P. Liu, “Magnetic Materials and Devices for the 21st Century: Stronger, Lighter, and More Energy Efficient,” *Adv. Mater.*, vol. 23, no. 7, pp. 821–842, Feb. 2011.

[9] K. P. Skokov and O. Gutfleisch, “Heavy rare earth free, free rare earth and rare earth free magnets - Vision and reality,” *Scr. Mater.*, vol. 154, pp. 289–294, Sep. 2018.

[10] F. Kools, A. Morel, R. Grössinger, J. M. Le Breton, and P. Tenaud, “LaCo-substituted ferrite magnets, a new class of high-grade ceramic magnets; Intrinsic and microstructural aspects,” *J. Magn. Magn. Mater.*, vol. 242–245, pp. 1270–1276, 2002.

[11] L. Zhou *et al.*, “Architecture and magnetism of alnico,” *Acta Mater.*, vol. 74, pp. 224–233, Aug. 2014.

[12] J. Cui *et al.*, “Current progress and future challenges in rare-earth-free permanent magnets,” *Acta Mater.*, vol. 158, pp. 118–137, Oct. 2018.

[13] Toyota Motor Corporation, “Toyota Develops New Magnet for Electric Motors Aiming to Reduce Use of Critical Rare-Earth Element by up to 50%,” 2018. [Online]. Available: https://global.toyota/en/newsroom/corporate/21139684.html?_ga=2.71651923.1550203226.1660290615-333381247.1660290615.

[14] I. Poenaru *et al.*, “Ce and La as substitutes for Nd in Nd2Fe14B-based melt-spun alloys and hot-deformed magnets: a comparison of structural and magnetic properties,” *J. Magn. Magn. Mater.*, vol. 478, pp. 198–205, May 2019.

[15] K. J. Merazzo *et al.*, “Magnetic materials: a journey from finding north to an exciting printed future,” *Mater. Horizons*, vol. 8, no. 10, pp. 2654–2684, 2021.

[16] V. Chaudhary, S. A. Mantri, R. V. Ramanujan, and R. Banerjee, “Additive manufacturing of magnetic materials,” *Prog. Mater. Sci.*, vol. 114, no. May, p. 100688, Oct. 2020.

[17] T. N. Lamichhane, L. Sethuraman, A. Dalagan, H. Wang, J. Keller, and M. P. Paranthaman, “Additive manufacturing of soft magnets for electrical machines—a review,” *Mater. Today Phys.*, vol. 15, p. 100255, Dec. 2020.

[18] A. Arabi-Hashemi, X. Maeder, R. Figi, C. Schreiner, S. Griffiths, and C. Leinenbach, “3D magnetic patterning in additive manufacturing via site-specific in-situ alloy modification,” *Appl. Mater. Today*, vol. 18, 2020.

[19] L. Withanawasam, Y. J. Zhang, and G. C. Hadjipanayis, “Coercivity enhancement in Pr-Fe-B magnets with small additions of Cu and Zn,” *J. Appl. Phys.*, vol. 70, no. 10, pp. 6450–6452, 1991.

[20] T. Kajitani, K. Nagayama, and T. Umeda, “Microstructure of Cu-added Pr-Fe-B magnets: Crystallization of antiferromagnetic Pr6Fe13Cu in the boundary region,” *J. Magn. Magn. Mater.*, vol. 117, no. 3, pp. 379–386, Dec. 1992.

[21] P. V. P. Marcondes and R. N. Faria, “Microstructural studies on Pr-Fe-B-Cu magnets produced by upset forging of cast ingot,” *Mater. Sci. Eng. A*, vol. 272, no. 2, pp. 245–249, 1999.

[22] G. C. Hadjipanayis, M. Zhang, and C. Gao, “High coercivities in as-cast Pr-Fe-B and Nd-Fe-B alloys with impurity additions,” *Appl. Phys. Lett.*, vol. 54, no. 18, pp. 1812–1814, May 1989.

[23] W. C. Chang *et al.*, “The magnetic properties of hot-rolled Pr/sub 17/Fe/sub 77.5/B/sub 4/M/sub 1.5/(M=Cu/Ga/Ag/Al/In/Pb) alloys,” *IEEE Trans. Magn.*, vol. 26, no. 5, pp. 2604–2606, Nov. 1990.

[24] T. Yuri and T. Ohki, “Effect of two-step annealing on magnetic properties of Pr-Fe-B base hot-rolled magnet,” *IEEE Trans. Magn.*, vol. 29, no. 6, pp. 2752–2754, Nov. 1993.

[25] N. Takahashi, H. Nakamura, C. R. Paik, S. Sugimoto, M. Okada, and M. Homma, “Coercivity and Microstructures in Pr–Fe–B–M Cast Alloys (M=Cu/Ga/Ag/Al/In/Pb),” *Mater. Trans. JIM*, vol. 32, no. 1, pp. 90–92, 1991.

[26] T. Shimoda, K. Akioka, O. Kobayashi, and T. Yamagami, “High-energy cast Pr-Fe-B magnets,” *J. Appl. Phys.*, vol. 64, no. 10, pp. 5290–5292, Nov. 1988.

[27] T. Shimoda *et al.*, “Hot-working behavior of cast Pr-Fe-B magnets,” *IEEE Trans. Magn.*, vol. 25, no. 5, pp. 4099–4104, 1989.

[28] W. F. Li, T. Ohkubo, T. Akiya, H. Kato, and K. Hono, “The role of Cu addition in the coercivity enhancement of sintered Nd-Fe-B permanent magnets,” *J. Mater. Res.*, vol. 24, no. 2, pp. 413–420, 2009.

[29] X. D. Xu *et al.*, “Comparison of coercivity and squareness in hot-deformed and sintered magnets produced from a Nd-Fe-B-Cu-Ga alloy,” *Scr. Mater.*, vol. 160, no. October, pp. 9–14, 2019.

[30] J. Gao, T. Volkmann, and D. M. Herlach, “Critical undercoolings for different primary phase formation in Nd15Fe77.5B7.5 alloy,” *IEEE Trans. Magn.*, vol. 38, no. 5 I, pp. 2910–2912, Sep. 2002.

[31] J. Strohmenger, T. Volkmann, J. Gao, and D. M. Herlach, “Metastable phase formation in undercooled Nd-Fe-B alloys investigated by in-situ diffraction using synchrotron radiation,” *Mater. Sci. Forum*, vol. 508, pp. 81–86, 2006.

[32] S. Ozawa, M. Li, S. Sugiyama, I. Jimbo, S. Hirosawa, and K. Kuribayashi, “Microstructual

evolution and magnetic properties of the Nd-Fe-B alloys solidified from undercooled melt by containerless solidification," *Mater. Sci. Eng. A*, vol. 382, no. 1–2, pp. 295–300, 2004.

[33] J. Gao, T. Volkmann, and D. M. Herlach, "Metastable phase crystallized from undercooled NdFeCoZrGaB alloy droplets," *J. Alloys Compd.*, vol. 308, no. 1–2, pp. 296–300, Aug. 2000.

[34] S. Ozawa, M. Li, S. Sugiyama, I. Jimbo, and K. Kuribayashi, "Direct crystallization of the Nd2Fe14B peritectic phase by containerless solidification in a drop tube," *Mater. Trans.*, vol. 44, no. 5, pp. 806–810, 2003.

[35] S. Ozawa, T. Saito, and T. Motegi, "Effects of cooling rate on microstructures and magnetic properties of Nd-Fe-B alloys," *J. Alloys Compd.*, vol. 363, no. 1–2, pp. 268–275, 2004.

[36] K. Kuribayashi and S. Ozawa, "Metastable phase formation from undercooled melt of Nd-Fe-B alloys," *J. Alloys Compd.*, vol. 408–412, pp. 266–272, 2006.

[37] Y. K. Zhang, J. Gao, H. Yasuda, D. M. Herlach, and J. C. He, "Does reduced fluid flow alter α-Fe content of Nd-Fe-B ingots?," *J. Alloys Compd.*, vol. 493, no. 1–2, pp. L8–L11, Mar. 2010.

[38] J. Gao, T. Volkmann, and D. M. Herlach, "Metastable solidification of NdFeB alloys by drop-tube processing," *J. Mater. Res.*, vol. 16, no. 9, pp. 2562–2567, 2001.

[39] J. Strohmenger, T. Volkmann, J. Gao, and D. M. Herlach, "The formation of a metastable peritectic phase in Nd-Fe-B alloys investigated by in situ X-ray diffraction during solidification," *Mater. Sci. Eng. A*, vol. 413–414, pp. 263–266, 2005.

[40] T. Volkmann, J. Gao, J. Strohmenger, and D. M. Herlach, "Direct crystallization of the peritectic Nd2Fe14B1 phase by undercooling of the melt," *Mater. Sci. Eng. A*, vol. 375–377, no. 1-2 SPEC. ISS., pp. 1153–1156, 2004.

[41] J. Gao, T. Volkmann, and D. M. Herlach, "Solidification of levitated Nd-Fe-B alloy droplets at significant bulk undercoolings," *J. Alloys Compd.*, vol. 350, no. 1–2, pp. 344–350, Feb. 2003.

[42] J. Gao, T. Volkmann, and D. M. Herlach, "Undercooling-dependent solidification behavior of levitated Nd14Fe79B7 alloy droplets," *Acta Mater.*, vol. 50, no. 11, pp. 3003–3012, 2002.

[43] J. Gao, T. Volkmann, J. Strohmenger, and D. M. Herlach, "Phase selection in undercooled Nd-Fe-Co-B alloy droplets," *Mater. Sci. Eng. A*, vol. 375–377, no. 1-2 SPEC. ISS., pp. 498–501, 2004.

[44] S. Ozawa, K. Kuribayashi, S. Hirosawa, S. Reutzel, and D. M. Herlach, "Heat treatment of metastable Nd2Fe17Bx phase formed from undercooled melt of Nd-Fe-B alloys," *J. Appl. Phys.*, vol. 100, no. 12, p. 123906, Dec. 2006.

[45] J. Gao and B. Wei, "Containerless solidification of undercooled NdFeZrB alloy droplets in a drop tube," *J. Alloys Compd.*, vol. 285, no. 1-2 Complete, pp. 229–232, 1999.

[46] R. Hermann and W. Löser, "Extension of the primary solidification region of Nd2Fe 14B by levitation of undercooled melts," *J. Appl. Phys.*, vol. 83, no. 11, pp. 6399–6401, Jun. 1998.

[47] J. Gao, T. Volkmann, S. Roth, W. Löser, and D. M. Herlach, "Phase formation in undercooled NdFeB alloy droplets," *J. Magn. Magn. Mater.*, vol. 234, no. 2, pp. 313–319,

2001.

[48] T. Miyazaki and H. Jin, *The Physics of Ferromagnetism*, vol. 158. Berlin, Heidelberg: Springer Berlin Heidelberg, 2012.

[49] R. Skomski, *Simple Models of Magnetism*. Oxford University Press, 2008.

[50] J. M. D. Coey, *Magnetism and Magnetic Materials*. Cambridge University Press, 2001.

[51] J. M. D. Coey and S. S. P. Parkin, *Handbook of Magnetism and Magnetic Materials*. Cham: Springer International Publishing, 2021.

[52] B. D. Cullity and C. D. Graham, *Introduction to magnetic materials*, 2nd Editio. John Wiley & Sons, 2009.

[53] A. Hubert and R. Schäfer, *Magnetic Domains*. Berlin, Heidelberg: Springer Berlin Heidelberg, 1998.

[54] K. A. Gschneidner and L. Eyring, Eds., *Handbook on the Physics and Chemistry of Rare Earths, Volume 1*. Elsevier, 1978.

[55] K. A. Gschneidner and L. Eyring, Eds., *Handbook on the Physics and Chemistry of Rare Earths, Volume 2*. Elsevier, 1979.

[56] K. A. Gschneidner and L. Eyring, Eds., *Handbook on the Physics and Chemistry of Rare Earths, Volume 11*. Elsevier, 1988.

[57] E. . Wolfarth, Ed., *Handbook of Magnetic Materials, Volume 1*. North-Holland Publishing Company, 1980.

[58] E. . Wolfarth, Ed., *Handbook of Magnetic Materials, Volume 3*. North-Holland Publishing Company, 1982.

[59] E. . Wolfarth and K. H. J. Buschow, Eds., *Handbook of Magnetic Materials, Volume 4*. Elsevier, 1988.

[60] K. H. J. Buschow, Ed., *Handbook of Magnetic Materials, Volume 6*. Elsevier, 1991.

[61] R. Skomski and D. J. Sellmyer, “Anisotropy of rare-earth magnets,” *J. Rare Earths*, vol. 27, no. 4, pp. 675–679, Aug. 2009.

[62] N. H. Duc, “Intersublattice exchange coupling in the lanthanide-transition metal intermetallics,” in *Handbook on the Physics and Chemistry of Rare Earths*, vol. 24, 1997, pp. 339–398.

[63] J. J. M. Franse and R. J. Radwanski, “Magnetic Properties of Binary Rare-earth 3d-transition-metal intermetallic Compounds,” in *Handbook of Magnetic Materials, Volume 7*, K. H. J. Buschow, Ed. Elsevier.

[64] L. Rabenberg, R. K. Mishra, and G. Thomas, “Microstructures of precipitation-hardened SmCo permanent magnets,” *J. Appl. Phys.*, vol. 53, no. 3, pp. 2389–2391, 1982.

[65] G. C. Hadjipanayis, “Magnetic hardening in Zr-substituted 2 : 17 rare-earth permanent magnets,” *J. Appl. Phys.*, vol. 55, no. 6, pp. 2091–2093, 1984.

[66] M. Duerrschnabel *et al.*, “Atomic structure and domain wall pinning in samarium-cobalt-based permanent magnets,” *Nat. Commun.*, vol. 8, no. 1, pp. 1–7, 2017.

[67] J. J. Croat, J. F. Herbst, R. W. Lee, and F. E. Pinkerton, “Pr-Fe and Nd-Fe-based materials:

A new class of high-performance permanent magnets (invited)," *J. Appl. Phys.*, vol. 55, no. 6, pp. 2078–2082, 1984.

[68] J. J. Croat, J. F. Herbst, R. W. Lee, and F. E. Pinkerton, "High-energy product Nd-Fe-B permanent magnets," *Appl. Phys. Lett.*, vol. 44, no. 1, pp. 148–149, Jan. 1984.

[69] M. Sagawa, S. Fujimura, N. Togawa, H. Yamamoto, and Y. Matsuura, "New material for permanent magnets on a base of Nd and Fe (invited)," *J. Appl. Phys.*, vol. 55, no. 6, pp. 2083–2087, Mar. 1984.

[70] M. Sagawa, S. Fujimura, H. Yamamoto, Y. Matsuura, and K. Hiraga, "Permanent magnet materials based on the rare earth-iron-boron tetragonal compounds," *IEEE Trans. Magn.*, vol. 20, no. 5, pp. 1584–1589, Sep. 1984.

[71] H. Onodera, Y. Yamaguchi, H. Yamamoto, M. Sagawa, Y. Matsuura, and H. Yamamoto, "Magnetic properties of a new permanent magnet based on a Nd-Fe-B compound (neomax)," *J. Magn. Magn. Mater.*, vol. 46, no. 1–2, pp. 151–156, Dec. 1984.

[72] K. H. J. Buschow, "Permanent magnet materials based on 3d-rich ternary compounds," in *Handbook of Ferromagnetic Materials*, vol. 4, no. C, E. P. Wolfarth and K. H. J. Buschow, Eds. Elsevier, 1988, pp. 1–129.

[73] W. F. Brown, "Virtues and weaknesses of the domain concept," *Rev. Mod. Phys.*, vol. 17, no. 1, pp. 15–19, 1945.

[74] H. Kronmüller, K.-D. Durst, S. Hock, and G. Martinek, "Micromagnetic Analysis of the Magnetic Hardening Mechanisms in RE-Fe-B Magnets," *Le J. Phys. Colloq.*, vol. 49, no. C8, pp. C8-623-C8-628, Dec. 1988.

[75] H. Kronmüller, K.-D. Durst, and M. Sagawa, "Analysis of the magnetic hardening mechanism in RE-FeB permanent magnets," *J. Magn. Magn. Mater.*, vol. 74, no. 3, pp. 291–302, Oct. 1988.

[76] X. C. Kou, H. Kronmüller, D. Givord, and M. F. Rossignol, "Coercivity mechanism of sintered Pr17Fe75B8 and Pr17Fe53B30 permanent magnets," *Phys. Rev. B*, vol. 50, no. 6, pp. 3849–3860, Aug. 1994.

[77] S. Ener *et al.*, "Twins – A weak link in the magnetic hardening of ThMn12-type permanent magnets," *Acta Mater.*, vol. 214, 2021.

[78] X. Ye *et al.*, "Magnetoelectric Tuning of Pinning-Type Permanent Magnets through Atomic-Scale Engineering of Grain Boundaries," *Adv. Mater.*, vol. 33, no. 5, p. 2006853, Feb. 2021.

[79] R. A. Lefever, *Magnetic Materials: Chemistry, Structure, and Crystal Growth*. Cambridge University Press, 2013.

[80] H. Sepehri-Amin, S. Hirosawa, and K. Hono, *Advances in Nd-Fe-B Based Permanent Magnets*, 1st ed., vol. 27. Elsevier B.V., 2018.

[81] S. Hirosawa, Y. Matsuura, H. Yamamoto, S. Fujimura, M. Sagawa, and H. Yamauchi, "Magnetization and magnetic anisotropy of R2Fe14B measured on single crystals," *J. Appl. Phys.*, vol. 59, no. 3, pp. 873–879, 1986.

[82] K.-H. Müller, S. Sawatzki, G. Roland, and O. Gutfleisch, "Permanent Magnet Materials and Applications," in *Handbook of Magnetism and Magnetic Materials*, J. M. D. Coey and S. S. P. Parkin, Eds. Cham: Springer International Publishing, 2021.

[83] R. P. Chaudhary *et al.*, “Development of Mischmetal-Fe-Co-B Permanent Magnet Alloys via High-Throughput Methods,” *ACS Comb. Sci.*, vol. 22, no. 5, pp. 248–254, 2020.

[84] A. Li *et al.*, “Development of Ce-based sintered magnets: review and prospect,” *J. Iron Steel Res. Int.*, vol. 0123456789, 2019.

[85] X. F. Liao *et al.*, “Maximizing the hard magnetic properties of melt-spun Ce–La–Fe–B alloys,” *J. Mater. Sci.*, vol. 54, no. 9, pp. 7288–7299, 2019.

[86] Z. B. Li, M. Zhang, B. G. Shen, F. X. Hu, and J. R. Sun, “Variations of phase constitution and magnetic properties with Ce content in Ce-Fe-B permanent magnets,” *Mater. Lett.*, vol. 172, pp. 102–104, 2016.

[87] X. Tang, H. Sepehri-Amin, M. Matsumoto, T. Ohkubo, and K. Hono, “Role of Co on the magnetic properties of Ce-substituted Nd-Fe-B hot-deformed magnets,” *Acta Mater.*, vol. 175, pp. 1–10, 2019.

[88] C. D. Fuerst, T. W. Capehart, F. E. Pinkerton, and J. F. Herbst, “Preparation and characterization of La2-xCexFe14B compounds,” *J. Magn. Magn. Mater.*, vol. 139, no. 3, pp. 359–363, 1995.

[89] E. Burzo, “Permanent magnets based on R-Fe-B and R-Fe-C alloys,” *Reports Prog. Phys.*, vol. 61, no. 9, pp. 1099–1266, Sep. 1998.

[90] A. C. Neiva, A. P. Tschiptschin, and F. P. Missell, “Phase diagram of the PrFeB system,” *J. Alloys Compd.*, vol. 217, no. 2, pp. 273–282, Feb. 1995.

[91] J. Fidler and T. Schrefl, “Overview of Nd–Fe–B magnets and coercivity (invited),” *J. Appl. Phys.*, vol. 79, no. 8, p. 5029, 1996.

[92] T. Shimoda *et al.*, “Hot-Working Behavior of Cast Pr-Fe-B Magnets,” *IEEE Trans. Magn.*, vol. 25, no. 5, pp. 4099–4104, 1989.

[93] X. D. Xu *et al.*, “Comparison of coercivity and squareness in hot-deformed and sintered magnets produced from a Nd-Fe-B-Cu-Ga alloy,” *Scr. Mater.*, vol. 160, pp. 9–14, 2019.

[94] S. Pandian, V. Chandrasekaran, G. Markandeyulu, K. J. L. Iyer, and K. V. S. Rama Rao, “Effect of Al, Cu, Ga, Nb additions on the magnetic properties and microstructural features of sintered NdFeB,” *J. Appl. Phys.*, vol. 92, no. 10, pp. 6082–6086, 2002.

[95] S. Hirosawa, S. Mino, and H. Tomizawa, “Improved corrosion resistance and magnetic properties of Nd-Fe-B-type sintered magnets with Mo and Co,” *J. Appl. Phys.*, vol. 69, no. 8, pp. 5844–5846, Apr. 1991.

[96] J. Wecker and L. Schultz, “Beneficial effect of Co substitution on the magnetic properties of rapidly quenched Nd-Fe-B,” *Appl. Phys. Lett.*, vol. 51, no. 9, pp. 697–699, Aug. 1987.

[97] J. F. Herbst, “R2Fe14B materials: Intrinsic properties and technological aspects,” *Rev. Mod. Phys.*, vol. 63, no. 4, pp. 819–898, 1991.

[98] C. Koestler, R. Ramesh, C. J. Echer, G. Thomas, and J. Wecker, “Microstructure of melt spun Nd-Fe-Co-B magnets,” *Acta Metall.*, vol. 37, no. 7, pp. 1945–1955, Jul. 1989.

[99] C. N. Christodoulou, T. B. Massalski, and W. E. Wallace, “Magnetic hardening of the Pr2Co14B-based rapidly quenched alloys,” *J. Magn. Magn. Mater.*, vol. 125, no. 1–2, pp. 177–189, 1993.

[100] T. Horikawa, M. Yamazaki, M. Matsuura, and S. Sugimoto, “Recent progress in the

development of high-performance bonded magnets using rare earth–Fe compounds," *Sci. Technol. Adv. Mater.*, vol. 22, no. 1, pp. 729–747, 2021.

[101] K. Hono and H. Sepehri-Amin, "Strategy for high-coercivity Nd-Fe-B magnets," *Scr. Mater.*, vol. 67, no. 6, pp. 530–535, 2012.

[102] P. Nothnagel, K. H. Müller, D. Eckert, and A. Handstein, "The influence of particle size on the coercivity of sintered NdFeB magnets," *J. Magn. Magn. Mater.*, vol. 101, no. 1–3, pp. 379–381, 1991.

[103] O. Gutfleisch and I. R. Harris, "Fundamental and practical aspects of the hydrogenation, disproportionate, desorption and recombination process," *J. Phys. D. Appl. Phys.*, vol. 29, no. 9, pp. 2255–2265, 1996.

[104] R. J. Chen *et al.*, "Rare earth permanent magnets prepared by hot deformation process," *Chinese Phys. B*, vol. 27, no. 11, pp. 1–42, 2018.

[105] R. C. Budhani, T. C. Goel, and K. L. Chopra, "Melt-spinning technique for preparation of metallic glasses," *Bull. Mater. Sci.*, vol. 4, no. 5, pp. 549–561, 1982.

[106] J. H. H. Liebermann and C. D. Graham, "Production of Amorphous Ribbons and Effects of Apparatus Parameters on Ribbon Dimensions," *Mater. Res.*, 1976.

[107] W. Grünberger, D. Hinz, A. Kirchner, K. H. Müller, and L. Schultz, "Hot deformation of nanocrystalline Nd-Fe-B alloys," *IEEE Trans. Magn.*, vol. 33, no. 5 PART 2, pp. 3889–3891, 1997.

[108] K. Khlopkov, O. Gutfleisch, D. Hinz, K. H. Müller, and L. Schultz, "Evolution of interaction domains in textured fine-grained Nd2 Fe14 B magnets," *J. Appl. Phys.*, vol. 102, no. 2, 2007.

[109] K. Khlopkov *et al.*, "Local texture in Nd-Fe-B sintered magnets with maximised energy density," *J. Alloys Compd.*, vol. 365, no. 1–2, pp. 259–265, 2004.

[110] P. Gaunt, "Ferromagnetic domain wall pinning by a random array of inhomogeneities," *Philos. Mag. B Phys. Condens. Matter; Stat. Mech. Electron. Opt. Magn. Prop.*, vol. 48, no. 3, pp. 261–276, 1983.

[111] O. Gutfleisch *et al.*, "Nanocrystalline high performance permanent magnets," *J. Magn. Magn. Mater.*, vol. 242–245, no. PART II, pp. 1277–1283, 2002.

[112] X. Tang, H. Sepehri-Amin, T. Ohkubo, K. Hioki, A. Hattori, and K. Hono, "Coercivities of hot-deformed magnets processed from amorphous and nanocrystalline precursors," *Acta Mater.*, vol. 123, pp. 1–10, 2017.

[113] X. Xia *et al.*, "Improvement of thermal stability in hot-deformed Nd-Fe-B magnets by grain refinement," *Scr. Mater.*, vol. 178, pp. 129–133, Mar. 2020.

[114] L. Liu *et al.*, "Coercivity enhancement of Nd-Fe-B hot-deformed magnets by the eutectic grain boundary diffusion process using Nd-Ga-Cu and Nd-Fe-Ga-Cu alloys," *AIP Adv.*, vol. 8, no. 5, p. 056205, May 2018.

[115] X. Tang *et al.*, "Relationship between the thermal stability of coercivity and the aspect ratio of grains in Nd-Fe-B magnets: Experimental and numerical approaches," *Acta Mater.*, vol. 183, pp. 408–417, Jan. 2020.

[116] S. Hirosawa, M. Nishino, and S. Miyashita, "Perspectives for high-performance permanent magnets: Applications, coercivity, and new materials," in *Advances in Natural*

Sciences: Nanoscience and Nanotechnology, 2017, vol. 8, no. 1.

[117] T. G. Woodcock *et al.*, "Understanding the microstructure and coercivity of high performance NdFeB-based magnets," *Scripta Materialia*, vol. 67, no. 6. pp. 536–541, 2012.

[118] M. Sagawa, H. Nagata, T. Watanabe, and O. Itatani, "Rubber isostatic pressing (RIP) of powders for magnets and other materials," *Mater. Des.*, vol. 21, no. 4, pp. 243–249, 2000.

[119] H. Sepehri-Amin, Y. Une, T. Ohkubo, K. Hono, and M. Sagawa, "Microstructure of fine-grained Nd-Fe-B sintered magnets with high coercivity," *Scr. Mater.*, vol. 65, no. 5, pp. 396–399, 2011.

[120] A. G. Popov *et al.*, "Preparation of sintered Nd-Fe-B magnets by pressless process," *Phys. Met. Metallogr.*, vol. 113, no. 4, pp. 331–340, 2012.

[121] A. G. Popov, O. A. Golovnia, and V. A. Bykov, "Pressless process in route of obtaining sintered Nd-Fe-B magnets," *J. Magn. Magn. Mater.*, vol. 383, pp. 226–231, 2015.

[122] T. G. Woodcock, F. Bittner, T. Mix, K. H. Müller, S. Sawatzki, and O. Gutfleisch, "On the reversible and fully repeatable increase in coercive field of sintered Nd-Fe-B magnets following post sinter annealing," *J. Magn. Magn. Mater.*, vol. 360, pp. 157–164, 2014.

[123] R. Ramesh and K. Srikrishna, "Magnetization reversal in nucleation controlled magnets. I. Theory," *J. Appl. Phys.*, vol. 64, no. 11, pp. 6406–6415, 1988.

[124] R. Ramesh, G. Thomas, and B. M. Ma, "Magnetization reversal in nucleation controlled magnets. II. Effect of grain size and size distribution on intrinsic coercivity of Fe-Nd-B magnets," *J. Appl. Phys.*, vol. 64, no. 11, pp. 6416–6423, Dec. 1988.

[125] C. Wendt, S. R. Fernández-Vidal, Á. Gómez-Parra, M. Batista, and M. Marcos, "Processing and Quality Evaluation of Additive Manufacturing Monolayer Specimens," *Adv. Mater. Sci. Eng.*, vol. 2016, 2016.

[126] N. Guo and M. C. Leu, "Additive manufacturing: Technology, applications and research needs," *Frontiers of Mechanical Engineering*, vol. 8, no. 3. pp. 215–243, 2013.

[127] C. Panwisawas, Y. T. Tang, and R. C. Reed, "Metal 3D printing as a disruptive technology for superalloys," *Nat. Commun.*, vol. 11, no. 1, pp. 1–4, 2020.

[128] J. Jaćimović *et al.*, "Net Shape 3D Printed NdFeB Permanent Magnet," *Adv. Eng. Mater.*, vol. 19, no. 8, p. 1700098, Aug. 2017.

[129] "Mqp-S-11-9-20001-070 Datasheet." [Online]. Available: https://mqitechnology.com/product/mqp-s-11-9-20001/.

[130] C. Huber *et al.*, "Coercivity enhancement of selective laser sintered NdFeB magnets by grain boundary infiltration," *Acta Mater.*, vol. 172, pp. 66–71, 2019.

[131] A. S. Volegov *et al.*, "Additive manufacturing of heavy rare earth free high-coercivity permanent magnets," *Acta Mater.*, vol. 188, pp. 733–739, Apr. 2020.

[132] F. Bittner, J. Thielsch, and W. G. Drossel, "Laser powder bed fusion of Nd–Fe–B permanent magnets," *Prog. Addit. Manuf.*, vol. 5, no. 1, pp. 3–9, 2020.

[133] N. Urban, F. Huber, and J. Franke, "Influences of process parameters on rare earth magnets produced by laser beam melting," in *2017 7th International Electric Drives Production Conference (EDPC)*, 2017, pp. 1–5.

[134] N. Urban, A. Meyer, V. Keller, and J. Franke, “Contribution of Additive Manufacturing of Rare Earth Material to the Increase in Performance and Resource Efficiency of Permanent Magnets,” *Appl. Mech. Mater.*, vol. 882, pp. 135–141, Jul. 2018.

[135] L. Schäfer *et al.*, “Design and Qualification of Pr–Fe–Cu–B Alloys for the Additive Manufacturing of Permanent Magnets,” *Adv. Funct. Mater.*, vol. 31, no. 33, p. 2102148, Aug. 2021.

[136] N. Urban, A. Kuhl, M. Glauche, and J. Franke, “Additive Manufacturing of Neodymium-Iran-Boron Permanent Magnets,” *2018 8th Int. Electr. Drives Prod. Conf. EDPC 2018 - Proc.*, pp. 6–10, 2019.

[137] D. Goll, F. Trauter, T. Bernthaler, J. Schanz, H. Riegel, and G. Schneider, “Additive Manufacturing of Bulk Nanocrystalline FeNdB Based Permanent Magnets,” *Micromachines*, vol. 12, no. 5, p. 538, May 2021.

[138] F. Bittner, J. Thielsch, and W.-G. Drossel, “Laser powder bed fusion of Nd–Fe–B permanent magnets,” *Prog. Addit. Manuf.*, vol. 5, no. 1, pp. 3–9, Mar. 2020.

[139] T. Kolb *et al.*, “Laser Beam Melting of NdFeB for the production of rare-earth magnets,” in *2016 6th International Electric Drives Production Conference, EDPC 2016 - Proceedings*, 2016, pp. 34–40.

[140] N. Sridharan *et al.*, “Rationalization of solidification mechanism of Nd–Fe–B magnets during laser directed-energy deposition,” *J. Mater. Sci.*, vol. 53, no. 11, pp. 8619–8626, 2018.

[141] M. Skalon *et al.*, “Influence of Melt-Pool Stability in 3D Printing of NdFeB Magnets on Density and Magnetic Properties,” *Materials (Basel).*, vol. 13, no. 1, p. 139, Dec. 2019.

[142] D. Goll, F. Trauter, R. Loeffler, T. Gross, and G. Schneider, “Additive Manufacturing of Textured FePrCuB Permanent Magnets,” *Micromachines*, vol. 12, no. 9, p. 1056, Aug. 2021.

[143] T. Kozieł, “Estimation Of Cooling Rates In Suction Casting And Copper-Mould Casting Processes,” *Arch. Metall. Mater.*, vol. 60, no. 2, pp. 767–771, Jun. 2015.

[144] R. M. Srivastava, J. Eckert, W. Löser, B. K. Dhindaw, and L. Schultz, “Cooling Rate Evaluation for Bulk Amorphous Alloys from Eutectic Microstructures in Casting Processes,” *Mater. Trans.*, vol. 43, no. 7, pp. 1670–1675, 2002.

[145] P. Pawlik, K. Pawlik, and A. Przybył, “Investigation of the cooling rate in the suction casting process,” *Rev. Adv. Mater. Sci.*, vol. 18, no. 1, pp. 81–84, 2008.

[146] L. Schäfer *et al.*, “A Novel Magnetic Hardening Mechanism for Nd-Fe-B Permanent Magnets Based on Solid-State Phase Transformation,” *Adv. Funct. Mater.*, p. 2208821, Nov. 2022.

[147] J. Wecker and L. Schultz, “Coercivity of metastable (Nd,Pr)-Fe-Co-B alloys,” *J. Magn. Magn. Mater.*, vol. 80, no. 1, pp. 97–100, Aug. 1989.

[148] C. D. Fuerst and J. F. Herbst, “Hard magnetic properties of melt-spun Nd-Co-Fe-B materials,” *J. Appl. Phys.*, vol. 63, no. 8, pp. 3324–3326, Apr. 1988.

[149] I. Arganda-Carreras *et al.*, “Trainable Weka Segmentation: a machine learning tool for microscopy pixel classification,” *Bioinformatics*, vol. 33, no. 15, pp. 2424–2426, Aug. 2017.

[150] C. Chacon and O. Isnard, “Neutron-diffraction study of the Ndn+1Co3n+5B2n compounds,” *Appl. Phys. A Mater. Sci. Process.*, vol. 74, no. SUPPL.I, pp. 2–5, 2002.

[151] Y. Wu *et al.*, “A comparative study of Nd15Fe78B7 and Nd15Co78B7 systems: phase formations and coercivity mechanisms,” *Acta Mater.*, vol. 240, no. September, p. 118311, 2022.

[152] Y. Wu *et al.*, “Microstructure, coercivity and thermal stability of nanostructured (Nd,Ce)-(Fe,Co)-B hot-compacted permanent magnets,” *Acta Mater.*, vol. 235, no. January, p. 118062, Aug. 2022.

[153] X. Shen, Y. Wang, Z. Diao, and X. Liu, “The effect of molybdenum on the magnetic properties of the Nd-Fe-Co-B system,” *J. Appl. Phys.*, vol. 61, no. 8, pp. 3433–3435, 1987.

[154] G. Rieger, M. Seeger, L. Sun, and H. Kronmüller, “Micromagnetic analysis applied to melt-spun NdFeB magnets with small additions of Ga and Mo,” *J. Magn. Magn. Mater.*, vol. 151, no. 1–2, pp. 193–201, Nov. 1995.

[155] W. Meiners, “Direktes Selektives Laser Sintern Einkomponentiger Metallischer Werkstoffe,” Rheinisch-Westfälische Technische Hochschule Aachen, 1999.

[156] A. B. Spierings and G. Levy, “Comparison of density of stainless steel 316L parts produced with Selective Laser Melting using different powder grades,” *20th Annu. Int. Solid Free. Fabr. Symp.*, 2009.

List of Figures

List of Tables

List of Publications

[1] O. Tosoni, E. Borges, J. Reijonen, A. Antikainen, **L. Schäfer**, S. Riegg, O. Gutfleisch, "High-Coercivity Copper-Rich Nd-Fe-B Magnets by Powder Bed Fusion Using Laser Beam Method," *Add. Manu*, p. 103426, 2023.

[2] F. Staab, E. Bruder, **L. Schäfer**, K. Skokov, D. Koch, B. Zingsem, E. Adabifiroozjaei, L. Molina-Luna, O. Gutfleisch, K. Durst "Hard Magnetic $SmCo_5$-Cu Nanocomposites Produced by Severe Plastic Deformation," *Acta Mater.*, p. 118709, 2023.

[3] **L. Schäfer**, K. Skokov, F. Maccari, I. Radulov, D. Koch, A. Mazilkin, E. Adabifiroozjaei, L. Molina-Luna, O. Gutfleisch, "A Novel Magnetic Hardening Mechanism for Nd-Fe-B Permanent Magnets Based on Solid-State Phase Transformation," *Adv. Funct. Mater*, p. 2208821, Nov. 2022.

[4] O. Tosoni, E. Borges, J. Reijonen, A. Antikainen, **L. Schäfer**, and S. Riegg, "High-coercivity NdFeB Printed Magnets With Laser Powder Bed Fusion Method," in *World PM2022 Congress Proceedings*, 2022.

[5] J. Altenberend, R. Dolbec, J. Reijonen, S. Riegg, **L. Schäfer**, O. Tosoni, R. Vert, P. V. Wijk, "Plasma Spheroidization Of Nd-Fe-B Powder For Additive Manufacturing," in *World PM2022 Congress Proceedings*, 2022.

[6] Y. Wu, K. Skokov, **L. Schäfer**, F. Maccari, A. Aubert, H. Xu, H. Wu, C. Jiang, O. Gutfleisch, "Microstructure, coercivity and thermal stability of nanostructured (Nd,Ce)-(Fe,Co)-B hot-compacted permanent magnets," *Acta Mater.*, vol. 235, no. January, p. 118062, Aug. 2022.

[7] Y. Wu, K. Skokov, **L. Schäfer**, F. Maccari, A. Aubert, Z. Rau, K. Schweinar, B. Gault, H. Xu, C. Jiang, "A comparative study of $Nd_{15}Fe_{78}B_7$ and $Nd_{15}Co_{78}B_7$ systems: phase formations and coercivity mechanisms," *Acta Mater.*, vol. 240, no. September, p. 118311, 2022.

[8] F. Maccari, S. Ener, D. Koch, I. Dirba, K. Skokov, E. Bruder, **L. Schäfer**, O. Gutfleisch, "Correlating changes of the unit cell parameters and microstructure with magnetic properties in the $CeFe_{11}Ti$ compound," *J. Alloys Compd.*, vol. 867, p. 158805, Jun. 2021.

[9] X. Ye, Y. Fengkai, **L. Schäfer**, D. Wang, H. Geßwein, W. Wang, M. R. Chellali, L. T. Stephenson, K. Skokov, O. Gutfleisch, D. Raabe, H. Hahn, B. Gault, R. Kruk, "Magnetoelectric Tuning of Pinning-Type Permanent Magnets through Atomic-Scale Engineering of Grain Boundaries," *Adv. Mater.*, vol. 33, no. 5, pp. 2–8, 2021.

[10] **L. Schäfer**, K. Skokov, J. Liu, F. Maccari, T. Braun, S. Riegg, I. Radulov, J. Gassmann, H. Merschroth, J. Harbig, M. Weigold, O. Gutfleisch, "Design and Qualification of Pr–Fe–Cu–B Alloys for the Additive Manufacturing of Permanent Magnets," *Adv. Funct. Mater.*, vol. 31, no. 33, p. 2102148, Aug. 2021.

[11] S. Ener, D. Palanisamy, T. Devillers, J. Fischbacher, G. G. Eslava, F. Maccari, **L. Schäfer**, L. V. B. Diop, I. Radulov, B. Gault, G. Hrkac, N. M. Dempsey, T. Schrefl, D. Raabe, O. Gutfleisch, "Twins – A weak link in the magnetic hardening of $ThMn_{12}$-type permanent magnets," *Acta Mater.*, vol. 214, 2021.

[12] D. Palanisamy, S. Ener, F. Maccari, **L. Schäfer**, K. Skokov, O. Gutfleisch, D. Raabe, B. Gault, "Grain boundary segregation, phase formation, and their influence on the coercivity of rapidly solidified $SmFe_{11}Ti$ hard magnetic alloys," *Phys. Rev. Mater.*, vol. 4, no. 5, p. 54404, 2020.

[13] Z. Rao, B. Dutta, F. Körmann, D. Ponge, L. Li, J. He, L. Stephenson, **L. Schäfer**, K. Skokov, O. Gutfleisch, D. Raabe, "Unveiling the mechanism of abnormal magnetic behavior of FeNiCoMnCu high-entropy alloys through a joint experimental-theoretical study," *Phys. Rev. Mater.*, vol. 4, no. 1, p. 014402, Jan. 2020.

[14] F. Maccari, **L. Schäfer**, I. Radulov, L. V. B. Diop, S. Ener, E. Bruder, K. Skokov, O. Gutfleisch, "Rapid solidification of $Nd_{1+x}Fe_{11}Ti$ compounds: Phase formation and magnetic properties," *Acta Mater.*, vol. 180, pp. 15–23, Nov. 2019.

Acknowledgements

I would like thank **Prof. Oliver Gutfleisch** for supervising this PhD work and for giving me the opportunity to join the Functional Materials group. I really appreciate this period and the experience that I have gained throughout these years of research in the group. The possibility to meet and work with several experts in the field of magnetism and metallurgy greatly influenced my development. I also want to acknowledge **Prof. Karsten Durst** who kindly agreed to co-referee my thesis.

A dissertation should prove that the candidate understands how to work independently, methodically and scientifically, yet the knowledge gained is not an individual achievement. Numerous outstanding scientists, themselves still new to the field and highly motivated or already working for a long time and therefore indispensable through their experience, have supported me and therefore contributed significantly to the results of this work. I am very thankful for all the collaborations with scientists all over the world. Furthermore, the direct environment in the Materials Science department and especially the Functional Materials group has provided all resources and possibilities to enable this work. I would like to thank all the "MaWis" I had the pleasure of working with and the great people in "FM-all".

I would especially like to thank my supervisor who has supported me since my Advanced Research Lab, Master's thesis and finally during my PhD. Everyone who knows him knows what incredible experience and knowledge he has and I thank him for sharing it with me and allowing me to learn a lot, theoretically and practically. Большое спасибо **Dr. Konstantin Skokov.**

Sooner or later, every student will test the limits of measuring instruments and devices and you are not always lucky. In these cases, I was very grateful that someone was always there to help. I am sorry for the trouble and thank you very much Repairmasters **Mark Pabst**, **Marcel Eitner** and **Bernd Stoll**.

I would like to thank the secret powers in the Functional Materials group. I know I can be exhausting, but I think you guys always had something to laugh about. Many thanks to Chief Secretary **Maija Laux** and Head of Dispatch **Kirit Kaiser**.

Lastly, I would like to thank the Deutsche Forschungsgemeinschaft (DFG) for the financial support through the CRC/ TRR 270 "HoMMage" and all collaborators, partners and especially my fellow PhD students. I wish everyone much success!